X-ray Microcalorimetry for Space

Ian John Davenport

PhD Thesis

University College London

1994

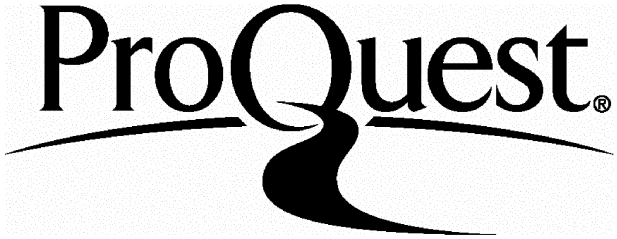

Abstract

The X-ray microcalorimeter is an X-ray detector of potentially high energy resolution and quantum efficiency. The energy of incident X-rays is determined by measuring the resultant change in the resistance of a cooled semiconductor as an X-ray is incident on it.

The history of X-ray microcalorimetry is reviewed, the current state of the art is placed in the context of contemporary X-ray detectors, and new X-ray detectors in the development stages. The performance of X-ray microcalorimeters is compared to other detectors.

The principles of operation of microcalorimeters are discussed, and the relations between operating parameters established. The system devised and operated by the *University of London* microcalorimetry collaboration is described, and the future development of X-ray microcalorimetry considered.

The design and implementation of a suite of computer programmes to analyse the data generated by the detector is described, and a space-based processing system defined.

Results obtained with the detector operating at 100 mK in 1991 facing a $^{55}_{25}$Fe source are presented and analysed. A resolution of 316 eV is shown at 200 mK, and 276 eV at 100 mK. The absence of the expected improvement in resolution at the lower temperature is investigated.

The microcalorimeter as an observational tool will require a space platform at a low temperature. Various low-temperature techniques are described, and the design and operation of the adiabatic demagnetisation refrigerator (ADR) used is described and modelled.

The ADR is appraised as a means of cooling a space-based detector to 100 mK, and a hypothetical system involving a 2-stage ADR is devised and modelled. One ADR operates between 100 mK and 1.0 K, and a second operates between 1.0 K and 4.0 K. The complete cooling system maintains a 100 mK stage for 59 hours, with a recycle time of 17 hours. Replacing the high temperature ADR with a pumped helium tank cooling to 2.0 K increases the hold time to 80 hours, recycling in 3 minutes.

Contents

1 The History of X-Ray Calorimetry **21**

1.1 Early History 21

1.2 Microcalorimetry In Context 22

1.2.1 Position Sensitive and Gas Scintillation Proportional Counters 22

1.2.2 Microchannel Plates 24

1.2.3 Charge Coupled Devices 24

1.2.4 X-ray Microcalorimeters 25

1.2.5 Comparisons 25

1.3 Review of Micro-calorimetry Work 26

1.3.1 *GSFC / NASA* Collaboration 26

1.3.2 *Lawrence Livermore National Laboratory (LLNL)* 28

1.3.3 *University of London* Collaboration 28

1.4 Other Next-generation X-ray Detectors 29

1.4.1 Superconducting Tunnelling Junctions 29

1.4.2 Dielectric Microcalorimeters 30

1.4.3 Kinetic Inductance Microcalorimeters 31

2 Principles of X-ray Microcalorimetry **37**

2.1 The Basic Process 37

2.1.1 Semiconductivity, The Band Theory of Solids 37

2.1.2 The Thermalisation of X-rays 40

2.1.3 The Hot Electron Effect 46

2.1.4 Observation 46

2.2 Example System 48

2.2.1 Description 48

2.2.2 Bolometer Characteristics 48

2.2.3 Amplification Electronics 49

2.2.4 Computer Simulation 49

2.3 The Effects of different materials 50

2.3.1 Germanium 50

2.3.2 Silicon 51

2.3.3 A thermalising medium 51

2.4 Sources of Noise 53

2.4.1 Johnson Noise from the Microcalorimeter 54

2.4.2 Phonon Noise due to heat flow from the Microcalorimeter to the heat sink 54

2.4.3 Johnson Noise from the Bias Resistor 56

2.4.4 Pre-amplifier Noise 56

2.4.5 Excess noise 57

2.4.6 Spurious pulses 57

2.4.7 Statistical Variation in the number of Phonons Created . . 58

2.5 Other resolving power limitations 60

2.5.1 Electron Traps 60
2.5.2 Photo-electron emission 61
2.5.3 Radiative Losses 61
2.5.4 Metastable states 62
2.5.5 Non-thermal phonon spectrum 62
2.5.6 Thermal Uniformity 62
2.6 Future Developments 63
2.6.1 Environment 63
2.6.2 Arrays 63

3 Data Processing Techniques **71**

3.1 Initial Processing 71
3.1.1 Raw data form 71
3.1.2 Pulse Viewing 72
3.1.3 Pulse height determination 73
3.2 χ^2 Rejection of Non-conforming pulses 73
3.3 Matched Filtering of Pulses 76
3.4 Maximum Entropy Method of Deconvolution 79
3.5 The Fitting of Data 79
3.5.1 Determining the Point Spread Function, and Internal Noise 79
3.5.2 Fitting the Data to the Gaussians 81
3.5.2.1 Fitting Individual Peaks 82
3.5.2.2 Fitting Both Peaks Simultaneously 82
3.6 Testing the Processing Software 85
3.6.1 Outline of Procedure 85

3.6.2 Implementation 86
3.6.3 Results 86
3.7 A Space-based Processing System 86
3.7.1 Outline 86
3.7.2 A System based on the Current Algorithms 88
3.7.2.1 Initial Storage 88
3.7.2.2 χ^2 Rejection of Pulses 88
3.7.2.3 Matched Filter 89
3.7.2.4 Conclusion 90
3.7.3 A Space-based Processing System 90
3.7.3.1 Description 90
3.7.3.2 Total Memory Requirement 91
3.7.3.3 A Further Refinement 91
3.7.3.4 Speed of Processing 92

4 November 1991 Data and Interpretation 97

4.1 Source of Data 97
4.1.1 System Description 97
4.1.2 Schedule of Run 98
4.1.3 Table of Information on Source Data 98
4.2 Forms of Processing applied to data 100
4.2.1 χ^2 rejection 100
4.2.2 Binning technique in Matched Filtering 100
4.2.3 Fitting parameters applied 101
4.3 χ^2 Rejection and Matched Filter on all files 101

4.3.1 Processing of Individual Data files 102
4.3.2 100 mK Summed Data - Comments 133
4.3.3 200 mK Summed Data - Comments 135
4.4 Noise File Processing 136
4.5 Results of Processing 141
4.5.1 The Results of Rejection 141
4.5.2 Resolution Obtained 141
4.5.3 Quality of Gaussian fit to histogram 141
4.5.4 Fluorescence Yield Ratio 144
4.5.5 Point Spread Function, Internal Noise 144
4.6 Conclusions 148
4.6.1 Rejection Statistics 148
4.6.2 Full Width at Half Maximum 148
4.6.3 Quality of Fit 149
4.6.4 Fluorescence Yield Ratio (FYR) 149
4.6.5 Point Spread Function, Internal Noise 150
4.6.6 The 4 KeV to 6 KeV Noise 151

5 General Refrigeration Techniques 155

5.1 The Need for Refrigeration 155
5.2 The Use of Liquid Cryogens 156
5.2.1 Cooling by Nitrogen Evaporation 156
5.2.2 Cooling by ^{4}Helium Evaporation 156
5.2.3 Cooling by ^{3}Helium Evaporation 157
5.3 Magnetic Refrigeration 157

5.3.1 Adiabatic Demagnetisation of a Paramagnetic Salt 157
5.3.1.1 Principle of Operation 158
5.3.1.2 System Description 159
5.3.2 Nuclear Demagnetisation 161
5.4 Helium Dilution Refrigeration 161
5.5 Mechanical Cooling 161
5.6 The *Cochise* ADR experimental set up 162
5.6.1 General Description of System 162
5.6.1.1 The Salt Pill 162
5.6.1.2 The Superconducting Electromagnet 164
5.6.1.3 The Helium Chamber (Can) 164
5.6.2 Description of Operation 165
5.6.3 Thermal model of System 166
5.6.3.1 Node 1 - The Detector 166
5.6.3.2 Node 2 - The Detector Mount 169
5.6.3.3 Node 3 - The Detector Stage 169
5.6.3.4 Node 4 - The Salt Pill 169
5.6.3.5 Node 5 - The Helium Jacket 170
5.6.3.6 Node 6 - The Inner Helium Shield 170
5.6.3.7 Node 7 - The Helium Plate 170
5.6.3.8 Node 8 - The World 171
5.6.3.9 Node 9 - The Source 171
5.6.3.10 Node 10 - Outer Helium Shield 171
5.6.3.11 Modelling 171
5.6.4 A Higher Temperature Salt Pill 172

5.6.4.1 Initial GGG Preparation 172
5.6.4.2 Pill Preparation 172
5.6.4.3 Pill Testing 173

6 Space Application 177

6.1 The Need for a Spaceborne Platform 177
6.2 Means of Attaining a Space Platform 177
6.2.1 Balloon 177
6.2.2 Sounding Rocket 178
6.2.3 Space Station 178
6.2.4 Recoverable Module 178
6.2.5 Space Shuttle Short-term Module 179
6.2.6 Free-flying Satellite 180
6.3 Choice of Orbit 180
6.3.1 Geostationary Orbit 181
6.3.2 Low Earth Orbit (LEO) 181
6.3.3 Highly Eccentric Orbit (HEO) 181
6.4 Considerations for a Space-based refrigerator 182
6.4.1 Size 182
6.4.2 Mass 182
6.4.3 Ambient Magnetic Field Strength 183
6.4.4 Control Instrumentation 184
6.4.5 Reliability 184
6.4.6 Hardiness 184
6.4.7 Long-duration Stability 185

6.4.8 Zero-gravity Environment 185
6.5 The Use of Helium Dilution Refrigeration in Space 186
6.6 The Use of an ADR in Space 187
6.6.1 Support Structures 187
6.6.1.1 General Considerations 187
6.6.1.2 Kevlar Thread Diameter Determination 188
6.6.2 Heat Switch Qualification 190
6.6.2.1 Gas Heat Switch 191
6.6.2.2 Mechanical Heat Switch 191
6.6.3 Choice of Magnet 192
6.6.3.1 A Superconducting Electromagnet 192
6.6.3.2 A Permanent Magnet 193

7 A Space-Based ADR 197

7.1 Objective 197
7.2 Brief Overview of Operation 199
7.3 First Stage ADR Description and Thermal Model 200
7.3.1 Hold Time 200
7.3.2 Recycle Time 203
7.4 Description of Second Stage ADR 204
7.5 Overall Arrangement Thermal Model 205
7.5.1 Node 1 - Spacecraft 205
7.5.2 Node 2 - The Link Stage 205
7.5.3 Node 3 - Stage 1 Magnet 205
7.5.4 Node 4 - The Stage 1 Magnet Supports 207

7.5.5 Node 5 - Stage 1 Salt Pill 207
7.5.6 Node 6 - The Detector Stage 208
7.5.7 Node 7 - The Bolometer 208
7.5.8 Node 8 - Second Stage Salt Pill 208
7.5.9 Node 9 - The Stage 2 Magnet 208
7.5.10 Node 10 - The Stage 2 Magnet Supports 209
7.5.11 Node 11 - The Environment Case 209
7.5.12 Node 12 - The Stage 1 Hex frame 209
7.6 Determination of the Stage 2 Salt Pill Mass 209
7.6.1 Determination of ρ_E 211
7.6.2 Determination of Q_{cool1} 211
7.6.3 Determination of P_1 214
7.6.4 Determination of P_2 216
7.6.5 Recycling Stage 2 217
7.7 An Alternative Stage 2 - Cooled Helium bath 219
7.8 Conclusions re: a viable space refrigeration system 220
7.9 Electronic Control Systems 221
7.9.1 On-board Electronics Functions 222
7.9.2 System Telecommands 222
7.9.3 2-Stage ADR Control Diagram 223
7.9.4 Electronic System Constraints 225
7.9.5 Analogue Electronics Subsystem 225
7.9.6 Digital Electronics Subsystem 226
7.9.7 The Microprocessor Subsystem 227
7.9.7.1 Microprocessor Elements 227

7.9.7.2 Sofware Approaches 228
7.9.8 OBDH Interface Subsystem 229
7.9.9 DC/DC Converter Subsystem 230

List of Figures

2.1 Illustration of the Band Theory of Semiconduction 39

2.2 Thermodynamic arrangement of microcalorimeter 41

2.3 Ideal output pulse from one X-ray event 45

2.4 A typical X-ray pulse 45

2.5 The amplification system 47

2.6 Electrical connections to an array of elements. 65

3.1 The Processed Simulated Data 87

3.2 Processing Flow Chart 93

4.1 FE1.19.11.DAT, no rejection 104

4.2 FE1.19.11.DAT, 90 rejection 104

4.3 FE1.19.11.DAT, no rejection 106

4.4 FE1.19.11.DAT, 90 rejection 106

4.5 FE3.19.11.DAT, no rejection 108

4.6 FE3.19.11.DAT, 90 rejection 108

4.7 FE1.20.11.DAT, no rejection 110

4.8 FE1.20.11.DAT, 90 Rejection 110

4.9 FE2.20.11.DAT, no rejection 112

4.10 FE2.20.11.DAT, 90 Rejection 112
4.11 FE3.20.11.DAT, no rejection 114
4.12 FE3.20.11.DAT, 90 Rejection 114
4.13 FE4.20.11.DAT, no rejection 116
4.14 FE4.20.11.DAT, 90 Rejection 116
4.15 FE5.20.11.DAT, no rejection 118
4.16 FE5.20.11.DAT, 90 Rejection 118
4.17 FE6.20.11.DAT, no rejection 120
4.18 FE6.20.11.DAT, 90 Rejection 120
4.19 FE7.20.11.DAT, no rejection 122
4.20 FE7.20.11.DAT, 90 Rejection 122
4.21 FE8.20.11.DAT, no rejection 124
4.22 FE8.20.11.DAT, 90 Rejection 124
4.23 FE10.20.11.DAT, no rejection 126
4.24 FE10.20.11.DAT, 90 Rejection 126
4.25 FE11.20.11.DAT, no rejection 128
4.26 FE11.20.11.DAT, 90 Rejection 128
4.27 FE12.20.11.DAT, No rejection 130
4.28 FE12.20.11.DAT, 90 Rejection 130
4.29 100 mK summed data, no rejection 132
4.30 100 mK summed data, 90 Rejection 132
4.31 200 mK summed data, no rejection 134
4.32 200 mK summed data, 90 Rejection 134
4.33 File NOISE1.DAT 137
4.34 File NOISE2.DAT 137

4.35 File NOISE3.DAT 138

4.36 File NOISE4.DAT 138

4.37 File NOISE5.DAT 139

4.38 File NOISE7.DAT 139

4.39 File NOISE8.DAT 140

5.1 Standard Operation of an ADR 160

5.2 Isothermal Operation of an ADR 160

5.3 Cutaway schematic of *Cochise* ADR 163

5.4 Thermal model of *Cochise* ADR 167

7.1 Overview of Space-based ADR 198

7.2 Two stage ADR cycle 201

7.3 Stage 1 of the Space ADR 202

7.4 The node structure of the System Thermal Model 206

7.5 Determination of absorbable energy density ρ_E 213

7.6 Variation in Stage 2 hold time with pill mass 217

7.7 Block Diagram 221

7.8 Microprocessor Diagram 227

List of Tables

4.1 Source Data 99

4.2 Pulse rejection statistics 142

4.3 FWHM Results 143

4.4 Energy Histogram Fitting 145

4.5 Fluorescence Yield Ratio 146

4.6 Noise Data 147

5.1 Thermal model of Cochise ADR 168

7.1 GGG cooling energy 212

7.2 Hold Time Available from Stage 2 218

7.3 ADR Control Cycle 224

Chapter 1

The History of X-Ray Calorimetry

1.1 Early History

Without doubt the very earliest calorimeters were the naturally occurring ones, planets and satellites whose temperature rises by tens of kelvin due to internal radioactivity. Interstellar particles of size 40 angstroms can rise in temperature by as much as 200 K.

Calorimetry was first used in the early days of nuclear physics, for the measurement of the integrated energy of radioactivities, following Curie and Laborde's attempts to verify that the heat produced from radioactive species resulted from the absorption of emitted radiation. By the mid 1930s it was possible to operate small calorimeters at temperatures as low as 30 mK. The first composite calorimeter was developed in the early 1970s at the *Laboratoire de Physique Stellaire et Planetaire* (*LPSP*), with a large surface area and a very small monolithic semiconductor.

In 1975, T.O. Niinikoski reported spurious heating, which he identified with the passage of cosmic rays, but it was not until eight years later, in 1983, that work began on single particle calorimetry. Several institutions including the *Goddard*

Space Flight Center (*GSFC*) and the *European Space Agency* (*ESA*) started work around then, and by 1984, it was clear that thermal detectors cooled to very low temperatures were going to be potential single event particle detectors of good resolution.

1.2 Microcalorimetry In Context

Chapter 2 gives a detailed description of microcalorimetry in principle and practice, however, it is worth, at this point, briefly surveying the range of currently proven X-ray detectors, in order to show why X-ray microcalorimeters should be developed, and to place them in their context.

1.2.1 Position Sensitive and Gas Scintillation Proportional Counters

The earliest X-ray detectors are position sensitive and gas scintillation proportional detectors. The principle of operation of these devices is that X-rays enter a gas-filled cavity through a thin window, and may be incident on a gas molecule. Usually this gas is xenon. Photoelectric absorption of the X-ray takes place which excites the atom and releases a photo-electron. The atom de-excites by emitting an X-ray or an Auger electron (see section 2.1.2), while the electron has sufficient energy to ionise other gas molecules, and proceeds to do so until one electron-ion pair is produced for each 30 eV of the original X-ray energy. In Position Sensitive Proportional Counters (PSPCs) the electrons drift into a region of high electric field where they are accelerated, and their increased energy liberates further electron-ion pairs, usually increasing the number of free electrons by a factor of over 10^3. This process is referred to as an avalanche. Finally the electron cloud is incident on the anode, and is registered by the amplification system. The energy of the incident X-ray determines the size of the charge cloud produced, and hence the size of the electrical spike produced.

Unfortunately such a system is not particularly precise in its ability to determine the energy of the incident X-ray, with 15 % being a typical energy resolution. This is so poor because of the statistical variance in the number of electrons liberated by the incident X-ray, and also a similar variance in the number of electrons generated in the avalanche stage. The quantum efficiency of such detectors, however can be tailored to be near unity over a given an energy range. In the low energy regime (1-2 KeV) the quantum efficiency is limited by X-ray absorption in the window material, and in the high energy regime (10-20 KeV) the limitation is posed by the increasing transparency of the gas. The window material can be replaced by a plastic, which provides more transparency at low energy, making detection at as low as 0.1 KeV possible, at the cost of a greater permeability for the enclosed gas. At the high energy end it is possible to pressurise the gas to a few atmospheres to decrease transparency, and hence enable operation up to 100 KeV. Position sensitivity in one axis can be developed by having multiple anodes, and in the other axis by sensing how much charge "emerges" from each end of the anode. Alternatively innovations such as the wedge and strip anode allow spatial resolution as good as 150 μm to be obtainable.

In the gas scintillation proportional counter (GSPC) there is no high electric field region to cause the charge avalanche. Instead electron clouds create light in a region where the electric field is just sufficient to excite the gas. The scintillation light generated is measured by an arrangement of photomultiplier tubes, which determine X-ray energy by the total light intensity, and position by the relative amount of light arriving at each tube. Because of the lack of the gas multiplication avalanche stage, the energy resolution of GSPCs have a slightly improved energy resolution of nearer to 9 %, with measured values of 7 % possible. The spatial resolution of such a system is of the order of 900 μm at 10 KeV, and is as low as 2000 μm at 1 KeV.

1.2.2 Microchannel Plates

The microchannel plate (MCP) consists of a number of lead glass tubes bundled together. The internal diameter of these tubes is usually around 12 μm, and the center-to-center spacing 15 μm. X-rays are incident perpendicular to the plate surface, and liberate photo-electrons. A high electric field is generated between the opposite faces of the plate, and this causes the electrons to move down the tubes, liberating further electrons en route. Usually two or more plates are stacked up to create a cascade process where electron gains of 10^7 are typical. An electron cloud then emerges from the lower surface of the stack, and its position is then located by an anode system, possibly of wedge and strip design again.

The chief advantage of the microchannel plate system is that spatial resolution is very high, and is limited only by the spacing and diameter of the tubes, hence a value of 20 μm is typical. The quantum efficiency of such devices is high, however the energy resolution is virtually non-existent.

1.2.3 Charge Coupled Devices

The charge coupled device (CCD) is an array of capacitors. Charge is deposited on these capacitors by the incidence of X-rays, and is stored there until a ramped electric field moves the rows of charge along to the edge of the array, where they are read by an amplifier. The charge resultant from a single X-ray incident on any of the pixels may be measured, and this is related to the energy of the photon. Each of these metal-oxide-silicon capacitors is formed by the deposition of electrodes on the surface of a silicon wafer, so the formed arrays are able to resolve 30 μm spatially, and also possess an energy resolution of approximately 50 eV. The quantum efficiency of CCDs can be higher than that of a gas-filled device, depending on the thickness of silicon involved.

1.2.4 X-ray Microcalorimeters

The simplest X-ray microcalorimeter operates by the measurement of the rise in temperature of a semiconductor that results from the incidence of an X-ray photon. To avoid the complications that arise from X-ray thermalisation in a semiconductor, a thermalising medium is often strongly bonded to the semiconductor, and used to convert the X-ray energy into thermal energy. The resistance change of the semiconductor is measured by passing a small current through it, and the change in this current yields the temperature change. When operated at a temperature as low as 100 mK, the theoretical limit for energy resolution is estimated at 4 eV, and FWHMs of 10 eV have already been observed. Position resolution for these devices will depend on the development of arrays, however an element width of less than 0.1 mm seems unlikely at this point. The quantum efficiency of microcalorimeters is near-unity - for a given energy range of incident X-rays it is possible to design the absorber in such a way as to absorb all incident X-rays, with the only limitations being the small surface area, and the necessity of keeping the heat capacity of the device, and hence the size of the absorber, as small as possible.

1.2.5 Comparisons

Clearly the factor which is most in favour of X-ray microcalorimeters is the excellent energy resolution obtainable. However, despite the factor of 5 advantage of the microcalorimeter over the CCD in terms of energy resolution, the spatial resolution of the CCD is approximately 5 times better than that of the microcalorimeter, and hence is preferable in imaging applications, although for purely imaging applications where no energy resolution is required, the microchannel plate would appear to be the superior device. Compared to these three detector systems, the proportional counters have been somewhat left behind by progress, with neither the spatial resolution nor the energy resolution able to compete. The strongest feature of each is only comparable with the weakest features of the microcalorimeter and the CCD.

1.3 Review of Micro-calorimetry Work

1.3.1 *GSFC / NASA* Collaboration

In 1984[1] Moseley, Mather & McCammon suggested the use of a silicon arsenide wafer with a thermalising layer of aluminium as a spectrometer. The realisation in work of the time that at 300 mK such detectors are limited only by thermodynamic fluctuations in the system led to an increased urgency in such research, and in their paper, the group proposed a suitable device. They estimated that the theoretical limiting resolution for any such device is 1.1 eV FWHM.

In the same year[2], they demonstrated an antimony/boron-doped silicon detector at 300 mK, with an $^{55}_{26}$Fe source, and found a FWHM of 350 eV. This was reduced to 270 eV by the elimination of multiple-pulse events. Theoretically, the group estimated a resolution of 177 eV, and attributed the difference to amplifier noise and the non-optimal filtering used.

The following year[3], the collaboration presented the results of experiments with neutron transmutation doped germanium detectors at 300 mK, which yielded a FWHM of 130-170 eV. Three different forms of support for the detector were used in this run. In one case 0.3 mm brass wire was used, in another 1 mm quartz fibre was used, and in the third a 1 mm bundle of superconductor-coated carbon fibre. In the first and third cases the support was also used as the thermal/electrical link, whereas for the quartz support, 0.25 mm superconductor coated carbon fibre was used. The group also experimented with ion-implanted silicon, which has the advantage of lower heat capacity, but experienced an unexpected broadening of spectral lines, due to a varying amount of the photon energy being sensed in events. The required solution was to detect all of the energy being deposited by incident X-ray photons, and the need for a thermalising medium was recognised. Such a medium would consist of a material connected to the detector semiconductor detector, acting to thermalise the incident X-ray.

Later in 1985[4] investigation moved towards the possibility of using X-ray microcalorimeters in the AXAF mission, backed by a space-qualified Adiabatic De-

magnetisation Refrigerator (ADR). The problem concerning the conversion of X-ray energy to thermal energy in the detector was raised again, and the materials gold and silver were considered for use as absorbers. However, the large free-electron heat capacity of normal metals gave an unacceptably high level of thermal noise, and a different material was considered. Bismuth was decided upon, and a 2 μm layer was evaporated onto the back of a silicon thermistor. Tested with the $^{55}_{26}$Fe source, this yielded a FWHM of 38 eV at a temperature of 98 mK.

In 1987[5], Mercury Cadmium Telluride (HgCdTe or MCT) was being used as the thermalising element of a detector based on ion-implanted silicon. This detector was connected to a 80 mK heat bath by 20 μm aluminium wire, and demonstrated a FWHM of 17.4 eV. This detector, used on the $^{55}_{26}$Fe source, was able to demonstrate the separation of the $^{55}_{25}$Mn Kα line into the Kα_1 and Kα_2 elements. In this arrangement epoxy was used to connect the HgCdTe absorber to the silicon, and made a large contribution to the heat capacity of the device. With this in mind, consideration was given to the construction of a monolithic silicon detector. A monolithic detector would be created by the implantation of phosphorus and boron ions onto silicon wafer. Although this increases the specific heat capacity of the material, it is possible to make it much smaller in size.

Further thought was given to the choice of absorber materials. HgCdTe is a semiconductor, and had a 60 meV bandgap in use, which seemed to give about 0.2 % broadening. Removing Cd from the compound would have eliminated this gap, but reduced the Debye temperature of the material to 140 K, thus making its specific heat unacceptably high. Superconductors at less than one tenth of their critical temperature have negligably low electronic heat capacity, but deposited energy tends to form long-lived quasi-particles.

In 1988[6] results showed a discrepancy between measured FWHM of pulses and baseline noise of 11 eV in quadrature, and it was suggested that this was due to charge-trapping in the HgCdTe being used as absorber. (Baseline noise is the noise present in the detector which is present whether an X-ray is incident on the detector or not. Additional noise to this is contributed by the process

of thermalisation.) Absorber material was addressed further, and an alternative candidate suggested was the superconductor α-SnGe.

In 1992, the collaboration presented its results with Si detectors[7], where they had achieved a FWHM of 10.3 eV with the $^{55}_{26}$Fe source, applying some deconvolution processing. Some superconductors were suggested as suitable absorbing media, and results with Tin were given.

The most recent publication from this collaboration[8] details efforts to devise a 1 element by 12 element array from a silicon wafer, and gives a newly obtained deconvolved FWHM of 7.3 eV.

1.3.2 *Lawrence Livermore National Laboratory (LLNL)*

The work of this collaborative group developed from their involvement in infra-red calorimetry.

In 1990[10], *LLNL* was working with neutron transmutation doped germanium (NTD Ge) as a resistive microcalorimeter, and was attempting to explain the unexpected current-voltage behaviour of the material. In the same year a FWHM of 19 eV was demonstrated by the group, which included 12 eV of electronic noise.

1.3.3 *University of London* Collaboration

The earliest reference to the University of London collaboration on X-ray microcalorimetry is in 1987. The collaboration originally grew from the interest of (then) *Queen Mary College* in infra-red calorimetry, and the interest of *Mullard Space Science Laboratory* (a department of *University College London*) in new X-ray detector technology. The University used a ^{3}He cryostat to obtain temperatures in the region of 300 mK, and tested calorimeters optimised for use as infra-red detectors with a $^{55}_{26}$Fe source. Initial results showed a FWHM of 357 eV, with baseline noise of 330 eV.

From this point, the group developed an ADR with the assistance of Cochise Inc., to enable temperatures of 100 mK to be reached on a regular basis. At

the same time as this was under development, E. Haller of *LLNL* supplied the collaboration with a sample of NTD Ge, which was used to build a 100 mK infrared detector. Using this detector in a run in November 1991 showed that the FWHM at 200 mK was 288 eV, with a baseline FWHM of 190 eV, and at 100 mK, FWHM was 241 eV, with a baseline FWHM of 83 eV. Clearly the improvement expected by a lower operating temperature had not been realised, and the reason for this was suspected to be the presence of electron traps in the detector material. To avoid these traps, it was proposed to deposit a layer of Tin onto the detector surface, as a thermalising medium.

In 1992, Imperial College (IC) became involved in the collaboration as a result of their involvement in dark matter detectors. IC fabricate silicon detectors by epitaxial chemical vapour deposition with Arsenic, which have an advantage over germanium-based detectors in having a specific heat a factor of 100 lower.

1.4 Other Next-generation X-ray Detectors

1.4.1 Superconducting Tunnelling Junctions

Superconducting Tunnel Junctions (STJs) are similar in nature to microcalorimeters in that an X-ray imparts energy to a crystal, which then experiences a change in its electrical properties. In the case of a superconductor below a its critical temperature the energy gaps between bands are as small as, for example 3 meV in niobium, as compared to about 1 eV for semiconductors, and so a vast number of free electrons are created by the impact and thermalisation of an X-ray. The limitation of statistical variation in the number of charge-carriers produced, therefore is somewhat reduced. The initial photo-absorption causes the creation of a number of quasi-particle charge-carriers, each of an energy greater than 100 meV, which then emit phonons as a mechanism of losing energy. Since the Debye energy is much greater than the superconductor energy gap, the phonons produced in the X-ray interactions with charge-carriers can themselves produce charge-carriers, greatly reducing the amount of energy lost in the system by phonon

loss.

The result of this is that the resolution possibility of such a device is statistically set by the number of charge-carriers created, as detailed in Section 2.4.7, and in the case of STJs could therefore be as low as a resolution of 4 eV.

In practice, the method used for determining the number of free charge carriers available in the material is to use a quantum mechanical approach. Two overlapping layers of the superconductor are separated by a thin insulating layer. A bias voltage is applied across the outer layers, and tunnelling allows a current to pass between them. The level of this current is determined by the density of charge carriers present. Charge carrier density is affected by the deposition of energy associated with an X-ray impact for a few microseconds, and hence the bias current through the junction can be monitored.

Finkbeiner et al[12] worked with aluminium STJs, and in 1991 claimed resolutions of 3.3 % with the $^{55}_{26}$Fe source, which correlates to about 200 eV, at 276 mK. Hübner et al[11] used a niobium device, and achieved a resolution of 100 eV in 1993.

1.4.2 Dielectric Microcalorimeters

The development of dielectric microcalorimeters[13] arose chiefly out of the desire to have the high resolution of resistive microcalorimeters, but without the attendant Johnson noise. Dielectric detectors consist of a material with temperature-dependent dielectric properties. The X-ray thermalisation energy is imparted to a dielectric material, which forms the dielectric layer in a capacitor. The measurement of the induced change in capacitance yields the temperature change after calibration has been established, and one can proceed to analyse the temperature curve as with a resistive microcalorimeter.

A paper produced by the Centre in 1988[9] addressed the idea of applying then current calorimetry techniques to the X-ray field. This paper acknowledges the failings of thermistor-type calorimeters in use as X-ray microcalorimeters, and suggests that dielectric microcalorimeters may be a more suitable technology for

this application, citing some predicted detector performances which showed that a dielectric solution would have at least a factor of two improvement in FWHM. The highest resolution the paper conceived for a dielectric was 3 eV, and more interestingly, predicted that a FWHM of 17 eV should be obtainable at 300 mK, which would obviate the problems addressed later in this thesis of cooling in a space environment - only a pumped ^{3}He dewar would be required.

The early calculations of the *LLNL* group suggested that a dielectric device operated at 300 mK would offer a similar resolution to a resistive device operated at 100 mK. The initial tests made on the ferroelectric material KTN ($KTa_{1-x}Nb_xO_3$,x=0.12) were with infra-red LED pulses and 6 MeV alpha particles, and so little can be inferred from these results for the future implications of this device in X-ray detection, however it was clear that a non-thermal mechanism was responsible for the detection of alpha particles, and this phenomenon would have to be further explored before the device could become viable.

1.4.3 Kinetic Inductance Microcalorimeters

Kinetic inductance thermometers are another development from the *LLNL* which exploits the temperature dependence of Kinetic Inductance (KI). KI arises from the inertial mass of Cooper pairs in a superconductor, and the quantity of pairs present in a superconductor is dependent on the ambient temperature, hence kinetic inductance is a good measure of temperature. The device constructed by the *LLNL* consists of an iridium groundplane at 104 mK, on a diamond substrate. The dielectric over the groundplate was silicon monoxide, and the top layer was a niobium stripline. To absorb X-rays a slab of niobium was attached to the underside of the diamond substrate. The exact construction of the device and the choice of operating temperature is dependent on the heat capacity of the device, the maximum energy X-ray to be studied, and the required energy resolution. Whilst signal from the detector is maximized by operating at a temperature as close to the critical temperature as possible, it is essential that the energy of any incident X-ray should not bring the temperature of the superconductor over the

critical temperature, which in the case of this detector is 110 mK.

Various amplification systems are considered for this device, including a DC bias supported by a Superconducting Quantum Interference Device (SQUID), which requires reducing the efficiency of the thermal link between the absorber and the detector proper, to reduce the data rate from the detector to the electronics. Another amplification system operates on AC, and is essentially a potential divider, with the detector and a bias resistor in series, and a FET amplifier buffering the output impedance. In a third configuration, the inductance of the detector is used as part of a tuned circuit, and altering the inductance alters the resonance frequency, which is determined by a phase-locked loop. This is the system which supplies the least electronic noise to the output.

Bibliography

[1] *Thermal Detectors as X-ray Spectrometers* - S.H. Moseley, J.C. Mather, D. McCammon, J. Appl. Phys., Vol.56 No.5 pp.1257–1262, September 1984.

[2] *Experimental Tests of a single-photon calorimeter for X-ray Spectroscopy* - D. McCammon, S.H. Moseley, J.C. Mather, R.F. Mushotzky, J. Appl. Phys., Vol.56

[3] *Thermal Detectors as Single Photon X-ray Spectrometers* - S. Harvey Moseley, R.L. Kelley, J.C. Mather, R.F. Mushotzky, A.E. Szymkowiak, D. McCammon, IEEE Transactions on Nuclear Science, Vol. NS-32 No.1 pp.134–138, February 1985.

[4] *The GSFC/Wisconsin X-ray Spectroscopy Investigation for AXAF* - S.S. Holt, R.L. Kelley, S.H. Moseley, R.F. Mushotzky, A.E. Szymkowiak, D. McCammon, M. Juda, J. Zhang, in *Second International Symposium on Optical and Electro-Optical Science and Engineering* pub. December 1985.

[5] *Thermal Detectors for High Resolution Spectroscopy* - D. McCammon, M. Juda, J. Zhang, S.S. Holt, R.L. Kelley, S.H. Moseley, A.E. Szymkowiak, Japanese Journal of Applied Physics, Vol.26, Supplement 26-3, 1987.

[6] *Advances towards High Spectral Resolution Quantum X-ray Calorimetry* - S.H.Moseley, R.L. Kelley, R.L. Schoelkopf, A.E. Szymkowiak, D. McCammon, J. Zhang, IEEE Transactions on Nuclear Science, Vol.35 No.1 pp.59–64, February 1988.

[7] *X-ray microcalorimeters - principles and performance* - S.H. Moseley, M. Juda, R.L. Kelley, D. McCammon, C.K. Stahle, A.E. Szymkowiak, J. Zhang, Proceedings of an ESA Symposium on Photon Detectors for Space Instrumentation, at Noordwijk 10-12 November 1992, ESA SP-356, pp.13-19

[8] *Thermal Calorimeters for high resolution X-ray spectroscopy* - D. McCammon, W. Cui, M. Juda, J. Morgenthaler, J. Zhang, R.L. Kelley, S.S. Holt, G.M. Madejski, S.H. Moseley, A.E. Szymkowiak, Nucl. Inst. Meth. A326 (1993) pp.157-165

[9] *A New Microcalorimeter Concept for Photon Counting X-ray Spectroscopy* - Eric H. Silver, Simon E. Labov, F. Goulding, N. Madden, D. Landis, J. Beeman, Nuclear Instruments and Methods in Physics Research, Vol. A277 pp.657–663, 1989.

[10] *Electrical and Thermal properties of neutron-transmutation-doped Ge at 20 mK* - Ning Wang, F.C. Wellstood, B. Sadoulet, E.E. Haller, J. Beeman, Physical Review B, Vol.41, No.6, pp.3761, 15 February 1990-II

[11] *Superconducting Tunnel Junctions as Photon Counting Detectors* - P. Hübner, N. Rando, A. Peacock, P. Videler, A. van Dordrecht, J. Lumley, EUV, X-Ray and Gamma-Ray Instrumentation for Astronomy IV (Proceedings from SPIE's Annual Meeting in San Diego, 1993)

[12] *Superconducting aluminium tunnel junctions with indium absorbers for low-energy X-ray spectroscopy* - F. Finkbeiner, A. Hahn, W. Heeringa, P. Jany, H.O. Klages and T. Strobelt, Nuclear Instruments and Methods in Physics Research A306, pp.215-219, 1991

[13] *Test results of a prototype dielectric microcalorimeter* - T.E. Pfafman, E. Silver, S. Labov, J.Beeman, F. Goulding, W. Hansen, D. Landis, N. Madden, SPIE Vol.1344 pp.302, EUV, X-Ray, and Gamma-Ray Instrumentation for Astronomy 1990

[14] *Position Sensitive Detectors in X-ray Astronomy* - J.L. Culhane, Nuclear Instruments and Methods in Physics Research A310 (1991) 1-13, pp.1

[15] *Development of X-ray Calorimetric Detectors and Data Processing Techniques at London University* - I.D. Hepburn, P.A.R. Ade, M.J. Griffin, W.S. Holland at Queen Mary College, and J.L. Culhane, R. Kessel, D.M. Walton at Mullard Space Science Laboratory, University College London, in the book *Low Temperature Detectors for Neutrinos and Dark Matter-II* published by *Frontieres*, 1988. Edited by L. Gonzalez-Mestres and D. Perret-Gallix.

[16] *Thermal Detectors for X-ray Astronomy* - Stephen S. Holt, Pub. Laboratory for High Energy Astrophysics, NASA/GSFC, Greenbelt, MD, USA, 1989(?).

[17] *Superconducting Tunnelling Junction Detectors* - A. Zehnder, C.W. Hagen, W. Rothmund, SPIE Vol.1344 pp.286, EUV, X-Ray, and Gamma-Ray Instrumentation for Astronomy 1990

[18] *Application of kinetic inductance thermometers to x-ray calorimetry* - Yolanda C. Wai, Simon E. Labov, Eric H. Silver, SPIE Vol.1344 pp.314, EUV, X-Ray, and Gamma-Ray Instrumentation for Astronomy 1990

[19] D. Twerenbold, 1986, Europhys. Letts 1. (1986), 209-214

[20] H. Kraus, C. Jochum, B. Kemmather, M. Gutsche, F. v.Feilitzsch, R.L. Mossbauer, Nucl. Inst. Meth. A326, 1993, 177-189

Chapter 2

Principles of X-ray Microcalorimetry

2.1 The Basic Process

2.1.1 Semiconductivity, The Band Theory of Solids

The band theory of solids is a means of understanding the transport of electrons. When atoms are clustered closely together, the energy level diagrams for each atom become distorted, such that they are perturbed away from the normal levels. Hence in the system, an energy level in a group of atoms spreads to become an energy band. Higher energy valence levels become the widest bands, whereas lower levels, closer physically to the atoms they pertain to, are less affected by the electric fields of other atoms, and are spread less. The situation in conductors is that there is a partially filled band such that electrons can pass from one atom to another with only the slight amount of energy supplied by an electric field. In insulators and semiconductors a band, called the valence band, is completely full. This means that electrons cannot move about, since movement to a neighbouring atom would mean moving to an already occupied state, which is not allowed. The difference between semiconductors and insulators is that, in semiconductors, the next level up, the conduction level, is very close to the valence level, a gap of 1 eV

or less. At finite temperatures the thermal energy imparted to electrons allows them to jump into the conduction band. These three conditions are illustrated in Figure 2.1.

In the cases of silicon and germanium, the atoms are arranged into tetrahedral structures, and covalent bonds are formed between neighbouring atoms. A small amount of energy (1.1 eV for Si, 0.7 eV for Ge) is required to break one of these bonds and free an electron. This is the energy gap between the valence and conduction bands. At room temperature, therefore, a large number of electrons are freed, and this number increases rapidly with temperature. The hole left by a vacated electron will be filled by a neighbouring electron, and the hole left there will also be filled, so that the hole also travels. The hole serves as a positive charge carrier. In pure semiconductors there are as many holes as electrons, and this is referred to as intrinsic conductivity.

Extrinsic conductivity occurs when an impurity is introduced, for example if some arsenic (group V) is added to some molten germanium. As has five valence electrons, and hence the loose one in a Ge structure has a bonding energy of only 0.01 eV. This electron easily escapes and becomes free charge. There is no hole, however, so only the electron is the charge carrier. At normal temperatures very few Ge atom electrons can escape and conduct, so even a 1 in 10^{10} concentration of As makes the As electrons the majority carrier, and the material is called an n-type semiconductor.

On the other hand, if gallium, a group III element with three valence electrons is used, then the atom steals an electron from neighbouring atoms, and forms a hole, which is mobile. This type of semiconductor is then called p-type, since the positively charged holes are the majority carriers.

At very low temperatures, for example below 300 mK, conduction in semiconductors occurs by a slightly different means. At this temperature charge carriers are frozen out, or trapped on dopant sites. If the impurity concentration is carefully chosen, then the energy gap between sites is only just too great for charge carriers to cross, and transfer is only possible by tunnelling, or "phonon-assisted

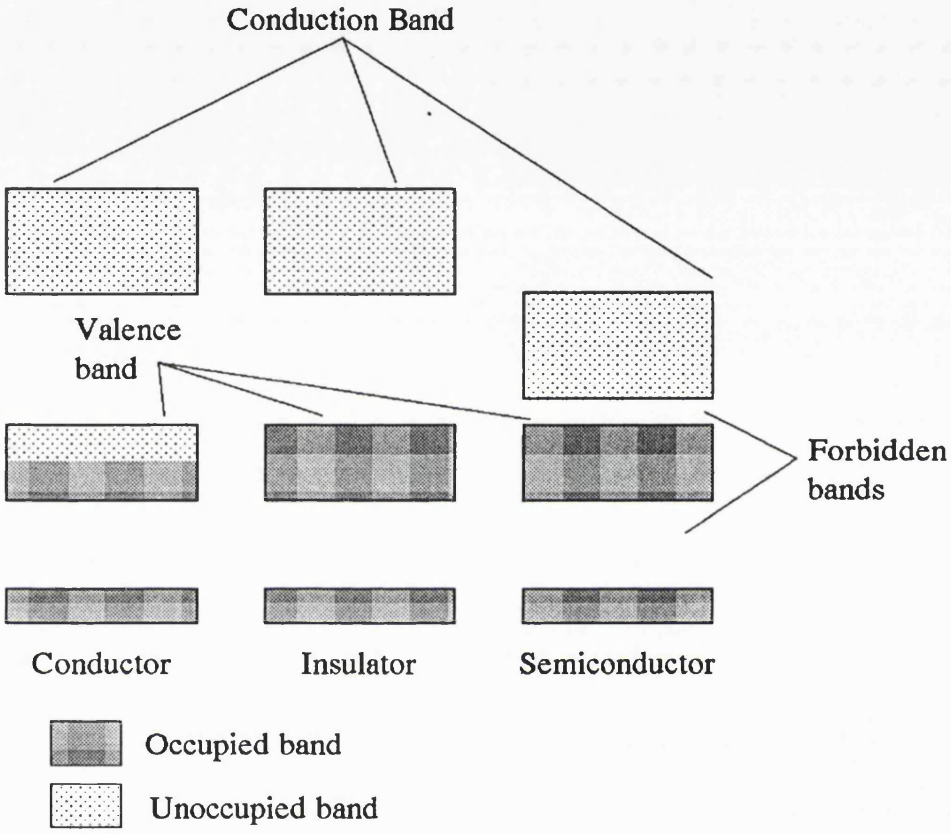

Figure 2.1: *Illustration of the Band Theory of Semiconduction*

hopping", which occurs when a high energy phonon imparts energy to the charge carrier. This means that conduction in the material is a strong function of the number density and average energy of phonons present, and hence of temperature. The resistance of a doped material in this regime depends very strongly on the dopant concentration.

It can be seen from this that semiconductors make exceptionally good thermometers, and they have been in use for many years as detectors of infra-red radiation. In these detectors, a wafer of semiconductor is connected to a heat sink at a low temperature such as 0.3 K or 1.0 K, and the incoming flux of infrared photons

heats the wafer. By passing a bias current through it, it is possible to determine the resistance of the wafer, and with suitable calibration the amount of energy incident on the wafer is determinable. From this and filters to determine the frequency of photons permitted to reach the detector, the temperature of astronomical sources may be measured.

In X-ray microcalorimetry, a similar setup is used, but the received energy is from individual X-ray photons, rather than a continuous flux of infra-red radiation.

2.1.2 The Thermalisation of X-rays

When an X-ray is incident on an atom of, for example germanium, it causes the release of a photo-electron, or an Auger electron.

(Auger electrons are the result of energy being imparted to a K-shell electron. The K-shell electron is emitted, and an L-shell electron takes its place. The photon emitted by the transition is absorbed by an electron in the same atom, probably in the L-shell, ejecting it. In this way no radiation escapes from the atom, just two electrons, hence this is called a radiationless transition.)

These high energy electrons (or electron in the case of photo-electron emission) then lose their energy to phonons and electrons by repeated interactions with the lattice. The phonons then relax to an equilibrium distribution, which is observed as a rise in temperature. Since the wafer is connected to a heat sink, the temperature of the wafer then drops as the heat leaks to the sink.

In practice the arrangement shown in Figure 2.2 is also used. The X-ray is incident on an absorbing medium, which has a good thermal link to a piece of semiconductor, and quickly reaches thermal equilibrium with it. If the combined heat capacity of the medium and the semiconductor is represented by C, and the energy of the incident X-ray as ΔE, then the initial increase in the temperature of the medium and semiconductor ΔT is given by the equation

$$\Delta T = \frac{\Delta E}{C}$$

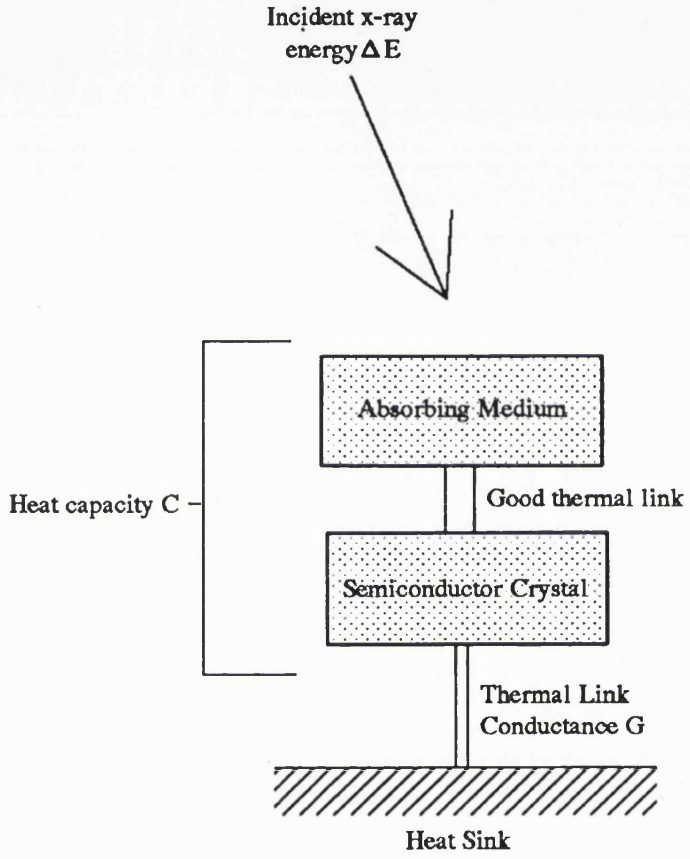

Figure 2.2: *Thermodynamic arrangement of microcalorimeter*

The raised temperature of the medium-semiconductor combination causes heat to flow to the heat sink along the thermal link with conductance G. In practice this thermal link is often the sense wires used to pass a bias current through the semiconductor, and hence determine its resistance.

By considering the rate of energy flow from the detector to the sink, it can be shown that the time taken for the detector to return to the heatsink temperature τ_{fall}, as shown in Figure 2.3 is independent of the photon energy, and is given

approximately by the equation

$$\tau_{fall} = \frac{C}{G}$$

A proof of this follows.

A conductive link exists between the detector and the bath such that energy passes from the detector to the sink as defined by this equation.

$$dQ = -\Delta T G dt$$

where

- Q is the amount of energy present in the material responsible for the temperature excess over the bath. Initially this will be ΔE, the energy deposited by the X-ray incidence. dQ is the change in this energy due to the thermal conduction between the detector and the bath in time dt.
- ΔT is the temperature difference between the detector and the bath $\Delta T = T_d - T_b$ where T_d is the detector temperature, and T_b is the bath temperature.
- G is the thermal conductance between the detector and the bath.

Above it has been shown that $\Delta T = \frac{\Delta E}{C}$, where ΔE is the energy of the incident X-ray. In the same manner, the difference in temperature between the detector and the bath is dependent on the amount of energy Q remaining from this incidence. ie. $\Delta T = \frac{Q}{C}$. Hence substituting this into the above,

$$dQ = -\frac{Q}{C} G dt$$

Hence

$$\frac{dQ}{Q} = -\frac{G}{C} dt$$

Integrating each side of this equation

$$\int \frac{dQ}{Q} = -\int \frac{G}{C} dt$$

And

$$\ln(Q) \doteq -\frac{G}{C}t + constant$$

We are free to define this constant as $\ln(K)$, hence

$$\ln(Q) = -\frac{G}{C}t + \ln(K)$$

$$\Rightarrow \ln\left(\frac{Q}{K}\right) = -\frac{G}{C}t$$

$$\Rightarrow \frac{Q}{K} = \exp\left(-\frac{G}{C}t\right)$$

In order to determine the constant K, use the boundary condition that at time $t = 0$, $Q = \Delta E = C\Delta T$. Hence

$$Q = \Delta E . \exp\left(-\frac{G}{C}t\right)$$

Since $\Delta T = \frac{Q}{C}$,

$$\Delta T = \frac{\Delta E}{C} \exp\left(-\frac{G}{C}t\right)$$

or

$$\Delta T = T_0 \exp\left(-\frac{G}{C}t\right)$$

We can define $\tau_{fall} = \frac{C}{G}$, and obtain

$$\Delta T = T_0 \exp\left(-\frac{t}{\tau_{fall}}\right)$$

Hence in time τ_{fall}, the pulse height will have fallen to 37 % of its initial height. This fall time is the major restriction on the event rate the detector can register, and is in the region of 1 ms, hence yielding an upper limit for event rate of about 1000 counts/second, and a more realistic limit of 100 counts/second in order to reduce the probability of more than one X-ray event co-inciding.

In fact, because the connections between the detector and the amplifier have a finite capacitance between them, of the order of 4 pF, and the amplifier has an input capacitance of 3 pF, the pulse shape output from the amplifier has a risetime τ_{rise}, which is dependent on this total capacitance and the resistance of the detector. The pulse which is observed is then of the form

$$V_c(t) = \left(\frac{V_0}{\left(1 - \frac{\tau_{rise}}{\tau_{fall}}\right)} \right) \left(e^{-\frac{t}{\tau_{fall}}} - e^{-\frac{t}{\tau_{rise}}} \right)$$

where

- R is the resistance of the detector.
- C is the total capacitance between the signal transmission lines.
- τ_{rise} is the rise time constant, the product of R and C.

With a typical detector resistance of 30 MΩ and a total input capacitance of 7 pF, the rise-time constant is of the order of 0.2 ms, compared to a fall time of approximately 0.5 ms, and such a pulse is shown in Figure 2.4. The effect of this rise-time is to reduce the peak height of the pulse, and this hence limits resolution.

It can be shown by differentiation that the time at which the pulse reaches its peak is given by

$$t_P = \frac{\tau_{rise}\tau_{fall} \ln\left(\frac{\tau_{rise}}{\tau_{fall}}\right)}{\tau_{rise} - \tau_{fall}}$$

In this case the combination of capacitance and resistance causes the peak height of the pulse to be only 31.3 % of that which would be the case if either the capacitance or resistance were zero, and this is a significant loss in resolution.

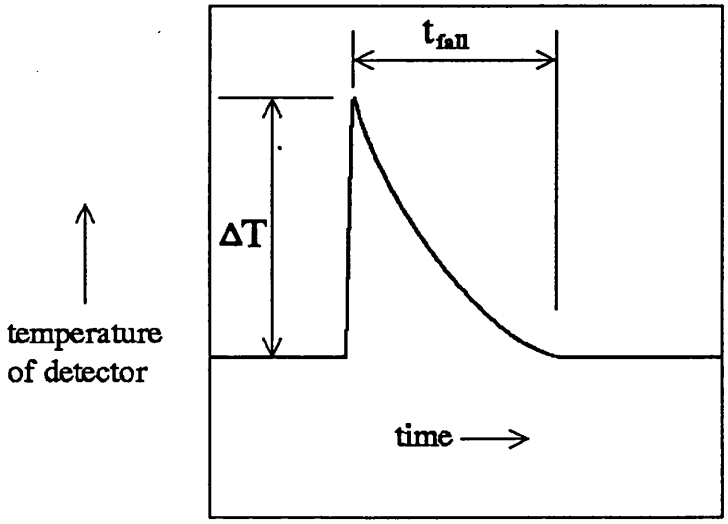

Figure 2.3: *Ideal output pulse from one X-ray event*

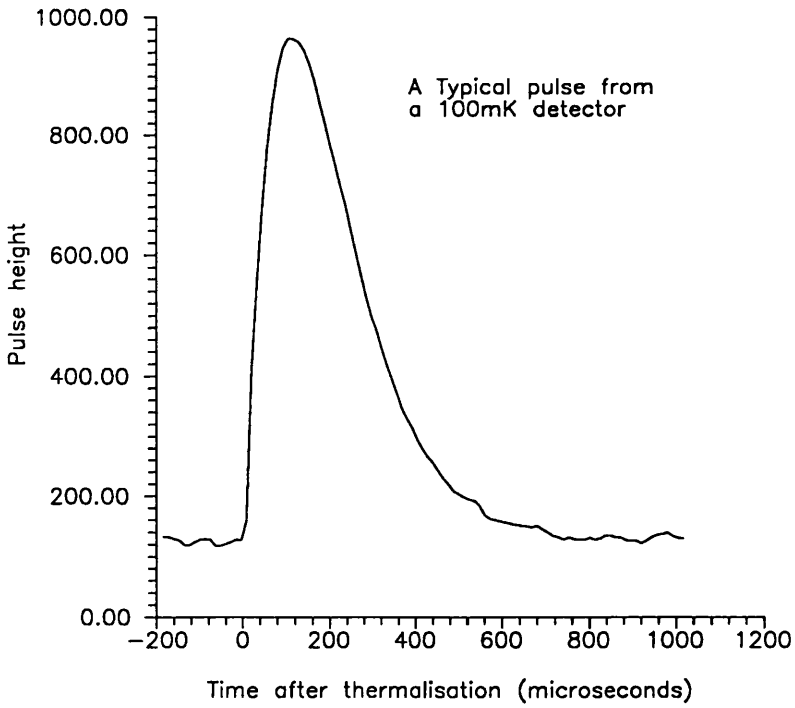

Figure 2.4: *A typical X-ray pulse*

2.1.3 The Hot Electron Effect

The theory of electron-phonon decoupling, or the hot electron effect was first proposed by Wang et al[1] to explain the non-linearity in current-potential difference characteristic of semiconductors at low temperatures. Previous work had been done by other authors describing this effect as it applied to metals.

Thermal equilibrium between the electrons and phonons in a material depends on the continuous exchange of phonons between electrons, and this is only possible if there are a number of final states available for electrons to descend into when emitting a phonon, or to rise into upon absorption.

The incidence of an X-ray upon the semiconductor, or the thermal conduction of heat from an absorber to the semiconductor affects the electrons in the material initially, and if the phonons are unable to reach thermal equilibrium with the electrons then the process of phonon-assisted hopping, the principal means of electrical conduction at this temperature will be retarded, and the dependence of resistance on temperature will be less strong. In the case of an X-ray incidence the large amount of energy deposited in the small area affected means that a large number of phonons are created initially, and this problem is less acute.

The hot electron effect is temperature dependent, and seems not to occur at temperatures as high as 100 mK.

2.1.4 Observation

In order to observe the effect of the X-ray on the detector, it is necessary to pass a small bias current through the semiconductor wafer, typically of the order of 1 nA. The electrical potential drop across the detector will be dependent on the resistance of the semiconductor, and this is put through a series of amplifiers, so that it can be digitised and recorded.

Figure 2.5 shows the system of amplification used by the University of London collaboration. The bias resistor and the bolometer are both in the 100 mK enclosure, and the FET is in the 1 K part, bringing the output impedance of the

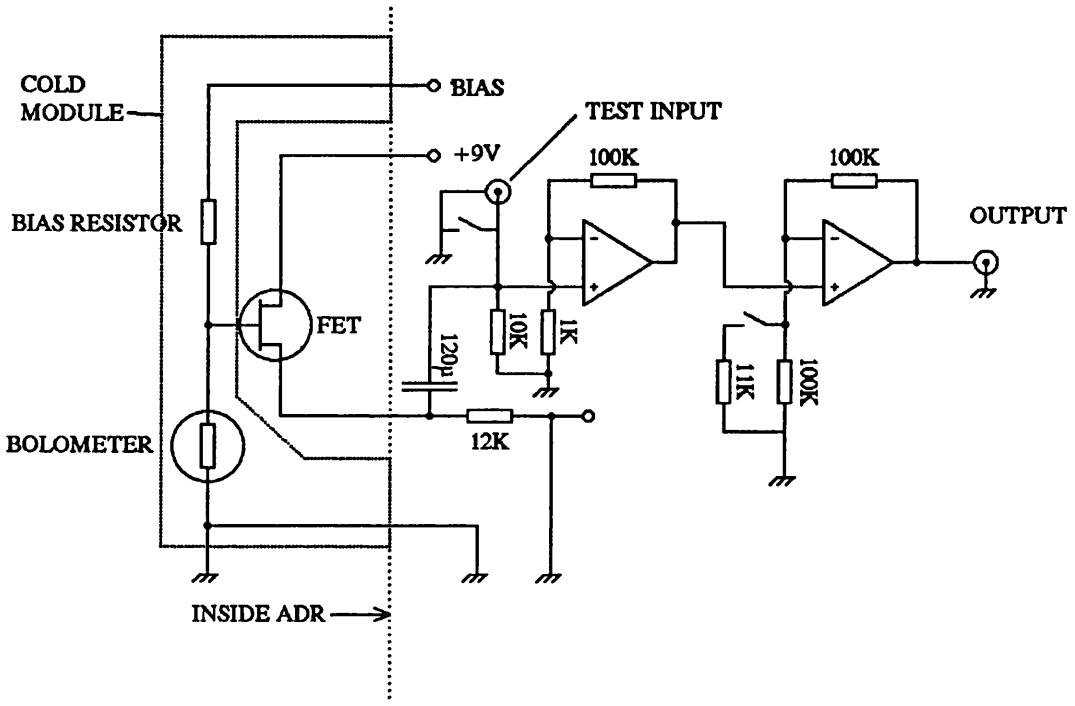

Figure 2.5: *The amplification system*

potential divider the two form down. The output of the FET is then put through a capacitor to remove the DC bias, and then through a pair of non-inverting amplifiers with a cascade gain switchable between 200 and 1000.

The digitisation stage can be performed by a digital storage oscilloscope, giving its output through an IEEE port, or by a simpler analogue to digital converter (ADC), with a suitable triggering mechanism.

2.2 Example System

2.2.1 Description

In the case of the X-ray microcalorimetry program developed by the *University of London* collaboration, the original material used was Neutron Transmutation Doped germanium (NTD Ge) supplied by E. Haller from the *Lawrence Livermore Laboratory.* The original sample[8] had dimensions of 0.12 mm × 0.10 mm × 0.30 mm, and an associated heat capacity calculated at 349 mK of 6.8 $pJ.K^{-1}$. Hence the incidence of a 6 KeV photon on the sample would cause a temperature increase of 0.00014 K or 0.14 mK.

2.2.2 Bolometer Characteristics

The ideal resistance for the bolometer is between 30 MΩ and 40 MΩ. The bias resistor is typically 120 MΩ or 240 MΩ, and a current of ideally 1 nA passes through the potential divider arrangement. If a detector has too great a resistance, then it has a high level of Johnson noise. Whilst increasing the current through the detector raises the temperature, and reduces the resistance to a more acceptable level, the temperature increase will cancel the advantage gained.

Additionally, a high resistance causes an increase in the pulse rise-time, as illustrated in Section 2.1.2, and reduces the peak height of the observed pulse.

Operating at a lower resistance, however, means that the resistance change with temperature will be less. The resultant change in potential difference across the detector will consequently be smaller, and the device resolution is diminished.

The bolometer resistance is therefore one of the most critical parameters of the device - too low a resistance and the resistance change with temperature drops, too high and the Johnson noise of the detector becomes more significant, and the rise time of the pulse is lengthened, making the pulse height lower.

The sample was indium-soldered to two 15 μm diameter brass wires of 1.50 mm length. These wires make the required electrical contact with the amplification

circuits, and also provide the thermal contact with the heat sink. In the early experiments a ^{3}He dewar was pumped on to obtain a heat bath of 300 mK, while in later years an Adiabatic Demagnetisation Refrigerator was supplied by *Cochise Inc.*, which enabled bath temperatures of 100 mK to be achieved. This is further discussed in Chapter 5.

2.2.3 Amplification Electronics

In this system, the ADR and the amplification electronics were enclosed in a large faraday cage, with a substantial earth, to eliminate the electrical interference from the substantial amount of electronic equipment present in the laboratory.

Electrical connections inside the ADR were made by high purity copper wire, lacquered to the cold surface by Ge varnish, but are now free-floating to avoid capacitance, a limitation to resolving power as described in Section 2.1.2.

2.2.4 Computer Simulation

As an diagnostic tool it was decided to develop a computer program to simulate the operation of a resistive X-ray microcalorimeter, based on the *University of London* device. The main features of this model included

- A simulation of the effect of varying temperature and current on the resistance of the germanium detector. This was achieved by recording the current-voltage curve of a sample at various temperatures, and using an extrapolation to calculate intermediate values.
- A calculation of the effect of bias current on the base temperature of operation of the detector. This was achieved by calculating the heating effect based on the power product VI.
- The rise in temperature of the detector due to the incidence of an X-ray photon. This is calculated by estimating the heat capacity of the detector

sample at the base temperature, and assuming that the X-ray energy is imparted instantaneously to the detector.

- The thermal connection between the detector sample and the heat bath was calculated from real data. By measuring the time constant of a real X-ray pulse as shown in Figure 2.3, it is possible to determine the conductance of the thermal link.

2.3 The Effects of Different Materials

Two materials have shown their respective merits in use as thermometers in X-ray microcalorimetry. Below I discuss the materials, methods used for their preparation, and the pros and cons of each of them.

2.3.1 Germanium

The *University of London* collaboration to date has used this material in the fabrication of its X-ray and infra-red microcalorimeters. The standard procedure for the doping of germanium with impurities is to bombard the material with a stream of thermal neutrons. Germanium has a number of stable isotopes present in its natural form, and these decay into dopant impurities after absorbing thermal neutrons. The dopant concentration is determined by the neutron flux, and to remove the damage caused by fast neutrons, thermal annealing is used. This means of preparation has been shown to yield a highly uniform concentration rivalled only by ion implantation.

In order to use the detector it is necessary to make an electrical contact to it, and this has to date been done by indium dots and gold wire, with a small speck of arsenic between the germanium and indium. A problem with this is that the change in contact area with repeated soldering leads to varying R-T curves, and the need to recalibrate. Future contacts will be ion-implanted, with mettalisation suitable for wire bonding, which should reduce excess noise.

2.3.2 Silicon

The addition of *Imperial College* to the *University of London* collaboration in 1992 has meant that the possibility of using silicon as the semiconductor has arisen. *Imperial College* has used calorimeters of a few grammes in mass as detectors for dark matter candidate particles.

The best obtained results with silicon involved the use of ion implanted silicon, which has a heat capacity a factor of 100 less than that of germanium. Ion implantation yields a thin doped region, of the order of 0.1 to 1.0 microns deep. However, ion-implantation yields a non-uniform doping density across the material, and as discussed in Section 2.1.1 the variable range hopping form of conduction that is dominant is very sensitive to doping level. This means that the creation of arrays would be extremely problematic, since all elements would have to have similar characteristics. Ion implantation typically creates a doped region of depth between 0.1 and 1.0 μm, and in this small a region the hot electron effect can be significant. An alternative method of doping might be epitaxial chemical vapour deposition (CVD), which can dope to a depth of 3 μm. In CVD a doped epitaxial layer is grown over the silicon wafer. Epitaxial growth can be obtained by molecular beam epitaxy, however CVD is more cost-effective.

There are two n-type materials which might be used to dope silicon with, phosphorus and arsenic. Of these, arsenic has a greater dependence of conductivity on temperature, and so is preferable for this application.

2.3.3 A Thermalising Medium

A problem with the thermalisation of an X-ray on the detector, is that of the trapping of electrons in the potential wells that exist at defects in the crystal lattice. At temperatures as high as 300 mK this is less significant, but at 100 mK electron kinetic energies are less, and the detector will be far more vulnerable to this problem. To overcome this, a thermalising medium is employed, and bonded to the semiconductor element of the detector. The trapping effect is discussed

later in Section 2.5.1, but the aim of the thermalising medium is to directly absorb the incident X-ray, and efficiently convert the energy from the released electrons into thermal phonons, within a short time.

The main design considerations for the thermalising medium are these:-

- High quantum efficiency over the energy range of the X-rays to be studied. The differing absorption characteristics of different materials can determine the necessary material. With a given material this defines the thickness required, and the efficient energy range.
- Low heat capacity. The lower the heat capacity, the greater will be the rise in temperature of the medium.
- Low Fluorescent Yield. The photo-electron liberated by the incident X-ray may escape from the material, as discussed later in Section 2.5.2, and the ideal absorber is chosen to keep this rate of loss low.

All metals are good thermalisers, and yield very low noise levels, however the free electrons in metals cause them to have unacceptably large specific heats. The more popular materials for this purpose used by the *GSFC* group are Mercury Cadmium Telluride (variously referred to as MCT, CMT and HgCdTe) and tin. Tin is useful because it is a superconductor at the low temperatures involved. HgCdTe is a semiconductor, and possesses a 60 mV bandgap which can trap energy. Although removing cadmium from the compound increases its specific heat, it does remove the bandgap, and reduce the energy variation. The use of superconductors is possible because well below the transition temperature, the electrons present in such materials are frozen into their ground state, and do not contribute to the heat capacity, leaving only the Debye contribution. The *GSFC* groups tests of superconductors as absorbers suggest that pure tin is the most promising.

A field in this section still in its infancy is the matter of the attachment of the absorber to the thermistor. Conventionally this has been done by the use of epoxy resin between the two parts, however, this is clearly unsatisfactory because

of the addition of this material's substantial heat capacity to the detector. Some research into deposition techniques has been undertaken, but results currently seem to lack repeatability.

2.4 Sources of Noise

The fundamental limitation on the resolution of an X-ray microcalorimeter is the random thermal fluctuations occurring within it. According to Moseley[2] and Holland[3] the effect of this on the resolution is given by

$$\Delta E = \xi T (k_B C)^{\frac{1}{2}}$$

where,

- ΔE is energy resolution
- ξ is a constant, characteristic of the material, dependent on its thermal properties. Its value is typically between 1 and 3, and a table of values for ξ can be found in [4].
- k_B is Boltzmann's constant.
- T is the operating temperature
- C is the heat capacity of the detector.

To convert this inherent resolution to Full Width at Half Maximum (FWHM), a factor of $2\sqrt{2\ln 2}$ is applied to the right hand side of this equation.

Below the Debye temperature of a solid, its specific heat is given with a good agreement by

$$C = \frac{12\pi^4 N}{5} . k_B . \frac{T^3}{T_D^3}$$

where T_D is the Debye temperature, and N is the number of unit cells in the solid. Substituting this into the FWHM equation gives a dependence of FWHM

on $T^{\frac{5}{2}}$. Such a strong dependence on temperature shows that a vastly improved resolution can be obtained from the detector by working at a lower temperature.

Additional sources of noise are as follows.

2.4.1 Johnson Noise from the Microcalorimeter

Johnson noise is the thermal noise present in any resistive circuit element, and has a flat frequency spectrum up to a certain level. The RMS noise generated by a resistance R at temperature T is given by

$$V_{nR} = (4.k_B.T.R.B)^{\frac{1}{2}}$$

where as usual, k_B is the Boltzmann constant, T is the absolute temperature of the resistor, R is the resistance, and B is the bandwidth under consideration. (B is often absorbed into the units of voltage noise). The instantaneous potential difference across the resistor has a Gaussian probability distribution.

2.4.2 Phonon Noise due to heat flow from the Microcalorimeter to the heat sink

This is statistical noise based on the fact that the carriers of heat energy from the detector to the heat sink carry a finite amount of energy each.

This is closely analogous to shot noise in electronics, where the finite charge of the electron is responsible for statistical noise.

Since the thermal conductance of the link is a fundamental parameter of the detector, the power P travelling along the link is

$$P = G.\Delta T$$

where ΔT is the temperature increase caused as before by the incidence of an X-ray photon. If the energy ϵ (shown later as about 1 meV) is required to create one phonon, then the rate at which phonons 'cross' the link can be given as

$$\frac{dN}{dt} = \frac{P}{\epsilon} = \frac{G.\Delta T}{\epsilon}$$

We require to know the amount of energy contained in these phonons. Although ΔT will vary, since the pulse is exponential in shape, it can be shown that the area under the shape $e^{-\frac{t}{\tau}}$ is τ, so we can simplify the process by assuming that ΔT remains at its maximum value for time τ, and then drops to zero.

so that in time τ, the number of phonons 'crossing' is

$$N = \frac{G.\Delta T.\tau}{\epsilon}$$

assuming Poissonian statistics, the uncertainty in N, ΔN is given by

$$\Delta N = \sqrt{N} = \sqrt{\frac{G\Delta T.\tau}{\epsilon}}$$

And since $\Delta T = \frac{\Delta Q}{C}$, where ΔE is the energy of the incident X-ray.

$$\Delta N = \sqrt{\frac{G.\Delta E.\tau}{\epsilon.C}}$$

and $\tau = \frac{C}{G}$

$$\Delta N = \sqrt{\frac{\Delta E}{\epsilon}}$$

Each of these phonons will carry a mean energy of ϵ, hence the energy uncertainty δE will be

$$\delta E = \sqrt{\epsilon.\Delta E}$$

As an example, we assume

$\epsilon = 1\,\text{meV} = 1.6\times10^{-22}$ J,

$\tau =$ about $5\,\text{ms} = 0.005\,\text{s}$

$\Delta E =$ around $6\,\text{KeV} = 9.6\times10^{-16}\,\text{J}$

so, $\delta E = 7 \times 10^{-21}\,\text{J} = 0.04\,\text{eV}$

2.4.3 Johnson Noise from the Bias Resistor

As described above, the Johnson noise is thermal noise dependent on the product of the temperature of operation and the resistance under consideration. The bias resistor in an arrangement as shown in Figure 2.5 will typically be much larger than the detector resistance, but because of 'shunting' the noise is negligible.

The Johnson noise arising in the detector can be represented as

$$J_D = \sqrt{(4k_BTR_D)}$$

and the Johnson noise arising in the bias resistor evident at the potential divider output point can be represented as

$$J_B = \sqrt{(4k_BTR_D)}(\frac{R_D}{R_L + R_D})$$

(NB. In Section 2.4.1, the bandwidth was included inside the term shown above. In this case it is absorbed into the units, and instead of the voltage noise, the units of J_D and J_B above are volts.hertz^{-1}, as opposed to V_{nR} described earlier, which has units volts.)

Hence the total Johnson noise evident is determined by addition in quadrature

$$J_T = \sqrt{\left((4k_BTR_D) + \left(\sqrt{(4k_BTR_D)}(\frac{R_D}{R_L + R_D})\right)^2\right)}$$

From comparing the bias noise to the detector noise, it is evident that it will always be at least a factor of 2 less than the detector noise.

2.4.4 Pre-amplifier Noise

The amplification system used by the detector system will contribute to the noise as perceived by the outside world. The voltage noise in amplifiers arises from the Johnson noise present in the device.

2.4.5 Excess noise

This is additional noise voltage generated by the effect of resistance fluctuations when an externally applied current flows through the resistor. It has a $\frac{1}{f}$ spectrum, and depends heavily on the construction of the resistor.

2.4.6 Spurious pulses

When the *University of London* collaboration started its X-ray detector tests at 300 mK, spurious pulses were noted that could be traced to two sources. To understand how these arose and were identified, it is necessary to define a 'genuine' pulse.

Since the work was done without a separate thermalising medium, a 'genuine' pulse is considered to be caused by an X-ray which has entered through the detector aperture, and has interacted directly with the NTD germanium substrate to produce the thermalisation effect. Typical pulses have a thermal time constant of the order of 500μs. The measured magnitude of such a pulse is dependent on the electronics involved, and of course on the energy of the responsible X-ray.

It was found that, in addition to the pulses expected from the standard source, two additional sources of pulses were present.

1. Pulses of a length of the order of 5000μs. Evidence suggests that these were caused by electrons striking the detector, approximately once every 8 minutes. Verification of this was found by bombardment of the detector with a β^- source, and observation of the same effect. This is quite easy to correct, since the large decay time is highly characteristic, and such pulses can be removed in the post-processing used in spectrum calculation.

2. Pulses which, although by their time-constant seem to be X-rays, show in the spectrum that they have not interacted with the substrate. The wide aperture of the detector initially allowed X-rays to interact with the brass wires and indium solder. This caused a general level of background on

the spectrum, and also an extra peak, in the case of the ^{55}Fe source just above the normal peaks at 5.9 and 6.5 KeV. This was verified when a lead aperture was installed to allow X-rays to access only the substrate, and the background and additional peak vanished.

2.4.7 Statistical Variation in the number of Phonons Created

On a more statistical basis, we may consider the process of phonon thermalisation. Consider an X-ray photon of energy ΔE, incident on the thermalising medium. Initially the X-ray produces either a photo-electron, or an Auger electron. The resultant electron then interacts with the atoms around it.

In the case of semiconductors, approximately 70 % of the energy of the subsequent electron interactions with atoms is immediately converted to phonons because of the nucleus recoil[5]. The remaining 30 % liberates electrons, and so 'traps' some energy, which is discussed later, however here we assume that recombination occurs fairly soon, and that all of the X-ray energy is converted into phonons.

To create each phonon requires energy ϵ. Eventually, the material will have a large number of phonons in it, with the energy per phonon becoming less, as thermal equilibrium between the phonons starts to establish itself. Eventually the energy of each phonon will be less than ϵ, and they no longer have sufficient energy to create further phonons. The number of phonons generated in this cascade process is

$$N = E/\epsilon$$

with an statistical uncertainty of

$$\delta N = \sqrt{F.E/\epsilon}$$

This equation is analogous to the equation for electron cascades in PSPCs and GSPCs, and exactly the equation used to describe the fundamental resolution of STJs, discussed in Section 1.4.1. It includes the Fano factor F used to describe the effect of multiple-collision events in the material. Although in general this

factor is around 0.2 for X-ray detectors, no attempt at a determination for F in microcalorimetry has been launched. In PSPCs ϵ stands for the energy to liberate an electron in the gas occupying the detector, which, as described in Section 1.2.1 is typically 30 eV.

Since this energy is much more than the energy needed to create a phonon, the number of phonons generated will be fundamentally higher for an incident X-ray photon of the same energy. This means that δN will be a smaller proportion of it than for electrons, and we have a higher resolution.

To show this mathematically...

If a measurement depends on a number of events N, and a Poissonion distribution occurs, then the uncertainty in the number of events is $\delta N = \sqrt{N}$. If E represents the total energy of the incident photon, and ϵ represents the ionisation energy in proportional counters, and the energy to create a phonon in the microcalorimeter.

$$N = \frac{E}{\epsilon}$$

$$\rightarrow \delta N = \sqrt{\frac{F.E}{\epsilon}}$$

$$\rightarrow \frac{\delta N}{N} = \frac{\sqrt{\frac{F.E}{\epsilon}}}{\frac{E}{\epsilon}}$$

$$= \frac{\sqrt{F}}{\sqrt{\frac{E}{\epsilon}}}$$

$$= \sqrt{\frac{F.\epsilon}{E}}$$

Now, since $\delta E = \frac{\delta N}{N}.E$

$$\delta E = \sqrt{\frac{F.\epsilon}{E}}.E = \frac{\sqrt{F}.E}{\sqrt{E}}.\sqrt{\epsilon}$$

$$\rightarrow \delta E = \sqrt{F.E.\epsilon}$$

This shows that the statistical resolution of any event-counting X-ray detection device will be the geometric mean of the energy to cause one event, and the energy of the incident photon. The Fano factor also plays a part in this equation, but will be constant for any given material.

To put numbers into this equation, we can consider on the one hand, the PSPC, which, ionises one atom of Xe for each 30 eV of the incident X-ray[7]. In the observation of an Iron line at 6KeV, taking the geometric mean shows us that a fundamental resolution of only 420 eV is the limit.

Doing a comparison with the microcalorimeter is slightly more difficult. Since we are considering a very cold situation, the temperature will be very much lower than the Debye temperature, and the most probable phonon wavelengths will be of the order of 100's to 1000's of the inter-atomic spacing in the material.

Since the current proposal is to use a Tin thermalising medium, we can consider the lattice spacing and speed of sound in Tin.

The speed of sound(c) in tin is $3320\,\mathrm{ms}^{-1}$. Since the inter-atomic spacing in tin is of the order of 10^{-10} m, we assume a typical phonon wavelength as 10^{-8}m. A typical phonon vibration frequency(ν) can be calculated from the equation $c = \nu\lambda$ as approximately 3×10^{11} Hz. Using the relation $E = h\nu$, this is equivalent to an energy of the order of 1 meV, which is in agreement with the phonon energy calculations of [5]. Putting this into the resolution equation yields a statistical resolution of approximately 1 eV.

2.5 Other Resolving Power Limitations

2.5.1 Electron Traps

At imperfections in a crystal lattice, deep potential wells occur, and electrons may be lost into these wells for times in excess of 1 ms, effectively removing the energy possessed by this electron from detection. The ability of electrons to escape from

such wells is dependent on their energy, and whilst at 300 mK this is not a great problem, at 100 mK it becomes more acute.

2.5.2 Photo-electron emission

The X-ray energy may be taken by a photo-electron, and escape from the detector before depositing its full energy. This will occur near the surface of the detector. The fraction which escapes is of the order of l_e/l_x, where l_x is the X-ray mean free path, and l_e is the electron range. This is maximum just above an absorption edge, and as a typical example is 6% for Si at 1.6 KeV. A solution for this problem would be to coating the detector with a low Z material, since such materials have a low l_e/l_x, however, this must be balanced against increasing heat capacity.

2.5.3 Radiative Losses

When an electron interacts with an atom, approximately 30 % of the energy is converted to freeing an electron, with only the remaining 70 % being converted to phonons. The free holes and electrons form excitons, bound hole-electron pairs which decay by the emission of phonons, photons or photo-electrons. Most of the decays of these excitons result in rapid thermalisation, but a small fraction are radiative. These photons will pass easily through the semiconductor, and will escape from the detector. If N photons escaped on average, then this would limit energy resolution to a proportionality to $\sqrt{N}$. However, we find that most excitons decay rapidly and non-radiatively. Hole-electron recombination by the Auger process is very fast (eg. 80 ns) compared to the radiative lifetime of 750 μs, so radiative decay does not occur to a significant extent. However, for some traps, the Auger process is forbidden, and in these cases there is a relatively high probability of the radiative decay. Three possible solutions to this problem are...

1. To produce a material which does not possess radiatively efficient traps.

2. To put a number of neutral donors in the crystal, to dominate the undesirable traps.

3. To metallize the external surface of the detector with Aluminium to prevent the photons lost by radiative decay from escaping.

2.5.4 Metastable states

If some of the energy were delayed beyond the readout time, then effectively it is lost, and shows up as a tail approximately ten times the length of the bulk of the pulse. Such a situation would be a long electron-hole recombination time, or a long exciton decay time. This would result in delayed thermalisation, and effectively lost energy. This in itself would not be a problem, since a constant loss in energy could be scaled, however, on each event, a variable amount of energy is lost.

A possible solution to this is, again, doping at a suitably high concentration that recombination rate is fast. If this is not possible, or desirable, then it may be possible to 'flash' the device, hence flooding the metastable states, and preventing them from absorbing further photons, just before the readout. This technique is unexplored, and it is unclear how it would be implemented in the case of X-rays.

2.5.5 Non-thermal phonon spectrum

It is unclear what the effect will be if the phonon spectrum is non-thermal. The key question is how the thermometers will operate. If the resistance change of the thermistor is a function of elastic strain energy density, then the energy spectrum of the phonons should not be relevant. However, if single quantum processes are important, for example the phonon-assisted hopping described earlier, the spectrum will be relevant.

2.5.6 Thermal Uniformity

To ensure a uniform response across the surface of the detector, the thermal time constant must be long in comparison with the equilibration time. The thermal

time constant is τ_{fall} from Section 2.1.2, where $\tau_{fall} = C/G$. This means the detector surface must be in thermal equilibrium well before the energy has leaked away. In Section 2.6.2 I show that this should not be a problem.

2.6 Future Developments

When considering the use of an X-ray microcalorimeter in the future, it is necessary that the device has advantages over detectors currently in common use. Whilst I have shown that the energy resolution of such a device is high, and the position resolution may also be comparable to its contemporaries, it will be necessary to address certain issues that need to be resolved before it will see a useful application.

2.6.1 Environment

Since the microcalorimeter will have to operate in space at a low temperature, long-term refrigeration devices will have to be developed, and I address this further in Chapters 6 and 7.

2.6.2 Arrays

Whilst the microcalorimeter would appear to lend itself chiefly to spectroscopic uses, it would greatly enhance its usefulness if it were developed into an imaging device. For this to occur, an array of devices will have to be devised. This is not going to be a trivial matter. Firstly, a thermal link must be present between each of the elements and the heat sink. This thermal link must be conductive enough that the heat is dissipated to the sink before any substantial heat flow occurs to surrounding elements. This places a limit on the physical connection between the elements of the array, which may be alleviated by more carefully considering the way the array is set out.

One means of setting up a reasonably homogeneous array would be at the point of fabrication. Assume we have a wafer of silicon about 5 mm square. If we are able to use CVD to make a few microns thick depth 5 mm square detector, then we can use plasma etching to cut an array from the wafer, say 8 by 8, each element 0.1 mm square, with a 0.1 mm gap between elements.

It may well be that this close an arrangement of elements will not be possible, if only because thermal contact must be established between each element and the bath separately, there should be effectively no contact between the neighbouring elements. This problem of the necessity of treating each element separately also comes up when determining a means of (1) Determining which element has been struck by a photon and (2) amplifying the output of the element such that it is useful. Whatever way these objectives are achieved, two electrical contacts must be made to each element, and a bias current must be passed along the wires through each element. These contacts may form the thermal link to the heat sink, which would have to be the amplification stage. A separate amplifier would be required for each element, which in the case illustrated in Figure 2.6 requires 64 amplifiers of as small an input capacitance as possible in a small area.

In order to reduce the number of wires used in the arrangement, it may be possible to arrange the array schematically as a potential divider, with a wire contact coming from between the detectors, as shown in Figure 2.6. It is clear that a vast number of wires are still involved in such an arrangement, but there is here only one wire per element, and this wire can double up as the thermal link. Unfortunately, this system has quite a large resistance, with each of the elements contributing approximately 40 MΩ of resistance, and in a system of 64 detectors set up in series with a 120 MΩ bias resistor in this manner, a total resistance of 2.68 GΩ is presented, and to maintain a current of 1 nA a potential difference of 2.68 V need be applied across the complete series.

McCammon et al have developed an array device [6] of 12 elements by 1 element, by etching and doping a wafer of silicon.

An alternative means of achieving a spatial array might be to build a 2 element by

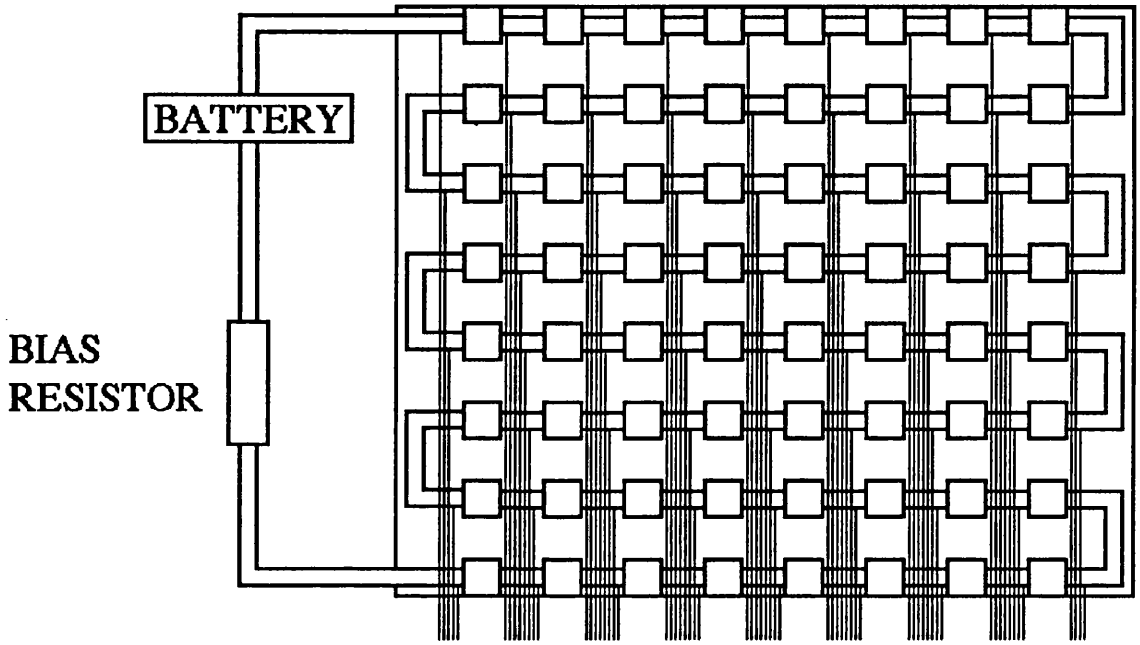

Figure 2.6: *Electrical connections to an array of elements.*

2 element array, and to mount a single absorbing medium onto all four elements, so that an X-ray incident anywhere on the absorber will yield some of its energy to each of the four detectors. The exact location of the incidence might then be calculated by the time delay between registering the temperature pulse on each of the detectors.

Unfortunately, elegant though this solution is in its simplicity, the time constant for an energy pulse from one element to another, assuming an element spacing of 0.1 mm, and a temperature increase caused by the incidence of an X-ray photon to be 0.1 mK, is in the region of 10^{-10} s, and this time is five orders of magnitude shorter than the pulse rise time, as demonstrated in Section 2.1.2. The time constant can be shown to be approximately

$$\tau_{element} = \frac{\Delta E \Delta x}{\Delta T K A}$$

where

- ΔE is, as before, the energy of the incident X-ray.
- Δx is the distance between the elements.
- ΔT is the temperature increase caused by the X-ray incidence.
- K is the thermal conductivity of the thermaliser.
- A is the cross-sectional area of the medium perpendicular to the direction of energy flow.

The small time constant not only removes the possibility of determining the position of the pulse by the time at which the temperature of each of the elements changes, it also means that the entire thermaliser will reach thermodynamic equilibrium so quickly that an equal amount of energy will be deposited in each of the elements, and determination of position by the partition of energy between the elements will not be possible. Because of this vast difference between $\tau_{element}$ and the amplifier response time, it is unlikely that a different material could be located that would be a suitable thermaliser, and would also have a substantially lower thermal conductance.

However, the positive side of this quick thermalisation time is that the temperature of the detector will equalise across its volume in a very small time as shown, and the concerns about the effects of a lack of thermal uniformity in Section 2.5.6 are unfounded.

Bibliography

[1] *Electrical and Thermal properties of neutron-transmutation-doped Ge at 20 mK* - Ning Wang, F.C. Wellstood, B. Sadoulet, E.E. Haller, J. Beeman, Physical Review B, Vol.41, No.6, pp.3761, 15 February 1990-II

[2] *Thermal Detectors as Single Photon X-ray Spectrometers* - S. Harvey Moseley, R.L. Kelley, J.C. Mather, R.F. Mushotzky, A.E. Szymkowiak, D. McCammon, IEEE Transactions on Nuclear Science, Vol. NS-32 No.1 pp.134–138, February 1985.

[3] *PhD Thesis* - W.S. Holland, Queen Mary College, University of London, Chapter 7, *Bolometric Detectors as X-Ray Calorimeters*, 1991

[4] *Thermal Detectors as X-ray Spectrometers* - S.H. Moseley, J.C. Mather, D. McCammon, J. Appl. Phys., Vol.56 No.5 pp.1257–1262, September 1984.

[5] *Particle Detection with Semiconductor Thermistors at Low Temperatures* - N. Wang, J. Beeman, A.N. Cleland, A. Cummings, E.E. Haller, A. Lange, R. Ross, B. Sadoulet, H. Steiner, T. Shutt, F.C. Wellstood, IEEE Transactions on Nuclear Science, Vol.36, No.1, February 1989, pp.852

[6] *Thermal Calorimeters for high resolution X-ray spectroscopy* - D. McCammon, W. Cui, M. Juda, J. Morgenthaler, J. Zhang, R.L. Kelley, S.S. Holt, G.M. Madejski, S.H. Moseley, A.E. Szymkowiak, Nucl. Inst. Meth. A326 (1993) pp.157-165

[7] *Position Sensitive Detectors in X-ray Astronomy* - J.L. Culhane, Nuclear Instruments and Methods in Physics Research A310 (1991) 1-13, pp.1

[8] *Thermal Detectors As X-Ray Calorimeters: Theoretical and Experimental Results and Data Processing Techniques* - R. Kessel, D.M. Walton, J.L. Culhane, W.S. Holland, I.D. Hepburn, P.A.R. Ade, M.J. Griffin, SPIE Vol.1140, X-ray Instrumentation (1989) pp.84

[9] *Composite Bolometers as Spectrometers for X-ray Astronomy* - N. Coron, G. Artzner, G. Danbieb, G. Jegoudez, J. Leblanc, J.P. Lepeltier, J.T. Deschamps, R. Rocchia, A. Tarrius, O. Testard, P.G. Hansen, B. Jonson, H.R. Ravn, H.H. Stroke, E. Turlot in *Second International Technical Symposium on Optical and Electro-Optical Applied Sciences and Engineering.*

[10] *Thermal Spectrometry of Particles and γ-rays with Cooled Composite Bolometers of Mass up to 25 grammes* - N. Coron, G. Artzner, P. de Marcillac, H. Stroke, A. Benoit, F. Amoudry, H. Ravn, B. Jonson, J.P. Torre, O. Testard, G. Dambier, J. Leblanc, G. Jegoudez, J.P. Lepeltier, Submitted for publication in *Superconducting and Low-temperature Particle Detectors* edited by G. Waysand, G. Chardin; Elsevier Sc. Publ., Amsterdam, 1989.

[11] *The Performance of MilliKelvin Si Bolometers As Xray and Exotic Particle Detectors* - C.C. Zammit, T.J. Sumner, M.J. Lea, P. Fozoomi, I.D. Hepburn, presented at EUV, Xray and Gamma-ray Instrumentation for Astronomy II, San Diego July 1991, and Proc. SPIE 1549

[12] *The development of Millikelvin Ge and Si bolometers for the UK dark matter programme* - C.C. Zammit, T.J. Sumner, A.D. Caplin at Imperial College, P. Stefanyi, M.J. Lea, J. Saunders, P. Fozooni at Royal Holloway

[13] *Variable Range Hopping Conductivity in Si:As Bolometers* - C.C. Zammit, A.D. Caplin at Imperial College, M.J. Lea, P. Fozooni, J. Kennefick, J. Saunders at Royal Holloway, Physica B 165 & 166 (1990) 317-318, North Holland

[14] *The Development of Millikelvin Silicon Bolometers for future X-ray array devices* - C.C. Zammit, T.J. Sumner at Imperial, I.D. Hepburn, P.A.R. Ade at

Queen Mary Westfield, Nuclear Instruments & Methods in Physics Research 00(1991) NIM0841P, North Holland

[15] *Solid State Physics* - J.S. Blakemore, Cambridge University Press, 2nd Edition.

[16] *X-ray microcalorimeters with germanium resistance thermometers* - S. Labov, E. Silver, T. Pfafman, Y. Wai, J. Beeman, F. Goulding, D. Landis, N. Madden, E. Haller, SPIE Vol.1334 EUV, X-ray, and Gamma-Ray Inst. for Astronomy (1990) pp. 295-301

[17] *Bias-induced nonlinearities in the dc I-V characteristics of neutron-transmutation-doped germanium at liquid-^{4}He temperatures* - T.W. Kenny, P.L. Richards, I.S. Park, E.E. Haller, J.W. Beeman, Phys.Rev B, Vol.39, No.12, 15 April 1989-II, pp. 8476-8482

Chapter 3

Data Processing Techniques

3.1 Initial Processing

3.1.1 Raw data form

When the pulses are captured by either a digitising storage oscilloscope or an Analogue to Digital Converter (ADC), they are converted into digital form. In the case of the oscilloscope, 8 bits are used in the conversion, yielding the possibility of 256 levels, and in the case of the ADC 12 bits are used, allowing 4096 possible levels. In order that the full benefit be had from this improvement in resolution, it is important that the ADC has a suitably amplified input.

The ADC continually monitors the input voltage level, supplying a digital conversion of this to the computer. The minimum time between samples possible by the ADC is about 1 μs. The desktop computer receives this data via a custom interface. Running a FORTRAN programme, it then puts this into a rotating buffer. The highest rate that computer is able to take a sample is approximately every 5μs, and in practice a time of 10μs is used, which is adequate to record 50 height readings of a 0.5 ms event. When the signal reaches a trigger level, the signal is recorded for a set number of samples, and the samples, preceded by the

pre-trigger data in the buffer, are stored as part of a file on floppy disk. Early files were comprised of 1200 pulses. Each pulse comprised of 600 bytes. Each of these bytes represents the height of the input pulse at a certain time, one channel. Approximately 50 of these channels show the pulse, and the remainder show the surrounding noise. In the later case of 12-bit sampling, two bytes are used for each channel. The first is the low-byte, the second the high-byte. To keep file size down, only 600 pulses are stored in the 12-bit files. Eight header identity bytes precede each pulse, and two footer bytes end it. Hence 8-bit files are of 732000 bytes length, and 12-bit files are of 726000 bytes length. The header and footer bytes are present because of the way FORTRAN handles files, and are discarded by the processing software described below.

The title of each file tells firstly the type of run used, an identifying number, and the date of the run the data was taken on. The identifying number starts at 1 each day. Original data files are given the suffix .DAT for clarity. For example, the file FE4.20.11.DAT is the fourth data file taken on the 20th November (in 1991), where the source used was $^{55}_{26}$Fe. The year is not specified in the filename because of restrictions in the disk operating system in the Archimedes used for receiving the pulses, and the VAX/VMS system used for storage and some processing.

The stages of processing described below were performed by programs written on an IBM PC compatible computer, which obtained the files by Ethernet transfer from a VAX/VMS archive.

3.1.2 Pulse Viewing

A programme, called DISPLAY, was written which enabled the user to visually inspect each of the pulses within a given .DAT file, without performing any processing on it.

3.1.3 Pulse height determination

The simplest and easiest manner to process the pulse data is to determine the height of each pulse. This is done by taking the average value of the few data points around the peak of the pulse. In this stage it is also wise to determine the structure of the background bias, and to subtract this from the height calculation. Plotting a pulse-height histogram yields an uncalibrated energy spectrum of the pulses. By knowing the energy of one or more of the X-rays being observed it is possible to calibrate this histogram in terms of energy.

Usually, the source $^{55}_{26}$Fe is used. This decays by electron capture into $^{55}_{25}$Mn, which emits two strong lines around 6 KeV, the details of which are in the later chapter on specific results. The resolvability of these lines, high event rate and familiarity with them makes these peaks useful as calibration points.

3.2 χ^2 Rejection of Non-conforming pulses

The first stage in processing any data is to first remove any extraneous noise. In Chapter 2 I described two mechanisms by which spurious pulses are generated. To this might be added the possibility of electronic noise from external equipment causing pulses in the amplification system between the detector and the digitisation. The pulse need only be long enough to trigger the digitiser for a spurious pulse to appear in the disk file. Another event that can disrupt processing is that two X-rays interact with the detector in quick succession. This will confuse any processing software, and should therefore be discarded.

It was therefore decided to employ a computer-based technique to reject those pulses which are clearly not generated by the simple interaction between an X-ray and the detector.

The means of rejection decided on was an adaptation of the χ^2 technique commonly used in fitting data. We start by assuming that we are dealing with the 600 or 1200 pulses that are found in one data file. Using these pulses we determine

the average pulse form over the 1200 or 600 pulses. Since the trigger level of the digitiser is constant throughout the run, it is unnecessary to consider any shift along the time axis. Although the technique assumes this, it does not assume that the baseline noise remains constant throughout the run. For each pulse the noise is removed by a fitting a quadratic regression to the noise-dominated regions of the sample, and subtracting the quadratic from all channels.

The calculation of the quadratic is done by using these standard equations.

$$b = \frac{([x]^2 - n[x^4]) + ([x][y] - [xy]n) - ([x][x^2] - n[x^3]) + ([x^2][y] - n[x^2y])}{([x]^2 - [x^2]n)([x^2]^2 - n[x^4]) - ([x][x^2] - [x^3]n)^2}$$

$$c = \frac{([y][x^2] - n[x^2y] - b([x^2][x] - n[x^3]))}{[x^2]^2 - n[x^4]}$$

$$a = \frac{([y] - [x]b - [x^2]c)}{n}$$

Where n is the number of bins. x above is along the time axis, y is the element height, and $[expression]$ means evaluate the mean value of *expression* over the region outside the influence of the pulse.

These equations calculate the constants a,b and c in the baseline equation

$$baseline(x) = a + bx + c^2$$

This background subtraction is only used when determining the average form of the pulses. Once an average form has been determined by using all the pulses, each of the pulses is individually compared to the average form by scaling the form up. The area underneath the real pulse is used to scale up the average to generate an expected form.

The average form for pulses is calculated as

$$\overline{x}_m = \frac{\sum x_{n,m}}{G}$$

where

- $x_{n,m}$ is the m_{th} element in pulse n
- The summation is performed only over those pulses not rejected.
- G is the number of pulses not rejected. Initially this will be all of the pulses in the files, but further iteration will reduce this number.

The area under pulse n, represented as A_n, is then

$$A_n = \sum_{m=L}^{m=U} (x_{n,m} - baseline)$$

where

- L and U are lower and upper limits set by the user, the end bins considered in the summation.
- *baseline* is calculated by fitting a quadratic equation to the parts of the averaged pulse not containing the pulse itself, as shown above.

The average area under a pulse $\overline{A}$ is then

$$\overline{A} = \frac{\sum A_n}{G}$$

where the summation is over all non-rejected pulses.

A χ^2 algorithm is then employed to compare the expected and the real forms. This assigns a number to the pulse, which shows how close to the ideal pulse-shape it is. This number is determined by this equation.

$$\chi^2 = \frac{\sum_{m=1}^{m=C} (x_{n,m}(\frac{\overline{A}}{A}) - \overline{x_m})^2}{\sigma^2}$$

where C is the number of channels per pulse,

σ is standard deviation, and calculated using the finite population data model as

$$\sigma^2 = \frac{N \times \sum x^2 - (\sum x)^2}{N^2}$$

The summations here are performed over a region of the pulse where the form is not evident, ie a region after the actual pulse, and in practice in the last 300 channels. N here is the number of channels used, and would therefore be 300 in this case.

The value of χ^2 is calculated for all the pulses, then a histogram can be shown. From this, it is clear that the χ^2 for most pulses is low, showing that most of the pulses are genuine. The user then determines a threshold level of χ^2. Pulses with a χ^2 above this are subsequently ignored. Having hopefully eliminated most of the bad pulses, the averaging procedure and the χ^2 routine are repeated on the unrejected pulses. This should lead to a more accurate average form being determined, and allows the possibility of further rejection if necessary. At the end of this stage, all pulses which are considered to be unwanted are marked as bad, and all further processing is performed only on unmarked pulses.

3.3 Matched Filtering of Pulses

Once unwanted pulses have been rejected, it is necessary to use a technique to determine the height of each of the pulses. The matched filter technique devised by Holland[1] is easily adaptable to this end, and operates as follows.

This technique assumes that the pulse form is independent of magnitude, which should be the case given that the time constants of the pulse are dependent on the detector construction. The rise time is dependent on the speed of absorption of the X-ray, and the speed of conduction of the energy from the absorber to the semiconductor. The fall time is dependent only on the conductance of the link between the semiconductor and the heat bath.

Initially the pulses are considered to be in digitised arrays $x_{n,m}$, where $x_{n,m}$ is the height of the n_{th} pulse (of which there are N) at a time $m\delta t$ after the start of

the recording. Each pulse consists of P bins, each separated by a time δt. The average pulse form $\overline{x}_m$ is given by

$$\overline{x}_m = \frac{1}{G}\sum x_{n,m}$$

Where the summation is over n as all the unrejected pulses.

This equation determines the shape of the average pulse, based on the shapes of all the individual unrejected pulses.

A weighting array ω_m is then calculated.

$$\omega_m = \frac{\overline{x}_m - \overline{x}}{\mathcal{N}}$$

where

$$\overline{x} = \frac{1}{P}\sum_{m=1}^{P} \overline{x}_m$$

and

$$\mathcal{N} = \sum_{m=1}^{P} | \overline{x}_m - \overline{x} |$$

ω_m is now a measure of how significant the element m in the pulse array is in determining its height. The effect of this is to eliminate the noise regions either side of the actual pulse data, and the enhance the peak of the pulse.

The factor $\mathcal{N}$ is to normalise ω_m

The height of pulse n, ph_n is now calculated as

$$ph_n = \sum_{m=1}^{P} \omega_m (x_{n,m} - \overline{x}_n)$$

where $\overline{x}_n$ is the average height of the n^{th} pulse and can be calculated by

$$\overline{x}_n = \frac{1}{P}\sum_{m=1}^{m=P} x_{n,m}$$

This height is calculated for each pulse, and stored. When all G heights have been calculated, the user determines how many channels the pulse spectrum is to be binned into. The programme determines bin width, and scales the histogram to give a suitable display. Once the histogram is shown, it can be stored as a text file, showing how many pulses fit into each bin. This output file has the terminator **.SPC**, and can be used by the later processing programs.

This programme creates a number of output files, described below.

- filename.**SPC**

  This file contains the histogram produced by the matched filter, mentioned above. All the data in the file is written as an ASCII file for easy integration into any other package. The first line of the file contains the filename of the original dataset used in the processing. The next line contains a brief comment entered by the user at the time of saving the histogram. The third line has a single number on it, which denotes the number of channels the data was binned into. The following lines are the individual bins. Each line contains the number of pulses in one bin.

- filename.**REJ**

  The file contains the pulses rejected in the χ^2 rejection stage of processing. This file has exactly the same form as the original .DAT files, except that there are not usually 600 pulses in this file.

- filename.**WIN**

  When the user is presented with the histogram of pulses, they may identify a region of the histogram of interest, and then store those pulses giving rise to the feature of interest. The programme will then send the relevant pulses to disk in the same format as a .DAT file, to allow for later processing.

- filename.**CHI**

  When the histogram of χ^2 values is presented to the user in the χ^2 rejection stage of processing, the user is given the option to store the histogram on

a file. This ASCII format file consists of a 100 lines, each containing the number of pulses occurring within a certain range of χ^2. This file is useful to determine the spread of χ^2 occurring within a dataset.

3.4 Maximum Entropy Method of Deconvolution

A possible stage of processing is that of the maximum entropy method deconvolution of spectrum (MEM). This method assumes that the obtained spectrum is just the convolution of delta-functions making up the spectrum, and the noise distribution of the system. This noise distribution is obtained by sampling of the signal from the calorimeter previous to the X-ray photon thermalisation pulse. This technique is very sensitive to the noise distribution, and it is therefore essential to sample it carefully.

An apparent resolution improvement of about 45 % is yielded by this method, however the resulting spectral profiles are far from satisfactory. Since the primary object of this project is to design a device of improved resolution, MEM has not been adapted for extensive use, and has not been represented here.

3.5 The Fitting of Data

A number of programmes have been developed in order to process the data produced by the matched filter programme. Whilst simply viewing the matched filter histograms gives an idea of the obtained energy resolution, and it is possible to estimate resolution with a pen and ruler, it is important to obtain figures based on a more repeatable process.

3.5.1 Determining the Point Spread Function, and Internal Noise

Assuming that the noise imposed upon the pulses has a roughly white spectrum, then the delta-functions that the X-ray lines would be in a noiseless system be-

come gaussian in form. Although visual inspection shows that this is approximately the case, it is worth examining the data to show this.

There are two possible means to determine the point spread function (PSF) of the detector. Both of these involve showing how a delta function will spread when the characteristic system noise is added to the input. To synthesise data that will, when processed produce a delta-function, we use an ideal pulse. This is the pulse resultant when a complete file of pulses is averaged.

$$\overline{x}_m = \frac{\sum x_{n,m}}{R}$$

where the summation is over all n, and

- $\overline{x}_m$ is the m_{th} element of the average form $\overline{x}$.
- $x_{n,m}$ is the m_{th} channel in pulse n in the pulse file.
- R is the number of pulses within the file.

Whilst it would be possible to use a rejection system here to remove pulses of unusual shape, the effect on the resultant form is negligible for this purpose.

To this average form is added a noise file. A noise file has the same format as a pulse file, except that each record does not have a pulse in it, just the background noise. Because of the absence of a pulse, the noise associated with the thermalisation will not be present, only system noise. This means that the point spread function determined by this method will not be exact. As each noise sample is added to the mean pulse form, the output is sent to another file. This file can then be treated as a standard pulse file, and processed by the matched filter programme. The matched filter programme will then provide a histogram which shows what would happen if all the X-rays were noiselessly thermalised in the detector. A peak will occur at the equivalent energy in the histogram, the form of which should be the point spread function. Careful choice of the number of bins allocated then allows for a closer examination of the form. Outputting the histogram data into a programme to fit a gaussian to the form shows how

close the point spread function is to a gaussian. Determining the best fit of a gaussian to the form, and plotting one over the other gives a visual idea of how well the form matches a gaussian, and the width of the gaussian. This width can be converted to a full width at half maximum by calibration.

An alternative but equivalent means of determining the PSF is to make a matched filter using pulse data, and then to feed noise data into it for the histogram.

Both of the above methods show the PSF, but more importantly they show the level of baseline noise. This is the internal noise of the system, and shows how good the resolution of the detector would be, if the only noise present were internal, and none resulted from the thermalisation process. Since further developments in the detector and the thermalisation medium are designed to reduce the thermal noise, the baseline noise is a sign of the ultimate resolution we could hope to obtain with the detector.

It should be noted that in these programmes the standard gaussian equation $y = K.e^{-\frac{x^2}{2\sigma^2}}$ is replaced by a gaussian area equation, which proves more accurate when there are only a few points on the gaussian curve.

$$A = 1 - \frac{1}{2}(1 + d_1x + d_2x^2 + d_3x^3 + d_4x^4 + d_5x^5 + d_6x^6)^{-16} + \epsilon(x)$$

where ϵ is the size of error inherent in this approximation, and in this case conforms to $| \epsilon | < 1.5 \times 10^{-}7$ when the following constants are used.

$d_1 = 0.0498673470$, $d_2 = 0.0211410061$, $d_3 = 0.0032776263$, $d_4 = 0.0000380036$, $d_5 = 0.0000953830$, $d_6 = 0.0000053830$.

This function yields the area underneath the gaussian in the region between minus infinity and x. By use of this and the knowledge of the width of a bin, it is possible to determine the height of the element.

3.5.2 Fitting the Data to the Gaussians

The final stage of processing is to relate the resultant histograms to the expected X-ray energy spectra.

3.5.2.1 *Fitting Individual Peaks*

From the results of the point spread function analysis presented in the later results chapter each of the emission lines roughly approximates to a gaussian function. It is therefore a logical step to attempt to fit the individual lines as gaussians, and to use the fit to determine the FWHMs. Thè fitting programme initially makes a fast scan of the **.SPC** file to take intelligent guesses as to the position of the peak , and its FWHM. The two variables are then adjusted by the programme upwards and downwards until no further adjustment will improve the fit. Finer adjustments are made until to improve the fit would require an adjustment below a user-determined threshold.

There are two flaws to this fitting procedure:-

- The point spread function of the detector need not be exactly a gaussian, although the evidence shows that this is broadly the case.
- Fitting lines individually creates a problem when the gaussians of the two lines are broad enough to overlap.

The output of this programme is a graph, showing how well the gaussian fits the data, and a FWHM based on the scaling factor.

3.5.2.2 *Fitting Both Peaks Simultaneously*

To date experimentation has been undertaken with the use of $^{55}_{26}$Fe, which decays into $^{55}_{25}$Mn and emits X-rays with distinctive energy peaks at 5.8989 KeV and 6.4909 KeV. Given these figures, and the fluorescence ratio of between 0.12 and 0.14, as given by [2] pp.744 it is possible to construct a mathematical model of the expected histogram, using gaussians to represent the two peaks. Tbere are now only two variables in the model, the scaling factor to map bins onto energy along the x-axis, and the FWHM of the peaks. We expect the two peaks to have approximately the same FWHM, and the fitting assumes as much. Firstly a scan of the data is used to make informed guesses as to the values of the two variables,

and then an iterative process is used to change the construct to better fit the data. As the construct fits better, so finer changes are made in its parameters. Once more a χ^2 algorithm is used to judge the match between the construct and the data. The output of this programme is a graph showing how well the construct fits, and the determined FWHM.

A further development to this programme is the calculation of some of the previously assumed parameters relating to the two peaks. Some early data seemed to suggest a rather high apparent fluorescence yield of the K_β line, when compared to the K_α line. Although this was mostly within the statistical uncertainty expected when dealing with only a few hundred counts, it seemed consistent. To investigate this more fully it was decided to incorporate a fluorescence yield ratio calculation into the post-processing software. Particularly important to this calculation was the determination of the uncertainty inherent in this ratio. Since both peaks are gaussians, with the same FWHM, the area of the under the peak will be directly proportional to its height. Hence the fluorescence yield is calculated by the ratio of the heights of the two peaks. Each of these heights is a number of pulses, somewhere between 1 and 1200, and we can therefore apply a statistical uncertainty to each height of the square root of the number of pulses.

We define the fluorescence yield ratio (FYR) as

$$R_{fy} = \frac{h_{K_\beta}}{h_{K_\alpha}}$$

where

- R_{fy} is the fluorescence yield ratio
- h_{K_β} is the height of the K_β line in counts.
- h_{K_α} is the height of the K_α line in counts.

If an absolute error in h_{K_β} exists as Δh_{K_β}, then the relative error in h_{K_β} is given by

$$R.E.(h_{K_\beta}) = \frac{\Delta h_{K_\beta}}{h_{K_\beta}}$$

and similarly for $R.E.(h_{K_\alpha})$.

where $R.E.(x)$ is the relative error inherent in quantity x.

Since we are using the square root of the number of counts as the absolute error, then

$$R.E.(h_{K_\beta}) = \frac{\sqrt{(h_{K_\beta})}}{h_{K_\beta}}$$

$$= \frac{1}{\sqrt{(h_{K_\beta})}}$$

and similarly for $R.E.(h_{K_\alpha})$.

Since these two errors (more properly referred to as uncertainties) are independent, they should be added in quadrature to determine the relative error in the quotient.

$$[R.E.(R_{fy})]^2 = [R.E.(h_{K_\alpha})]^2 + [R.E.(h_{K_\beta})]^2$$

$$\rightarrow [R.E.(R_{fy})] = \sqrt{\left(\frac{1}{(h_{K_\alpha})} + \frac{1}{(h_{K_\beta})}\right)}$$

To convert this relative error into the absolute error on the fluorescence yield ratio, ΔR_{fy}, multiply this relative error by the ratio.

$$\Delta R_{fy} = \frac{h_{K_\beta}}{h_{K_\alpha}} \times \sqrt{\left(\frac{1}{(h_{K_\alpha})} + \frac{1}{(h_{K_\beta})}\right)}$$

The programme determining the relative fluorescence yields of the lines must take account of this uncertainty, since as can be seen from the equation, it is large when dealing with small numbers of counts. For example, if the K_α peak

is 200 counts high, and the K_β peak 26 counts high, then the fluorescence yield ratio is 0.13, with an uncertainty of 0.04.

In addition to this the fitting programme allows some variability in the energy of the K_β line in relation to the K_α line. Unfortunately, drawing conclusions from this data is difficult. Any shift in the relative positions of the lines could be attributed to a shift in the absolute positions of either or both of the individual lines.

3.6 Testing the Processing Software

3.6.1 Outline of Procedure

In order to ensure that all of the processing software works as per the algorithms used, it is necessary to run some test data through the entire suite of programmes. To achieve this, a programme was written that creates a file of pulses with well-defined parameters. The programme SIMUL.C firstly examines a file of pulses, and extracts an average pulse form. Since one expects K_α and K_β pulses, it is necessary to generate a number of normal pulses, and a number of pulses greater in height than the average pulses. Since the fluorescence ratio generally accepted[2] is 0.13 ± 0.01, then the programme scales 70 pulses out of the 600 to be the K_β pulses. Since the K_β pulses represent a 6.4909 KeV line, and the K_α pulses represent a 5.8989 KeV line, the K_β pulses were synthesised by multiplying each element of the pulse by 1.100. To each of the 530 K_α pulses and 70 K_β pulses was added a sample from a noise file at the same temperature as the average pulse form was taken from.

Hence the result of the SIMUL programme should be a file containing 530 K_α pulses, and 70 K_β pulses, each with noise, so that when processed, the fluorescence yield ratio should be 0.13, and the energy ratio of the two peaks generated should be 1.100.

The procedure of processing this data with firstly the program CRAMFCOM and

subsequently WIDTH will test both of these effectively.

3.6.2 Implementation

To test the processing programmes, the programme SIMUL was given the file FE1.19.11.DAT to extract the pulse form from, and the noise samples were taken from the file NOISE1.DAT. The output file was called NEW.DAT. The programme CRAMFCOM was then used to process NEW.DAT. No rejection was applied to the data, and the pulses were put through the matched filter and binned into 200 bins, twice as many as usual. 200 bins were used because the noise samples only contain internal system noise, and the peaks are therefore narrower than real peaks, which include noise due to the thermalisation process.

3.6.3 Results

The results of the CRAMFCOM and WIDTH programmes are shown in Figure 3.1, along with the resultant fitting data. The gaussian fit to the two peaks are almost entirely within the uncertainty bars of the data, and the fluorescence yield ratio is exactly as expected, suggesting that the technique used is indeed processing the data as desired, and that the gaussian assumption is valid.

3.7 A Space-based Processing System

To reduce the data transfer from the space platform described in Chapter 7 and the ground station, it would be very convenient if some of the above processing steps could be performed using an on-board computer system.

3.7.1 Outline

The optimum system would be one where the ADC output from the detector was fed into the computer input. The computer would then store n pulses, decide

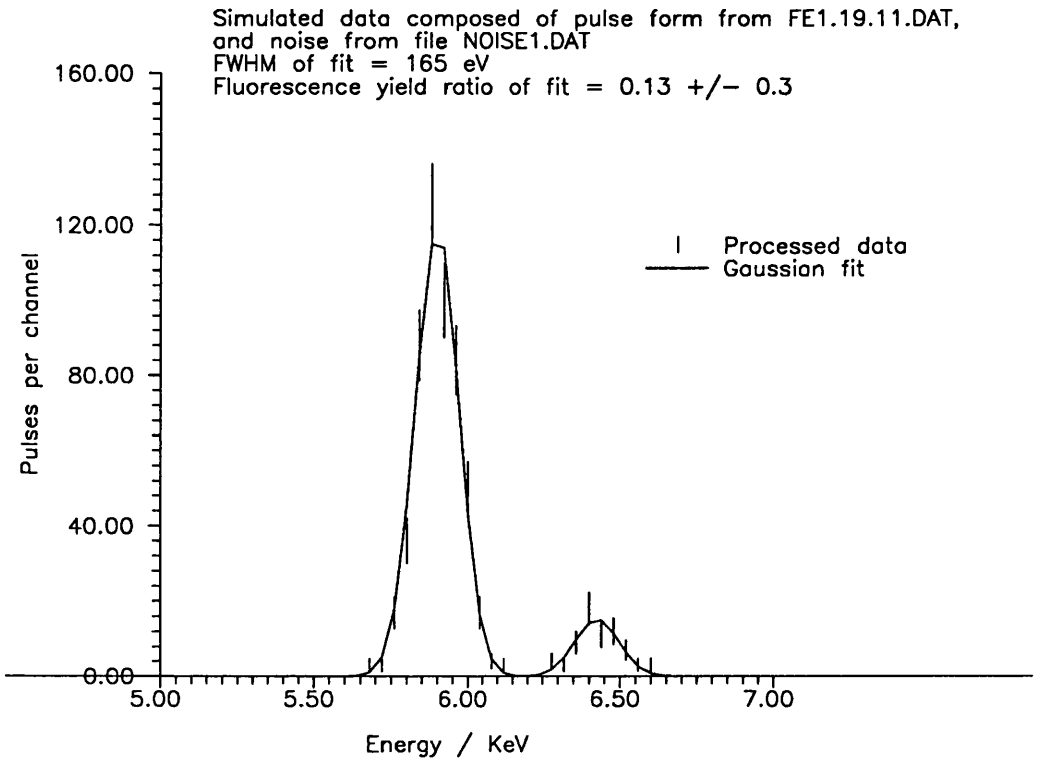

Figure 3.1: *The Processed Simulated Data*

which pulses to reject and discard them. The system would then devise a matched filter by examination of the remaining pulses, and apply this filter to each of the pulses in turn, determining a pulse height for each. These heights would then be binned, and the resultant array be transmitted to the ground station. Hence only approximately 600 integers need be transmitted from an possible 360000 integers input to the computer.

Below I describe three hypothetical systems, and show the memory storage requirements for them.

3.7.2 A System based on the Current Algorithms

Below I describe a processing system substantially based on the one in use in the laboratory.

3.7.2.1 Initial Storage

The ADC provides a height reading to the computer every 10 μs. This height is 8-bit form, and so consists of a 1-byte integer. The computer puts this height into a rotating buffer. If the height exceeds a trigger level, then the following 100 samples and the preceding 28 are stored in memory as a pulse event. Storage area for 1024 pulses, each 128 heights long will be required. This imposes an initial pulse storage requirement of 131072 bytes in the case of an 8-bit ADC.

3.7.2.2 χ^2 Rejection of Pulses

The system will then determine the average form of pulses by adding the n_{th} element from each pulse together, dividing by the total number of pulses, and storing the result in a 128 element array. Each element in this $\overline{x}_m$ array will be 4 bytes long because of the necessity of adding so many pulses together before division, and will hence require 512 bytes of storage.

For each of the stored pulses, the average pulse is scaled up (after the subtraction before scaling, and the addition after scaling, of the baseline) to match areas. For each of the 128 elements the difference between the pulse height and the scaled average pulse height is squared, and added to the total value of χ^2_n for the pulse. Each of the 1024 pulses will then have an associated value of χ^2, and a threshold level is used to reject all those pulses which do not match the average form. Hence the variables χ^2 and a 1-bit determination of whether or not the pulse has been rejected are further storage requirements. χ^2 should be a 1024 element long array of 2-byte integers, and therefore take up 2048 bytes, and the good/bad flag should take up 1024 bits, or 128 bytes.

3.7.2.3 Matched Filter

At this point the matched filter technique described in Section 3.3 is used.

The memory requirement of each of these calculation stages is listed below...

$\overline{x}_m$ can use the same memory as the χ^2 stage uses.

$\overline{x}_n$ is the average height of pulse n, and since the processing only requires the average height of the current pulse, only a 4-byte integer need be allocated.

$\overline{x}$ will only be a 4 byte integer.

The weighting array ω_m should be a 128 element array of 4-byte floating point numbers, 2 bytes either side of the decimal point, hence 512 bytes are required.

The pulse height for each of the pulses ph_n will be a 1024 element array of 4-byte floating point numbers as ω_m, and will thus take 4096 bytes.

In order to determine how to bin the pulses, it would be useful to have an average pulse height $\overline{ph}$, which would be calculated simply by substituting the average pulse form into the pulse height determination equation thusly.

$$\overline{ph} = \sum_{m=1}^{P} \omega_m(\overline{x}_m - \overline{x}_n)$$

The storage for this variable would require a 2-byte integer, hence 2 bytes of storage space.

To determine what pulse height should go into what bin at the final stage, it is useful to have a bin scale.

$$BINSCALE = \frac{300}{\overline{ph}}$$

If we then multiply this scale factor by the pulse height yielded by a pulse, then the average pulse will occur around bin 300. This variable should be a 4-byte float.

When the pulse heights are being binned for transmission, the bin width should be approximately the expected resolution of the detector or narrower. Hence for a

10 eV resolution detector observing X-rays with an energy approximately 6 KeV, 600 bins are required. Each of these bins will be an element in the pulse height array. If only 1024 pulses are recorded, then each element need only be a 2-byte integer, and the total array memory allocation will be 2048 bytes.

3.7.2.4 Conclusion

Adding together the above estimates for the memory requirement of this system yields a total of 140430 bytes. This is not unfeasible, but a little high. Furthermore, this system of processing, based as it is on the system we use in the laboratory-based experiments has other flaws. Firstly there is a distinct limit on the number of pulses observable in one session set by the memory allocation. Secondly, if it is desired to observe more than 1024 pulses in one observing run, then a delay between the two sessions will occur whilst the first data set is being processed. This down-time is potential observing time, and is especially valuable if a refrigeration system such as an ADR is being used to cool the detector.

Hence it is necessary to consider an alternative system which is not limited in its pulse-count in one session, but is based on the same processing methodology.

3.7.3 A Space-based Processing System

3.7.3.1 Description

In this system, we do not store 1024 pulses, and then process them. To determine the average pulse form $\overline{x}_m$ we initially input 128 pulses, and calculate it from those pulses. Thusly χ^2 is determined as each pulse is recorded, and its rejection or otherwise is determined immediately. The storage of $\overline{x}_m$ will consume only 256 bytes, since we will only be summing 128 1-byte numbers, hence only a 128 element array of 2-byte integers are required. The storage of 128 pulses, each 128 bytes long will consume 16384 bytes

In the stage of processing the 128 sample pulses we can also calculate $\overline{x}$, $\mathcal{N}$ and the weighting array ω_m. $\overline{x}_m$ will be the same $\overline{x}_m$ used in the χ^2 stage, $\overline{x}_n$ will use

4 bytes as a 4-byte integer, $\overline{x}$ will use 4 bytes, $\mathcal{N}$ is only a 4-byte integer, and the weighting array ω_m will be, as before, a 128 element array of 4-byte floats, and will use 512 bytes. The average pulse height $\overline{ph}$ will require 2 bytes as a 2-byte integer. The bin scale will require an additional 4 bytes as a 4-byte float.

During the process of receiving the pulses, a 128 byte array will be required to store the pulse data as it is being received, and for processing.

If the pulse height array uses 600 2-byte integers as before, which allows a maximum bin height of 65536, then assuming a count rate of 100 s^{-1} this allows an observing time of 11 minutes maximum, assuming the worst case that all pulses end up in the same bin. Extending this integer length to 4 bytes makes the maximum bin height 2^{32}, and the observing time maximum over 11000 hours, and is probably a more sensible figure. Hence the pulse-height array will be a 600 element array of 4-byte integers, and will use 2400 bytes.

3.7.3.2 Total Memory Requirement

Hence, the total memory allocation using this scheme is 16384 bytes for the storage of the 128 pulses, and an additional 3314 for the other processing requirements. Once the variables relating to the 128 pulses have been calculated, however, we may then discard the initial 128 pulses, and store the pulse height data in that freed space, hence the total requirement is only 17298 bytes.

3.7.3.3 A Further Refinement

The requirement for the 16384 bytes for the initial 128 pulses may also be removed. If, when each of the initial pulses is recorded, the value of each element is added to a cumulative array, each element of which represents one element on the average pulse, then, once 128 pulses have been read, then the average pulse form $\overline{x}_m$ can easily be determined. From this, $\overline{x}$ can also be calculated, and thence $\mathcal{N}$ and the array ω_m. Once the 128 pulses have been used to calculate $\overline{x}_m$, $\overline{x}$, $\mathcal{N}$ and ω_m, $\overline{ph}$, and the bin scale, each pulse received can be used to build up the energy spectrum.

Hence the requirement for this system is just the 256 bytes for the cumulative calculation of $\overline{x}_m$ by a 128 element array of 2-byte integers, 4 bytes for the 4-byte integer $\overline{x}$, 4 bytes for $\mathcal{N}$, 512 bytes for the ω_m 128 element array of 4-byte floats, 2 bytes for the 2-byte integer $\overline{ph}$, 4 bytes for the 4-byte float bin scale, and the 2400 bytes required to store the pulse height histogram. This yields a total requirement of 3182 bytes, and since it is now evident that the stored results dominate the memory storage requirement, this is a satisfactory situation.

3.7.3.4 Speed of Processing

Figure 3.2 shows the flow diagram the microcalorimeter processing system will have to follow.

It is clear that in determining the processing system to use, speed of processing will be a paramount consideration, not only because of the small time an event takes, but also because if the detection procedure is held up by the processing, then the ADR is cooling the detector whilst it is useless. An ideal system would be that in which, while the processing is being performed on a pulse, a separate subsystem, is monitoring the detector, and will capture any events independently, ready for processing when the height of the current pulse has been determined and binned. To this end, the requirement is that only one pulse event should occur in the time it takes to process a pulse, the time the processing system is passing around the second loop in Figure 3.2. As estimated earlier, a sensible event rate for this detector would be $100\,\mathrm{s}^{-1}$, yielding a processing time of 10 ms.

As can be seen from the diagram, in this 10 ms the majority of the processing is simply the optional calculation of χ^2 and decision as to the quality of the pulse, subtracting a 4-byte integer from each of the 128 1-byte integer elements in the current pulse, and multiplying each result by an element of a 4-byte float array. The sum of these products is then multiplied by the 2-byte scaling factor $BINSCALE$, and the appropriate array element incremented. This is not very demanding on a modern microprocessor, and will easily be achieved within the required time.

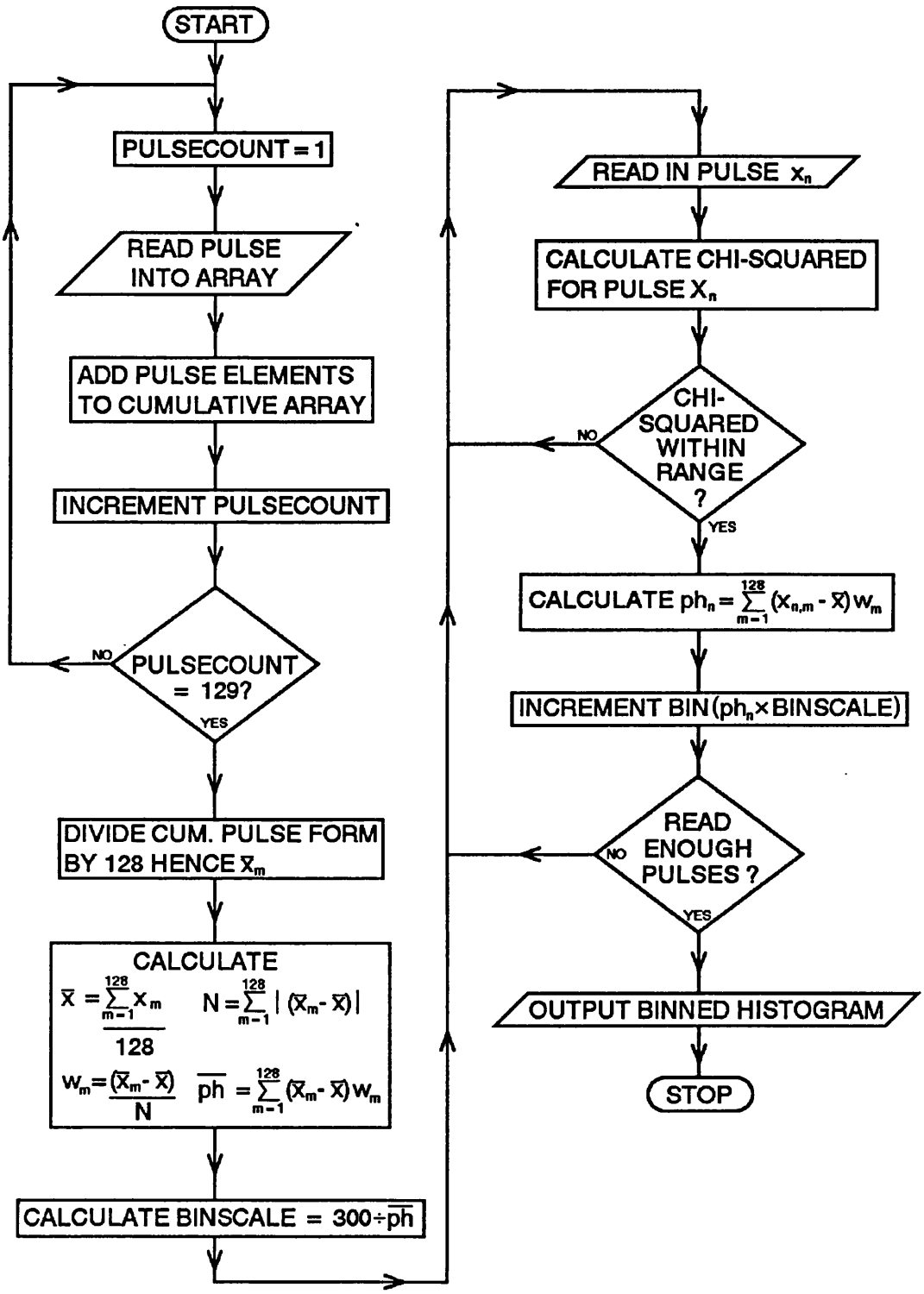

Figure 3.2: *Processing Flow Chart*

Bibliography

[1] *PhD Thesis* - W.S. Holland, Queen Mary and Westfield College, The University of London

[2] *Compilation of X-ray Cross-sections* - W.H. MacMaster, N. Kerr Del Grande, J.H. Mallett, J.H Hubbell - National Bureau of Standards - Lawrence Radiation Laboratory.

[3] *Atomic Fluorescence Yields Proc* - R.W. Fink, R.C. Jopson, Hans Mark, C.D. Swift, Rev. Mod. Phys. Vol.38 No.3 pp. 513-536, July 1966

[4] *X-ray Fluorescence Yields, Auger and Coster-Koenig Transition Probabilities* - Walter Bambynek, Bernd Crasemann, R.W. Fink, H.U. Freund, Hans Mark, C.D. Swift, R.E. Price, P. Venugopala Rao, Rev. Mod. Phys. Vol.44 No.4 pp.716-813, October 1972

[5] *Development of X-ray Calorimetric Detectors and Data Processing Techniques at London University* - I.D. Hepburn, P.A.R. Ade, M.J. Griffin, W.S. Holland at Queen Mary College, and J.L. Culhane, R. Kessel, D.M. Walton at Mullard Space Science Laboratory, University College London, in the book *Low Temperature Detectors for Neutrinos and Dark Matter-II* published by *Frontieres*, 1988. Edited by L. Gonzalez-Mestres and D. Perret-Gallix.

Chapter 4

November 1991 Data and Interpretation

4.1 Source of Data

During 19th-20th November 1991, an X-ray run was performed at Queen Mary College with the first-commissioned ADR.

4.1.1 System Description

The system under test was the original ADR, with the detector described in Chapter 2 mounted on the detector stage. This detector was optimised for use at 300 mK, and so was not expected to provide ideal results, but this run was intended as an initial test of the ADR and the data-taking equipment. Previous detector work had been performed at 300 mK.

The $^{55}_{26}$Fe source used produces two major X-ray emission lines. The $^{55}_{26}$Fe decays into $^{55}_{25}$Mn, and in this state the $^{55}_{25}$Mn emits a K_α line at 5.8989 KeV, and a K_β line at 6.4909 KeV. In [1], the fluorescence yield ratio (FYR) between the two

lines was determined as 0.13 to within an accuracy of 0.01, where the K_β is the less abundant. In the reference, the theoretically calculated value proposed by Scofield is closer to 0.12, whereas two sets of experiments give values nearer to 0.13 and 0.14.

4.1.2 Schedule of Run

On the 19th November 1991, the ADR was brought down to 100 mK. Data recording was performed using the 12-bit ADC. Four data files were taken with the detector not exposed to a source, these were named NOISE1, NOISE2, NOISE3 and NOISE4. Subsequently an $^{55}_{26}$Fe source was connected to the detector in the source mount, and three data files were taken, named FE1.19.11, FE2.19.11, and FE3.19.11. An explanation of the naming convention is given in Chapter 3.

On the 20th November 1991, a further three data files were taken at 100 mK, named FE1.20.11, FE2.20.11 and FE3.20.11. The data recording system was at this point changed over, and pulses were now recorded by the Digital Storage Oscilloscope, and fed to the computer through the IEEE port. This was the original method, and only digitises to 8-bit accuracy. The two files FE4.20.11 and FE5.20.11 were taken using this configuration.

The temperature of the detector was allowed to rise to 200 mK, and was stabilised. The 12-bit ADC data recording system was restored, and three noise files taken NOISE5, NOISE7, NOISE8. Subsequently six files were taken with the $^{55}_{26}$Fe source in place, FE6.20.11, FE7.20.11, FE8.20.11, FE10.20.11, FE11.20.11 and FE12.20.11.

4.1.3 Table of Information on Source Data

In Figure 4.1, the basic information on the data taken in this run is shown.

Source Data				
Pulses				
File	Temp. (mK)	Number of records	Date recorded	Bits used
FE1.19.11.DAT	100	600	19th Nov 1991	12
FE2.19.11.DAT	100	600	19th Nov 1991	12
FE3.19.11.DAT	100	600	19th Nov 1991	12
FE1.20.11.DAT	100	600	20th Nov 1991	12
FE2.20.11.DAT	100	284	20th Nov 1991	12
FE3.20.11.DAT	100	541	20th Nov 1991	12
FE4.20.11.DAT	100	750	20th Nov 1991	8
FE5.20.11.DAT	100	913	20th Nov 1991	8
FE6.20.11.DAT	200	600	20th Nov 1991	12
FE7.20.11.DAT	200	600	20th Nov 1991	12
FE8.20.11.DAT	200	600	20th Nov 1991	12
FE10.20.11.DAT	200	600	20th Nov 1991	12
FE11.20.11.DAT	200	600	20th Nov 1991	12
FE12.20.11.DAT	200	600	20th Nov 1991	12
Noise				
Noise1	100	600	19th Nov 1991	12
Noise2	100	600	19th Nov 1991	12
Noise3	100	600	19th Nov 1991	12
Noise4	100	600	19th Nov 1991	12
Noise5	200	600	20th Nov 1991	12
Noise7	200	600	20th Nov 1991	12
Noise8	200	600	20th Nov 1991	12

Table 4.1: *Source Data*

4.2 Forms of Processing applied to data

The data was originally taken on an Archimedes microcomputer, transferred to a VAX computer, stored on magnetic tape, and then transferred to an IBM compatible computer. This computer was used to devise, program, compile and use the processing packages described in the previous chapter on data processing.

Firstly, the data was scanned briefly by the DISPLAY program, to determine that no corruption had occurred.

4.2.1 χ^2 rejection

Each of the .DAT files were analysed twice using the CRAMF program. In one of the analyses no rejection was used, so that all pulses were passed onto the next stage, and in the second case χ^2 rejection was used to remove non-conforming pulses. These rejected pulses were stored.

The rejection used is referred to as "90 rejection". This is because when the user is asked to select a threshold of χ^2 to select, above which pulses will be rejected, they are shown a histogram, giving the χ^2 distribution. This distribution is calibrated in such a manner that the majority of pulses occur in the first 50 bins. "90 rejection", therefore eliminates only those pulses after bin 90, which will be highly non-conforming.

4.2.2 Binning technique in Matched Filtering

The pulses are then binned. In the cases where no pulses are rejected this is merely a case of operating the matched filter on all of the pulses and making a histogram of the determined heights. In order to ensure the binning has a minimal effect between datasets, the binning is calibrated such that the main K_α peak occurs around bin 75 of 100. In this case, each bin has a width of approximately 80 eV.

Where pulses have been rejected, the non-rejected pulses are put through a matched filter generated from the non-rejected pulses. Then the rejected pulses are also put through the same filter, to determine what height they would have been if they had not been rejected. Thus the output from this stage is a "good" histogram of non-rejected pulses, and a "bad" histogram of pulses which have been rejected.

4.2.3 Fitting parameters applied

Initially, values are estimated for the four variable quantities that the fitting program alters to try to fit the data.

The first variable is the position of the K_α peak. It estimates this by assuming that the highest count in the histogram will occur at the K_α peak. This is correct to within a few bins in all of the datasets yet processed.

The second variable is the width of the peaks, in terms of the σ in this gaussian equation...

$$y = A.e^{-\left(\frac{x^2}{2\sigma^2}\right)}$$

The program determines its first estimate of this by scanning the FWHM of the K_α peak, and using half of the FWHM.

The third variable, the fluorescence yield ratio between the two peaks is estimated as being 0.13, as suggested by the references above.

The last variable is the ratio between the positions of the two peaks. This is estimated as being what we would expect, the ratio between the energies 6.4909 KeV and 5.8989 KeV, 1.100.

4.3 χ^2 Rejection and Matched Filter on all files

The following pages show the data obtained in November 1991, showing the matched filter spectra obtained before and after χ^2 rejection, and in the cases

where χ^2 rejection has been used to discard pulses, the discarded pulses are also shown as broken lines.

4.3.1 Processing of Individual Data files

In the following pages, one side is devoted to two histograms of each dataset. The upper histogram is the pre-rejection data, where all pulses are processed. The points on the histogram are represented by vertical lines. The length of the lines indicates the uncertainty of the point. Since each point represents a number of pulses, the uncertainty is represented as being the square root of this number. The continuous line through the data points is the fit to the data points generated by the fitting program. The information presented above each graph on FWHM, χ^2 and fluorescence yield relate to this fit. In the case of the χ^2 value, this is the sum of the calculated χ^2 for each bin divided by the number of bins used in the processing. Because the data points are all related to the surrounding points this number is not directly related to the quality of the fit in a proportional manner, however, the lower the value of χ^2, the better the fit is, and our concern here is to compare the quality of the fit between the datasets.

The lower histogram is laid out as the upper histogram, except that the data in this case has been through the χ^2 rejection filter, and this has removed a number of pulses before the matched filter has been calculated and applied. The number of pulses rejected is shown in the information above the graph, and where those pulses would have occurred in the histogram is shown as a dashed line.

Following each pair of histograms are comments on any of their interesting features.

After the individual datasets, the data from several sets is added together to reduce statistical error. In the first case all of the data files recorded at 100 mK except for one are treated as one data file, and the results presented. The data file omitted is FE3.19.11.DAT, and is omitted because the individual file-processing indicates that the FWHM obtained from the pulses in this file is substantially

larger than that of the other 100 mK files. This is probably due to a drift in temperature over the time of the run.

A composite dataset is also composed from the 200 mK data in the files FE6.20.11, FE7.20.11, FE8.20.11, FE10.20.11, and FE11.20.11. The file FE12.20.11 is omitted, since it is clear from processing this file on its own that a considerable temperature drift during the data-taking has caused a broadening of the peaks.

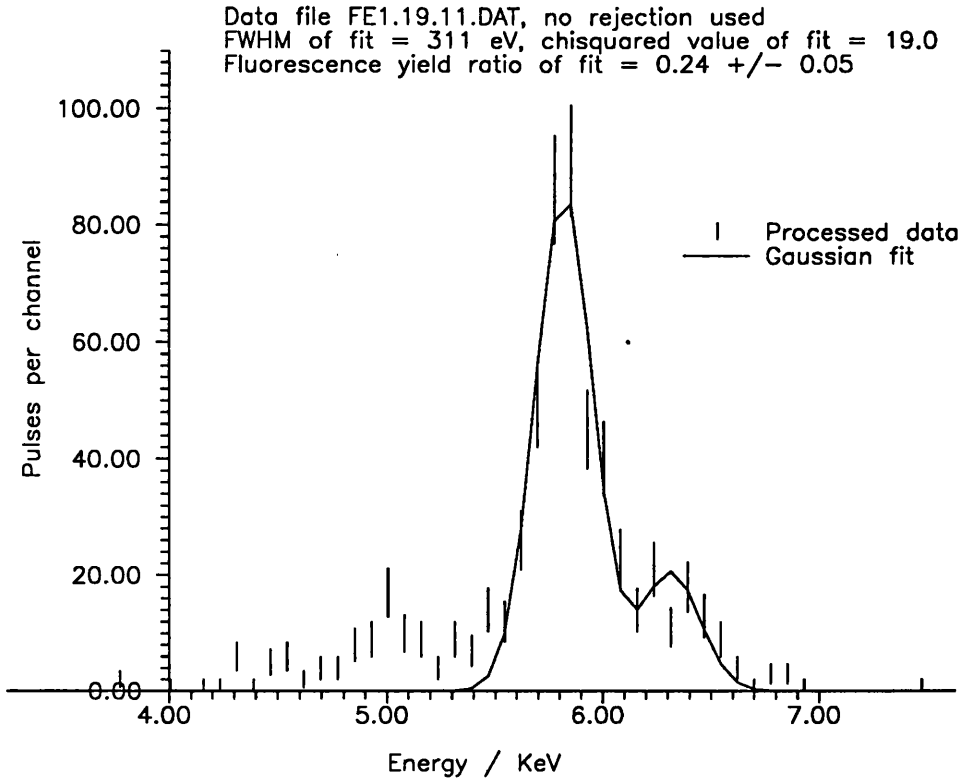

Figure 4.1: ***FE1.19.11.DAT, no rejection***

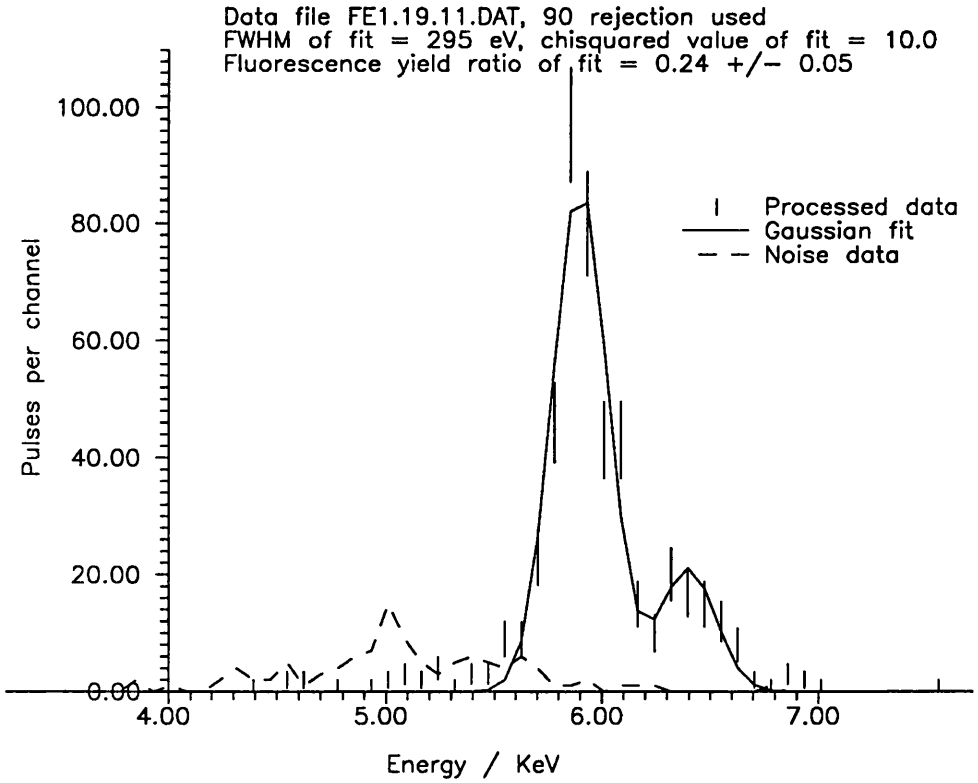

Figure 4.2: ***FE1.19.11.DAT, 90 rejection***

FE1.19.11.DAT Processed Data - Comments

This data was taken at 100 mK, with the detector observing the $^{55}_{26}$Fe source, on 19th November 1991. 600 pulses were recorded.

The χ^2 rejection algorithm here seems to have been most effective. The region of noise, between 4 KeV and 6 KeV has been substantially reduced, and this has resulted in an improvement in the gaussian fit, which has reduced χ^2 here from 19.0 to 10.0.

The fit has two interesting features. Firstly, it does not encompass the highest data point on the post-rejection data fit, and only just falls within the statistical error on the highest two points on the non-rejected data. This is possibly explained by the other point of interest, which is the odd pair of data points on the high energy side of the main peak. This feature may represent a shoulder caused by the fact that the K_α line is really composed of the K_{α_1} and the K_{α_2} lines.

Unfortunately, the low number of pulses around the K_β peak, and the poor fitting of the top of the K_α peak make the calculated fluorescence yield ratio between the two peaks higher than one might expect, in that the K_β peak seems to be too high. The odd structure of the K_β peak in the unrejected data shows that this result is to be treated with some caution, although the form is improved in the post-rejection data.

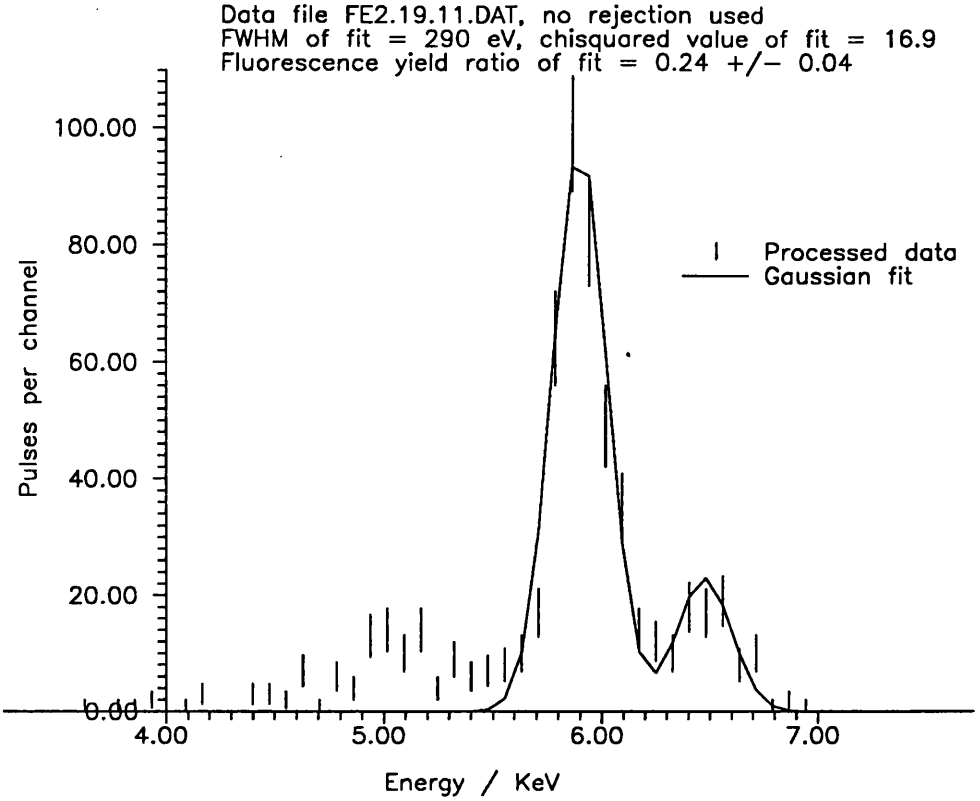

Figure 4.3: *FE1.19.11.DAT, no rejection*

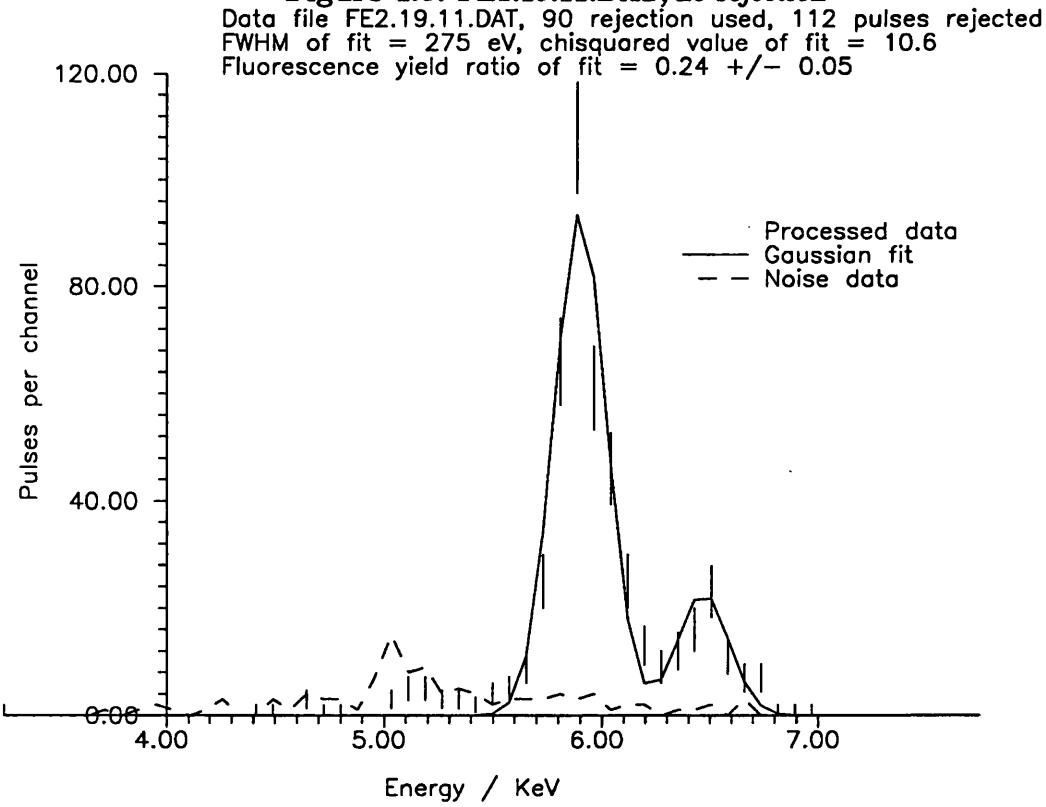

Figure 4.4: *FE1.19.11.DAT, 90 rejection*

FE2.19.11.DAT Processed Data - Comments

This data was taken at 100 mK, with the detector observing the $^{55}_{26}$Fe source, on 19th November 1991. 600 pulses were recorded.

As with the previous dataset, a large amount of the 4 KeV to 6 KeV noise here has been rejected by the χ^2 process, resulting in the improvement in the gaussian fit seen. In this case, again the highest datapoint in the rejected dataset has been missed by the fitting procedure, and this would appear to be because of the odd shape of the main peak. The high-energy shoulder would appear to have disturbed the fit again. The low fit to the main peak has increased the calculated fluorescence yield ratio; if the fit passed through the upper data point then the ratio would be around 0.4 less, however this would still be higher than expected

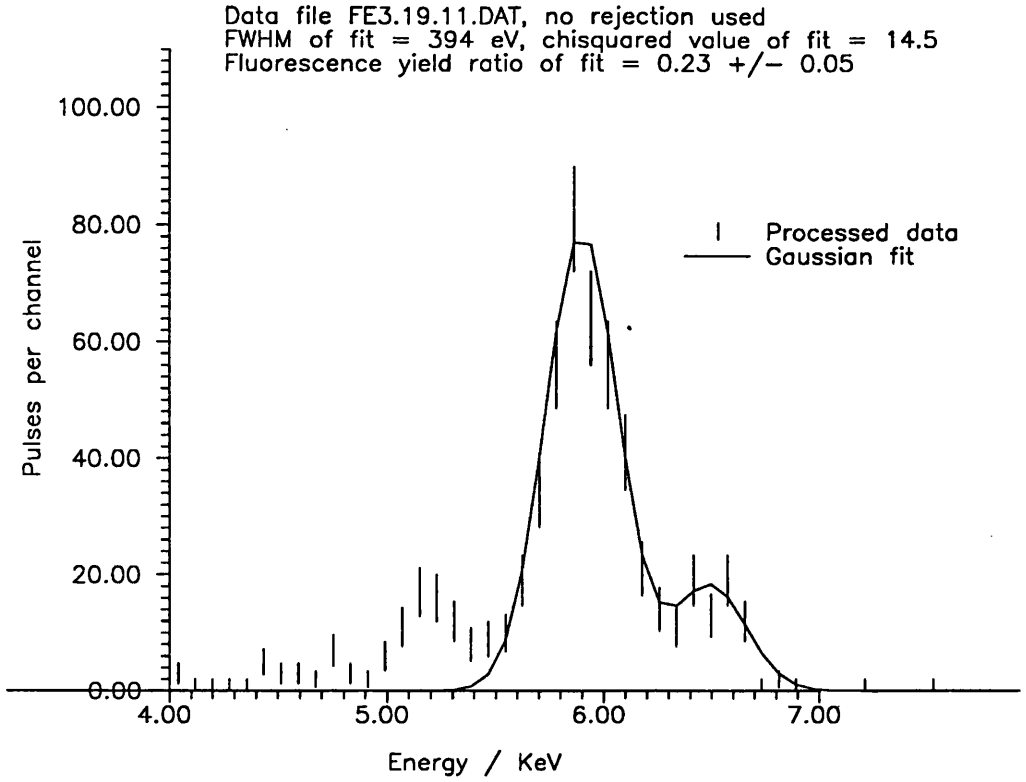

Figure 4.5: *FE3.19.11.DAT, no rejection*

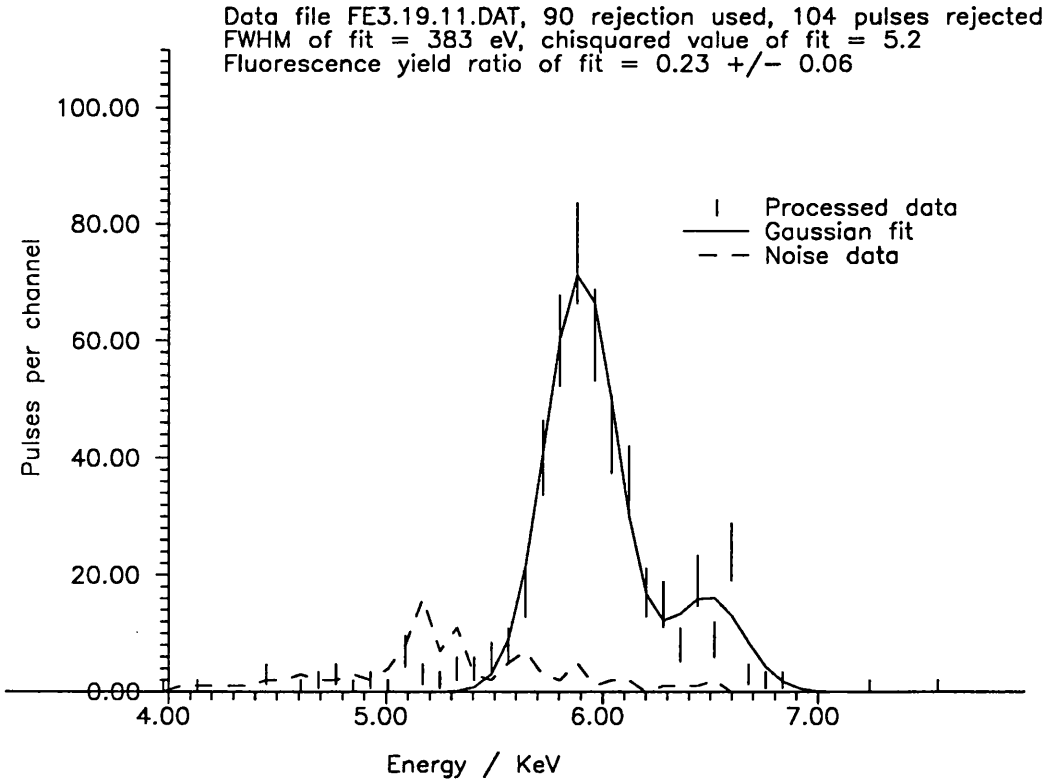

Figure 4.6: *FE3.19.11.DAT, 90 rejection*

FE3.19.11.DAT Processed Data - Comments

This data was taken at 100 mK, with the detector observing the $^{55}_{26}$Fe source, on 19th November 1991. 600 pulses were recorded.

As in the previous data, the χ^2 rejection has substantially reduced the 4 KeV to 6 KeV noise, and has improved the gaussian fit, by nearly a factor of three in this case.

Here again, the height of the K_β peak seems too high, but the structure is still rather formless, and so suspect.

The FWHM calculated here is substantially greater than that for the other 100 mK files, and this suggests that a temperature drift may have occurred during this run, the last of the day.

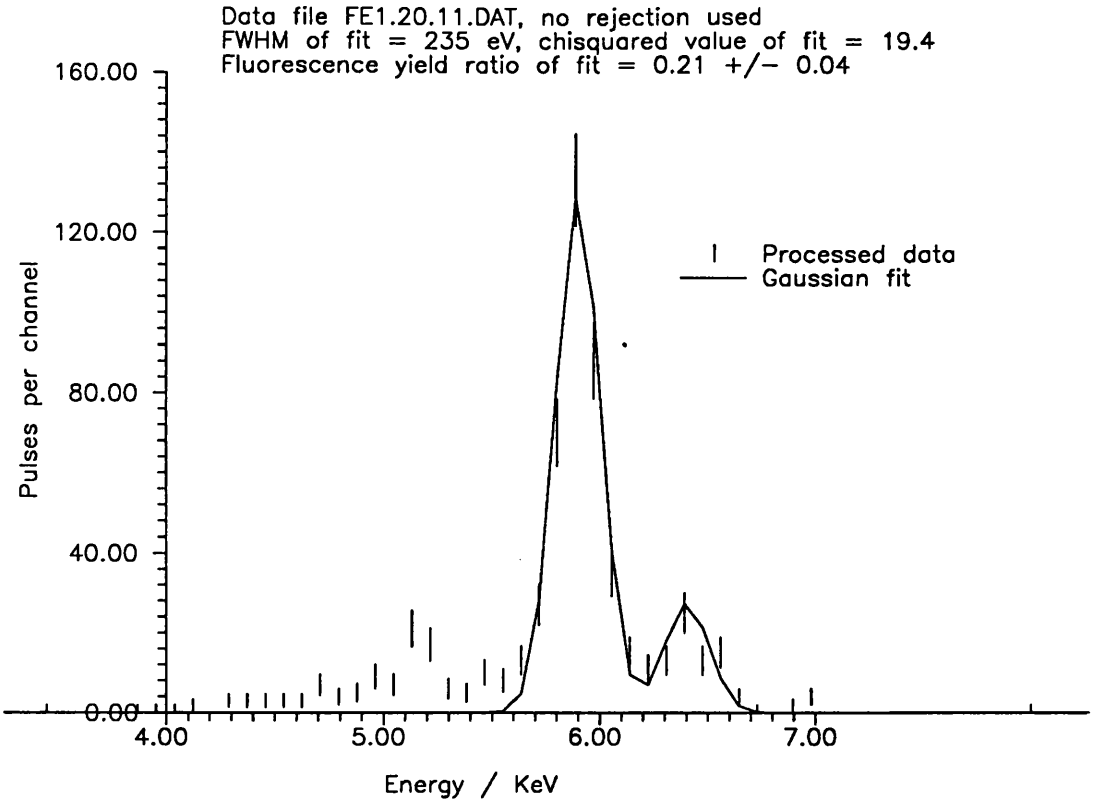

Figure 4.7: *FE1.20.11.DAT, no rejection*

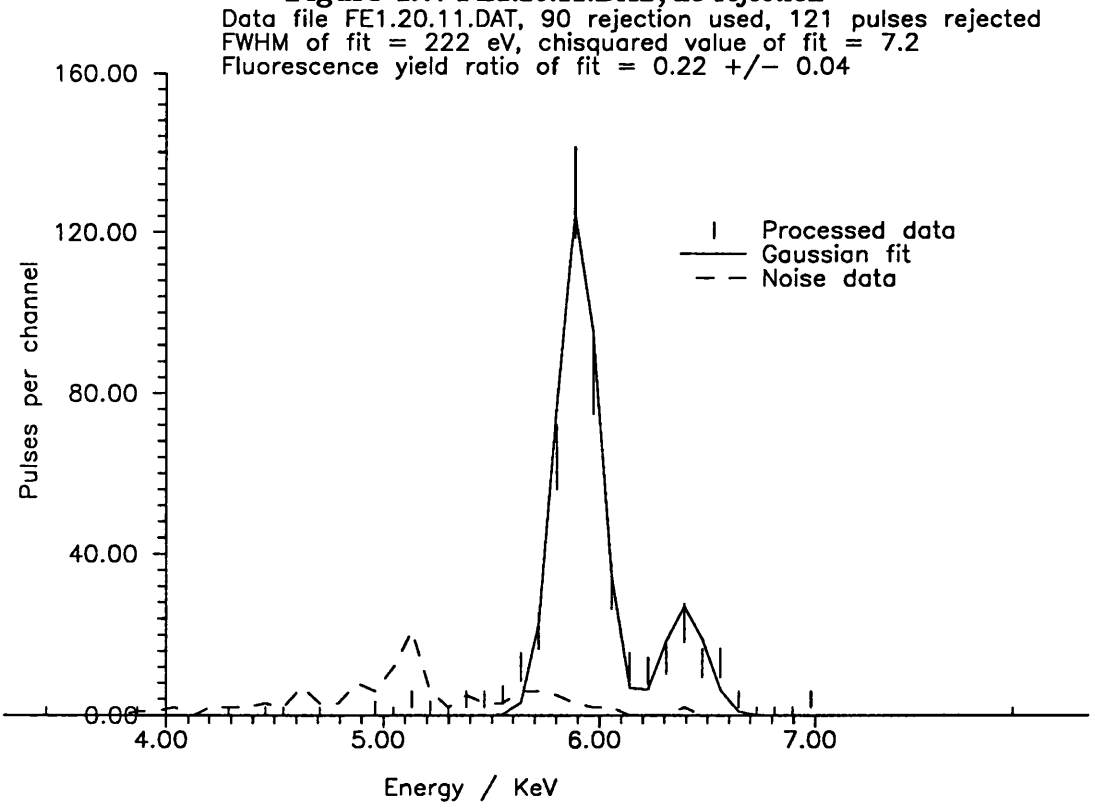

Figure 4.8: *FE1.20.11.DAT, 90 Rejection*

FE1.20.11.DAT Processed Data - Comments

This data was taken at 100 mK, with the detector observing the $^{55}_{26}$Fe source, on 20th November 1991. 600 pulses were recorded.

The 4 KeV to 6 KeV noise has been reduced again here, resulting in an improvement in the quality of the fit, which in this case is very close to most of the important data points.

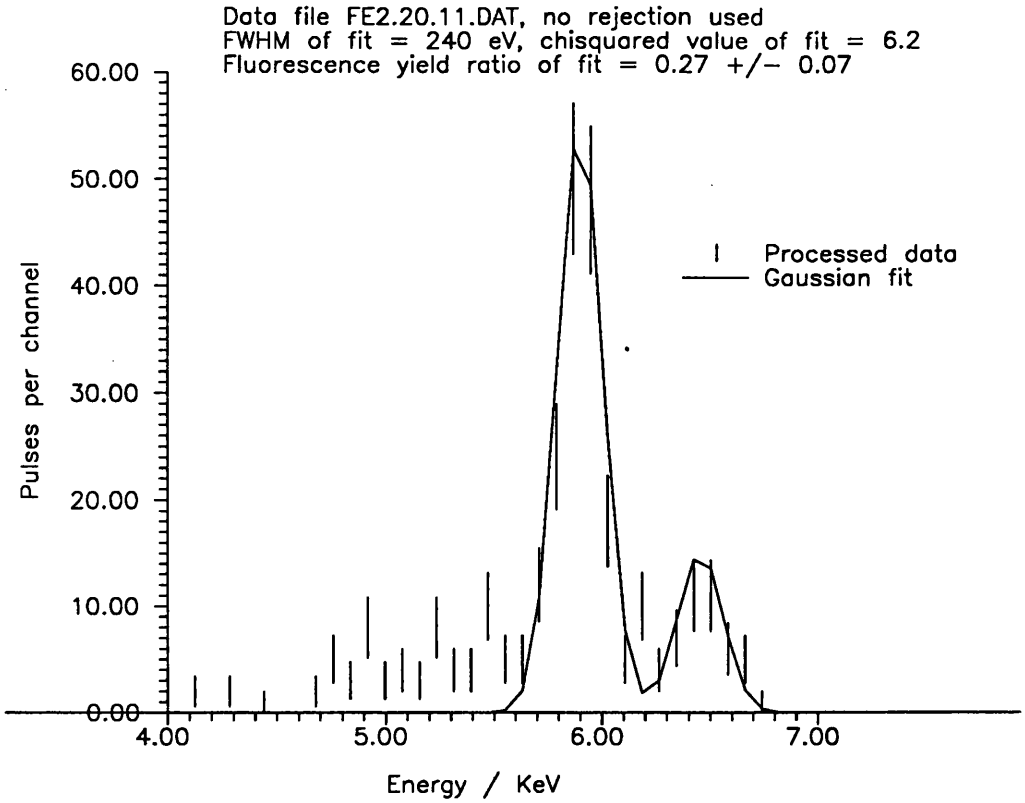

Figure 4.9: *FE2.20.11.DAT, no rejection*

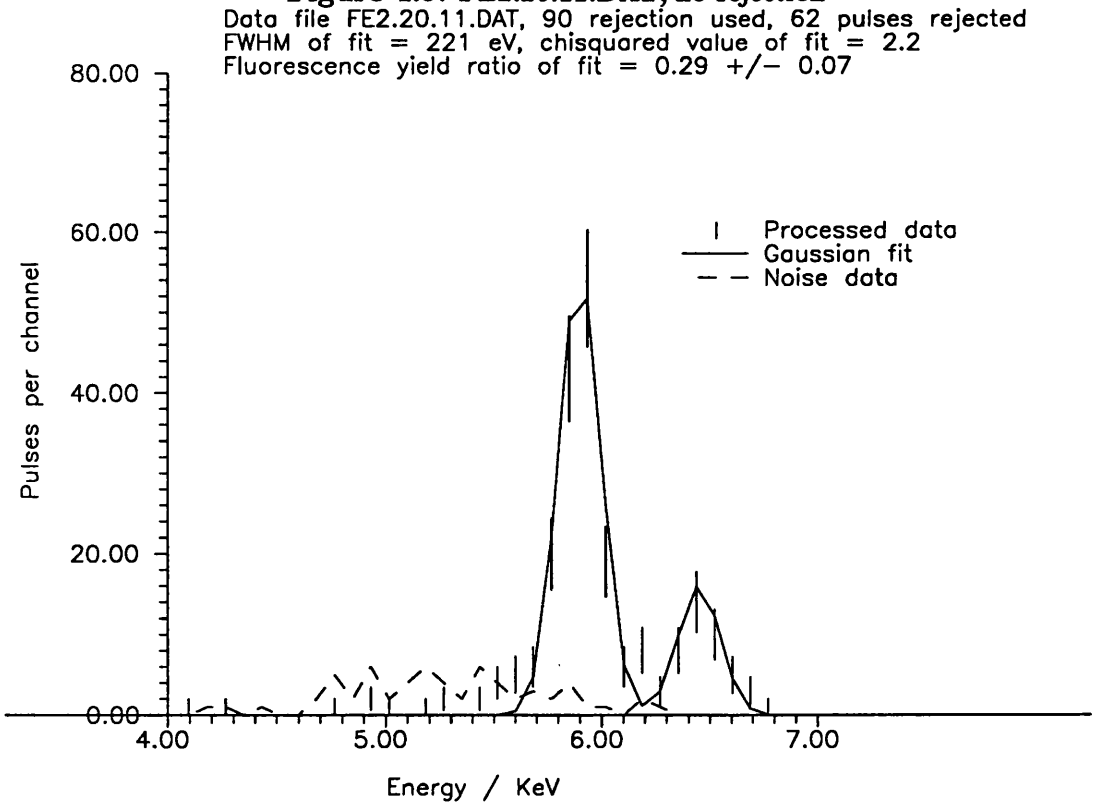

Figure 4.10: *FE2.20.11.DAT, 90 Rejection*

FE2.20.11.DAT Processed Data - Comments

This data was taken at 100 mK, with the detector observing the $^{55}_{26}$Fe source, on 20th November 1991. 284 pulses were recorded.

The small number of pulses in this dataset lead to the large error bars in the shown data.

Although the 4 KeV to 6 KeV noise is still present in this dataset, the double-peak form is better defined, as shown by the dramatically reduced χ^2 values for the spectrum fits, both pre- and post-rejection. Such a good fit makes the height of the K_β peak seem suspicious, since it seems from this that it is over twice the expected level. Whilst the K_β fit on the pre-rejection data seems a little suspicious, the post-rejection fit is good on the majority of points, and leaves little doubt as the to the unexpected high value of the FYR.

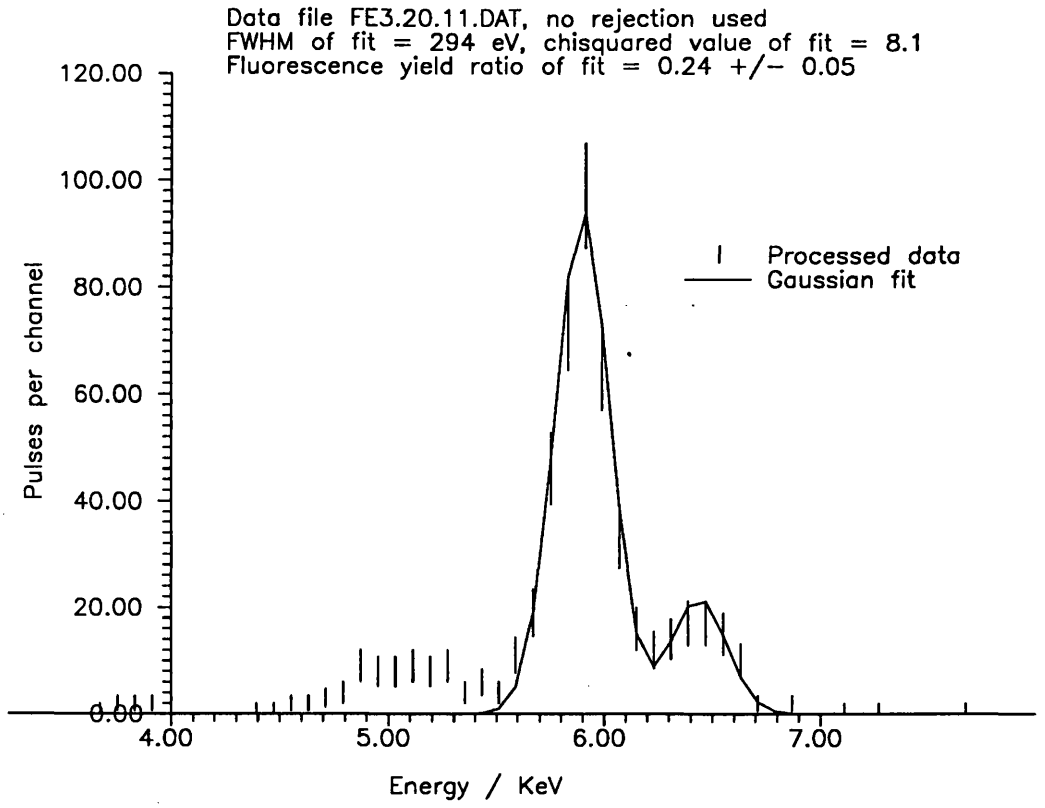

Figure 4.11: *FE3.20.11.DAT, no rejection*

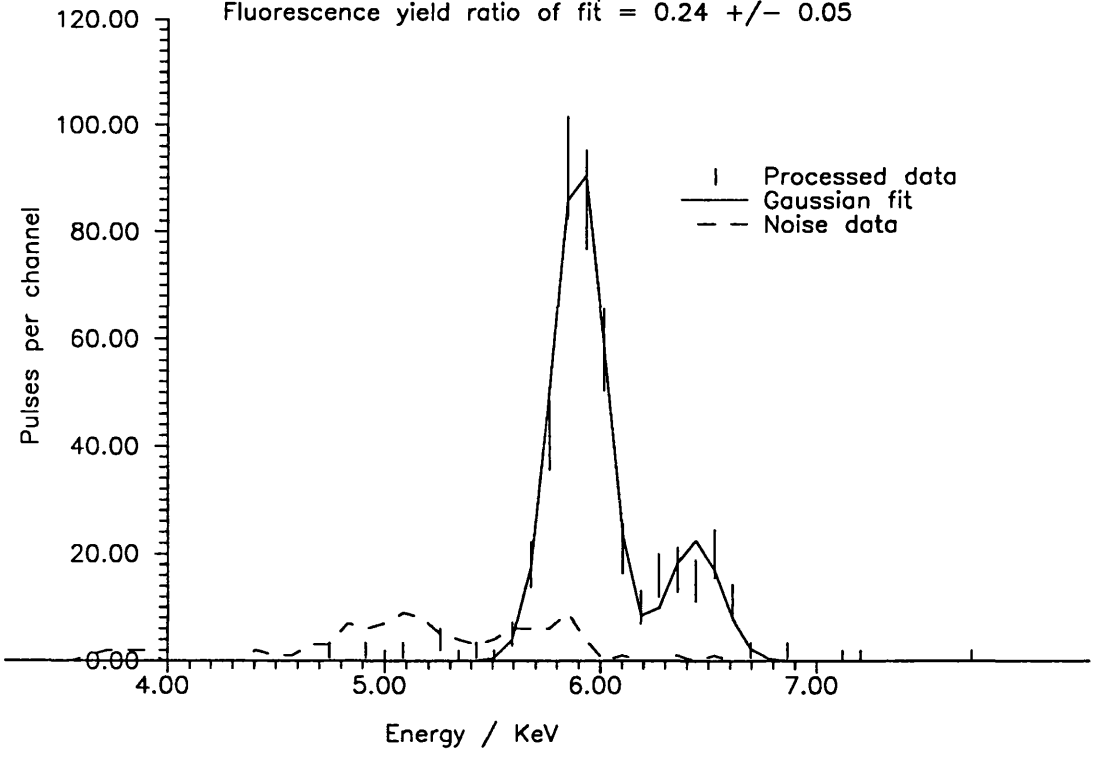

Figure 4.12: *FE3.20.11.DAT, 90 Rejection*

FE3.20.11.DAT Processed Data - Comments

This data was taken at 100 mK, with the detector observing the $^{55}_{26}$Fe source, on 20th November 1991. 541 pulses were recorded.

The 4 KeV to 6 KeV noise has been removed here. Whilst a cursory look at the K_β peak seems to suggest that a better fit would have been made if it were lower and wider, the width of the two peaks should be the same, and allowing the K_β peak to have a greater width than the K_α would suggest that different noise factors contribute to each peak. Clearly the shape is not close enough to a gaussian to be adequately fitted, and indeed when the non-conforming pulses are rejected, the K_β form is lost.

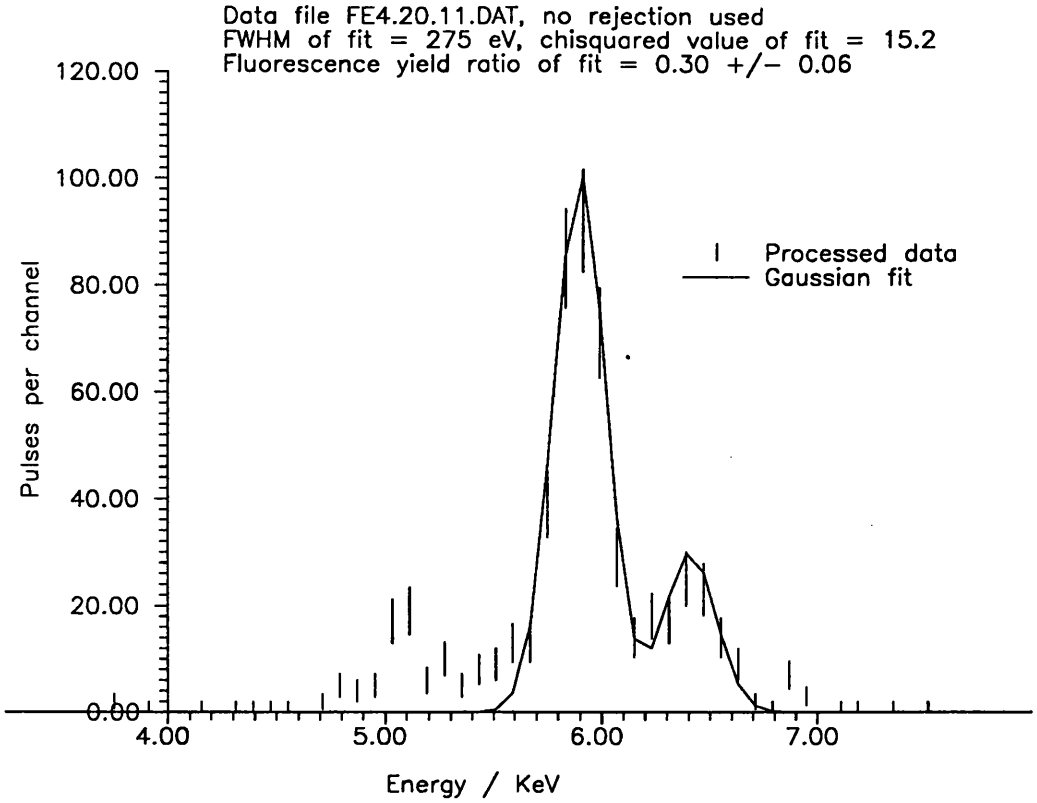

Figure 4.13: *FE4.20.11.DAT, no rejection*

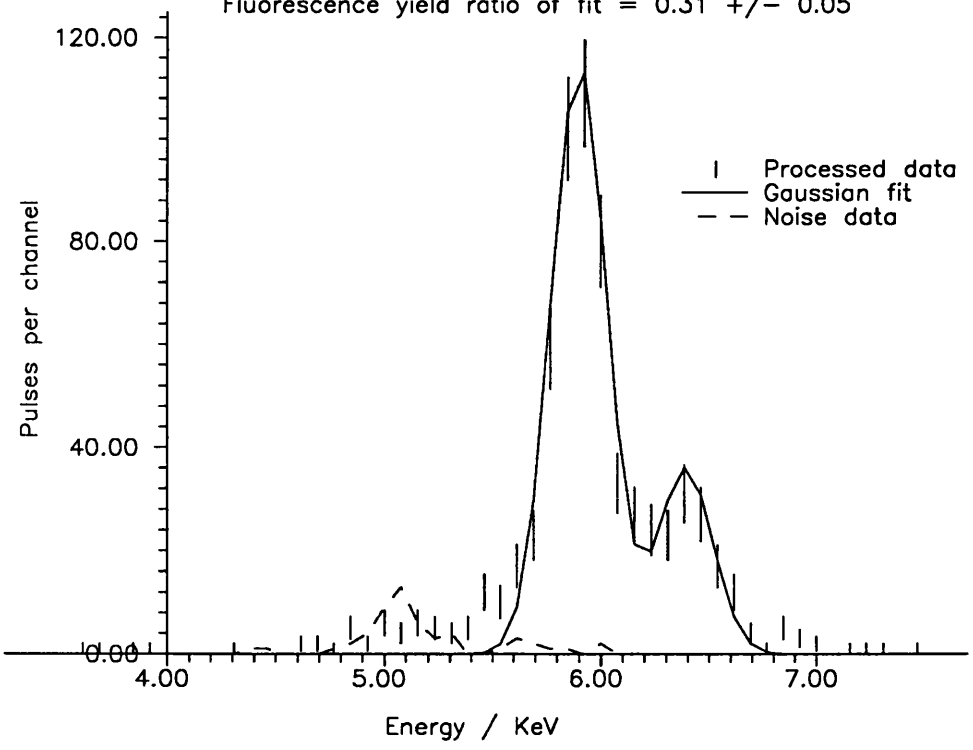

Figure 4.14: *FE4.20.11.DAT, 90 Rejection*

FE4.20.11.DAT Processed Data - Comments

This data was taken at 100 mK, with the detector observing the $^{55}_{26}$Fe source, on 20th November 1991. 750 pulses were recorded.

This is the first of the two datasets recorded in this run using the 8–bit analogue to digital converter. There is no reason to suppose that this should affect the resultant data, and these histograms resemble the previous dataset results.

The 4 KeV to 6 KeV noise has here been reduced by the rejection procedure, although only to about a half of its previous level.

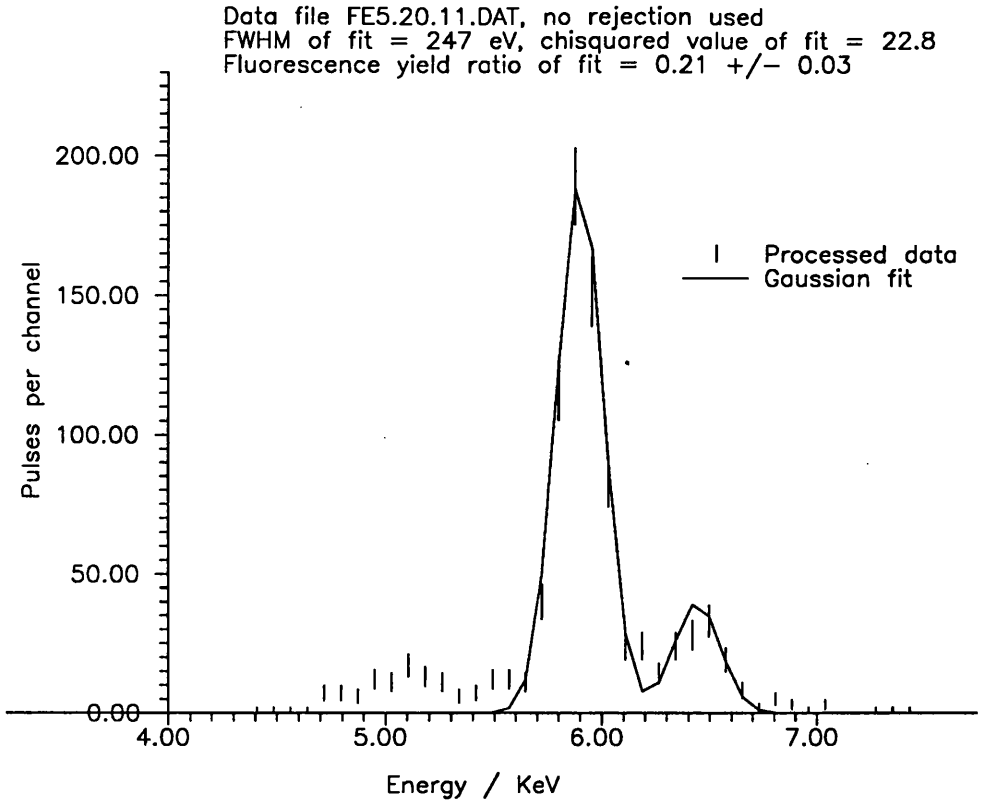

Figure 4.15: *FE5.20.11.DAT, no rejection*

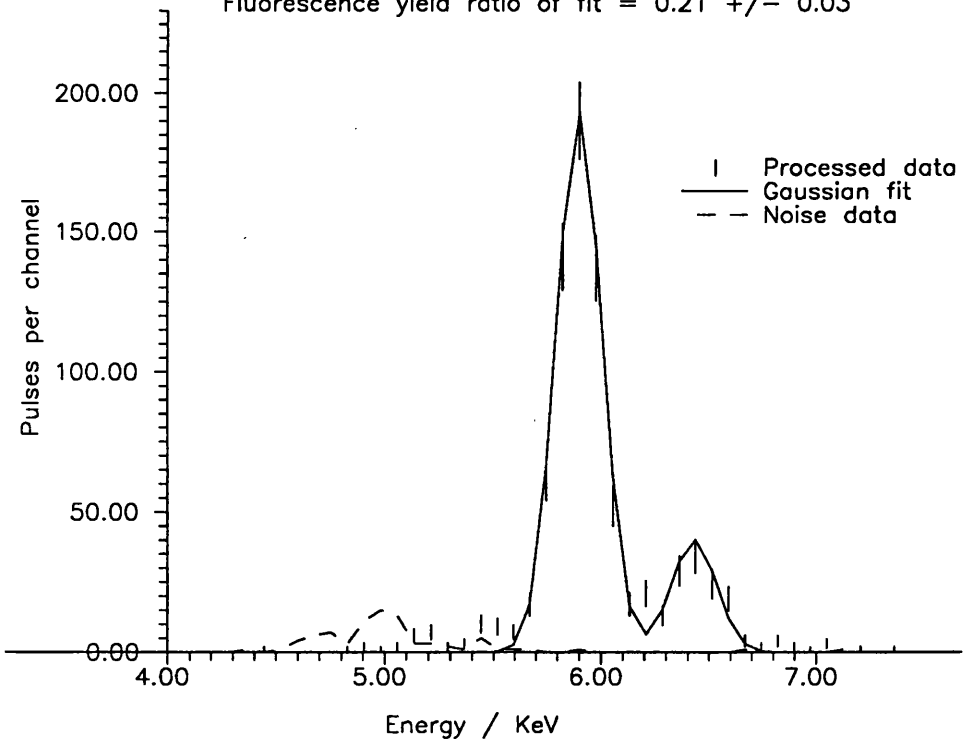

Figure 4.16: *FE5.20.11.DAT, 90 Rejection*

FE5.20.11.DAT Processed Data - Comments

This data was taken at 100 mK, with the detector observing the $^{55}_{26}$Fe source, on 20th November 1991. 913 pulses were recorded.

This is the other file in this run using the digital storage oscilloscope to record 8 bit data.

This is the file which contains the most pulses of all the datasets, and so has the smallest statistical error in the data points. This is most evident in the good fit obtained to the K_α peak seen, and the reduced uncertainty in the FYR.

Although the rejection procedure has removed some of the noise from the 4 KeV to 6 KeV region in this dataset, it is noticeable that most of the rejected pulses occur below 5.1 KeV, and a substantial number of noise pulses occur above this level, which are unaffected by the rejection. This suggests either that there are two forms of noise occurring in this region, caused by different sources, or that there is a gradual change in the pulse profile over the region, and that the rejection threshold is all that separates the rejected from the unrejected.

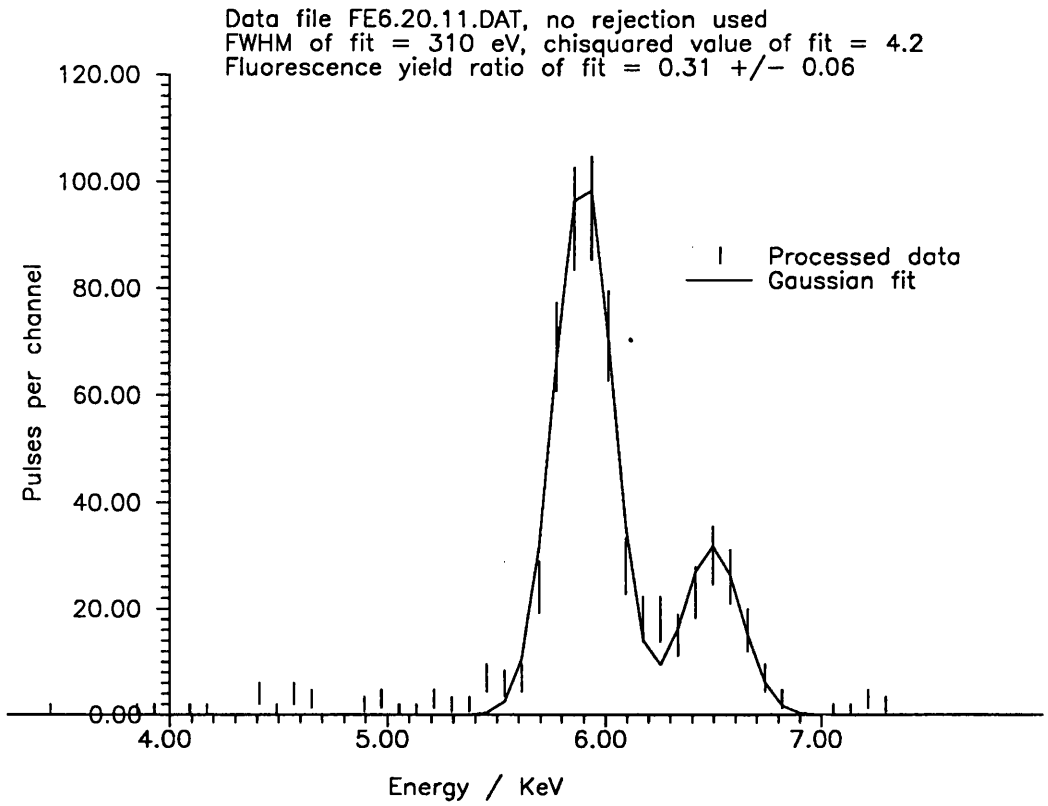

Figure 4.17: *FE6.20.11.DAT, no rejection*

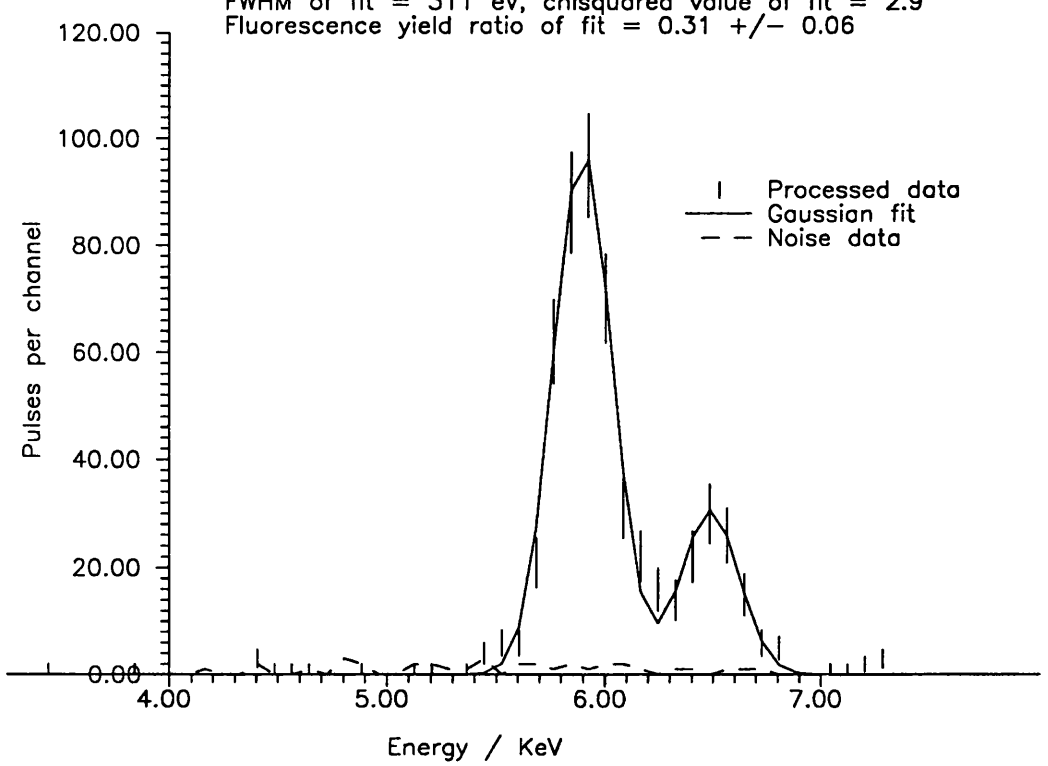

Figure 4.18: *FE6.20.11.DAT, 90 Rejection*

FE6.20.11.DAT Processed Data - Comments

This data was taken at 200 mK, with the detector observing the $^{55}_{26}$Fe source, on 20th November 1991. 600 pulses were recorded.

This is the first of the datasets recorded at the higher temperature of 200 mK, and it is noticeable that although the 4 KeV to 6 KeV noise is still present, it is at a substantially reduced level relative to the peaks. This and the more gaussian form of the two peaks gives a very low value of χ^2 for the histogram fit. The fit goes through the center of most of the data points, with the exception of the area between the two peaks, suggesting that this data is of good quality, which makes it curious that the fluorescence ratio between the two peaks is as high as 0.31, over twice the expected level.

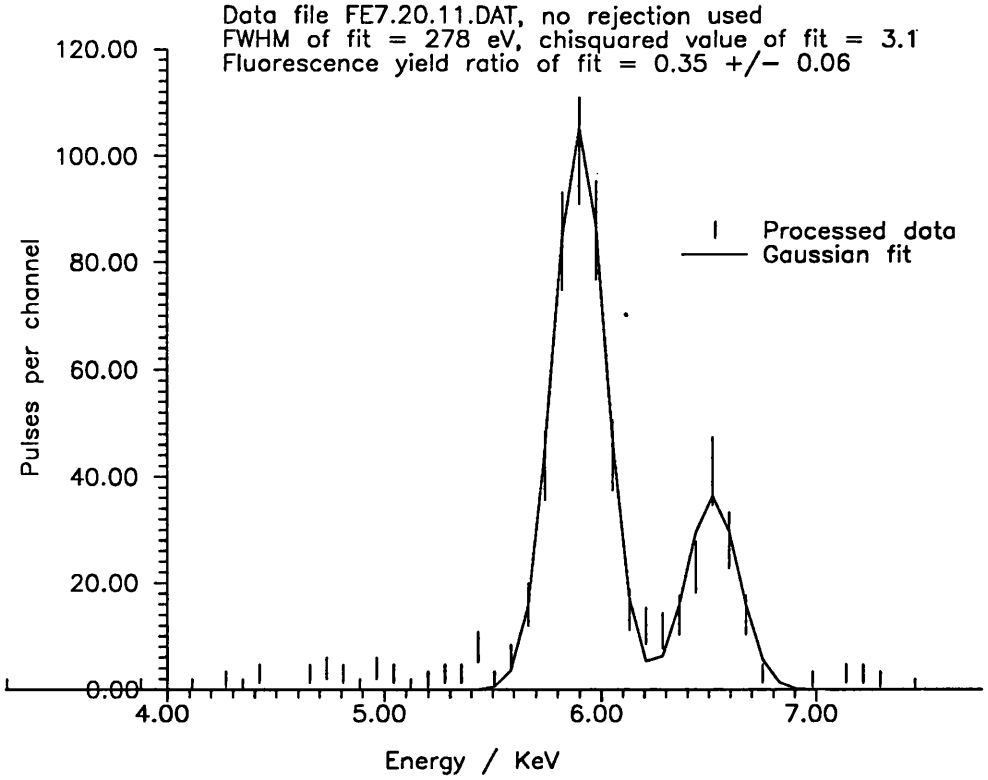

Figure 4.19: *FE7.20.11.DAT, no rejection*

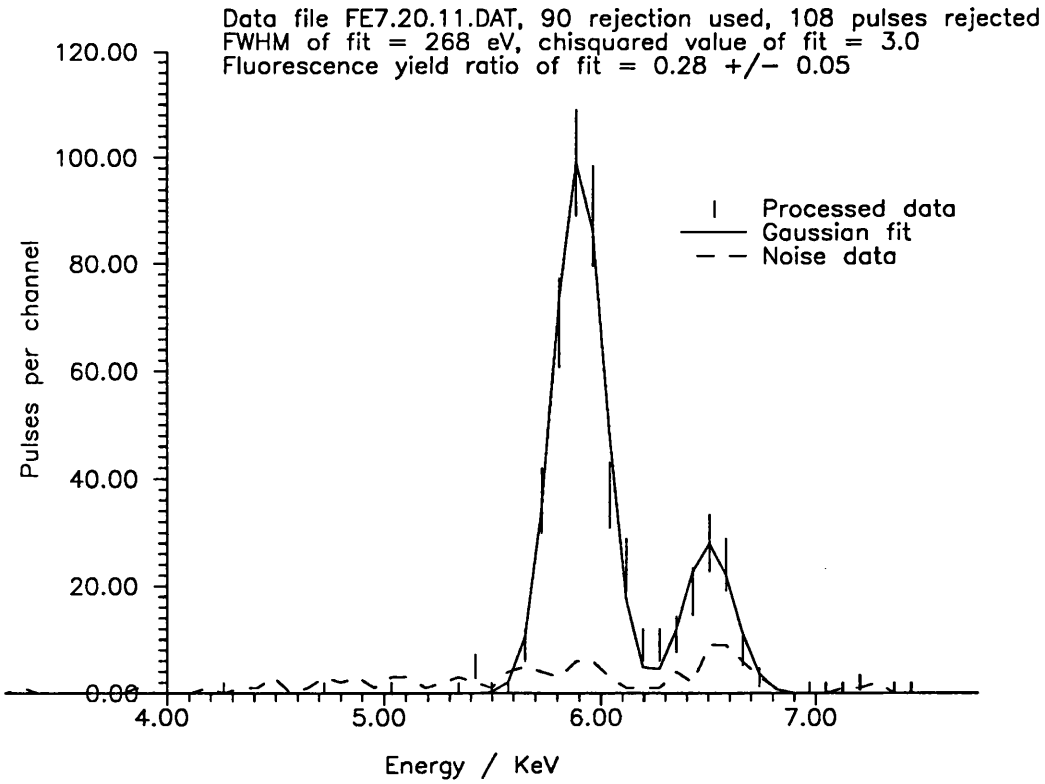

Figure 4.20: *FE7.20.11.DAT, 90 Rejection*

FE7.20.11.DAT Processed Data - Comments

This data was taken at 200 mK, with the detector observing the $^{55}_{26}$Fe source, on 20th November 1991. 600 pulses were recorded.

The low level of noise evident in this dataset is shown both graphically here, and can be inferred by the small size of the improvement in χ^2 between the pre- and post-rejection fits data. However, it is noticeable that a number of pulses around the region of the K_β peak have been rejected, and this has contributed to the lowering of the fluorescence yield ratio post-rejection, although it is still much higher than expected.

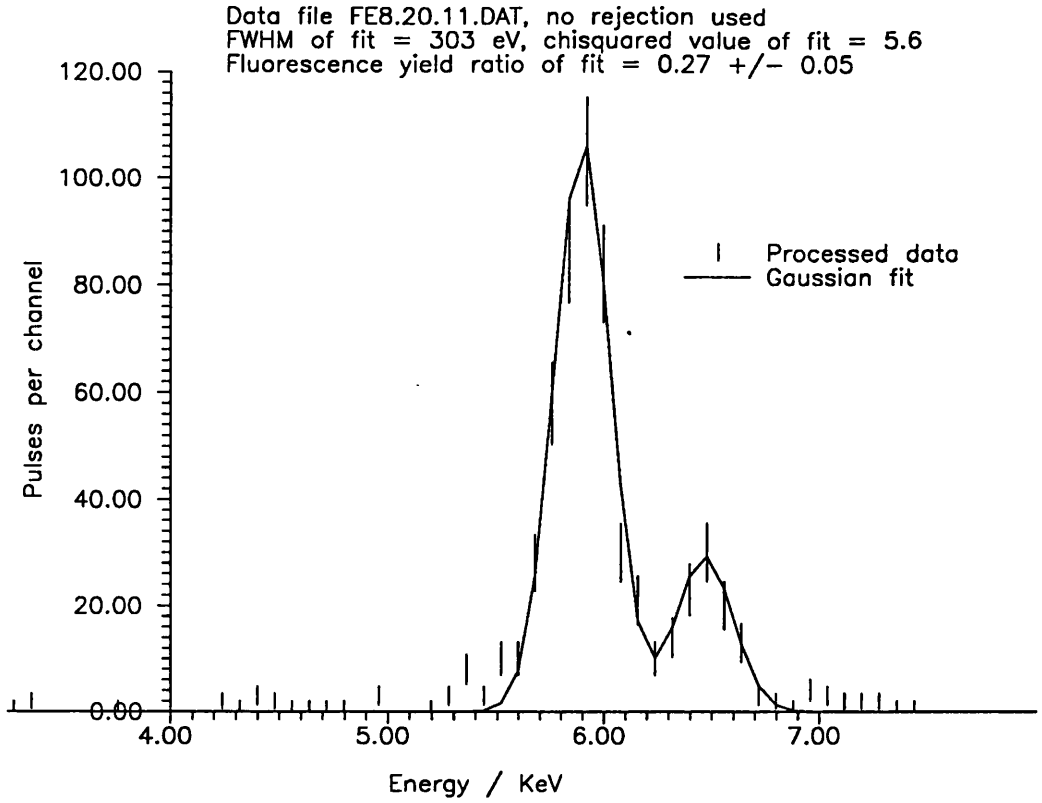

Figure 4.21: *FE8.20.11.DAT, no rejection*

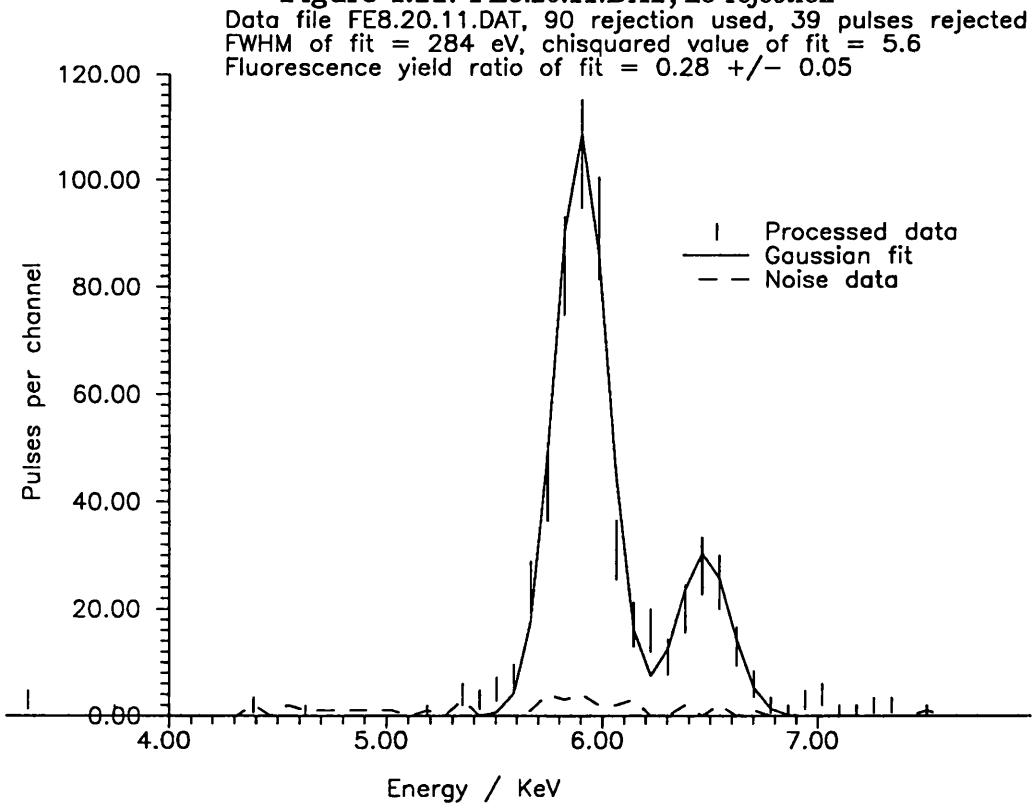

Figure 4.22: *FE8.20.11.DAT, 90 Rejection*

FE8.20.11.DAT Processed Data - Comments

This data was taken at 200 mK, with the detector observing the $^{55}_{26}$Fe source, on 20th November 1991. 600 pulses were recorded.

The level of 4 KeV to 6 KeV noise is very low in this case, and is slightly higher in the region of the peaks. Both of the peaks fit the gaussians very well, but the FYR is still higher than expected.

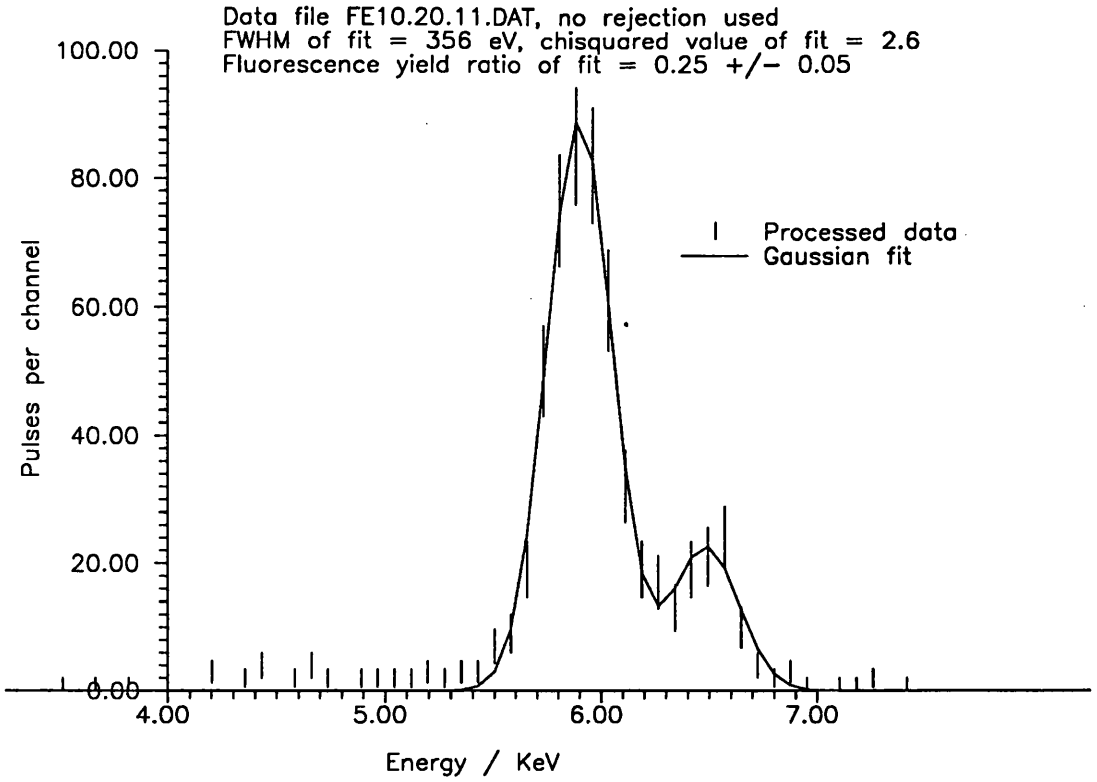

Figure 4.23: *FE10.20.11.DAT, no rejection*

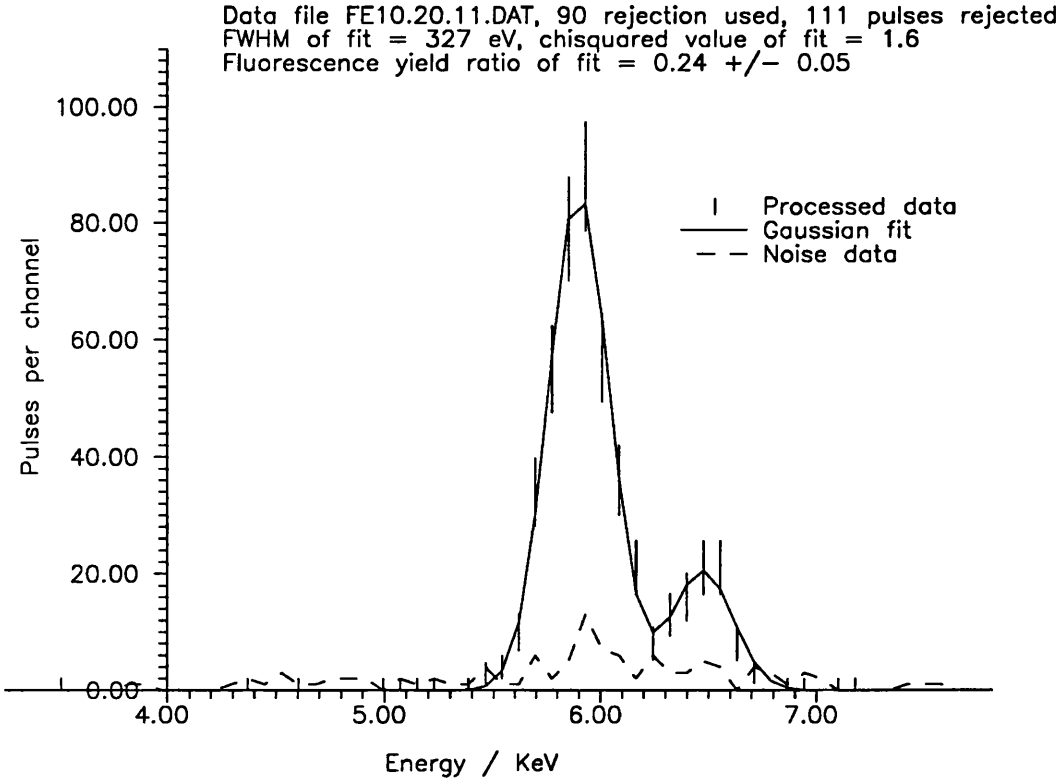

Figure 4.24: *FE10.20.11.DAT, 90 Rejection*

FE10.20.11.DAT Processed Data - Comments

This data was taken at 200 mK, with the detector observing the $^{55}_{26}$Fe source, on 20th November 1991. 600 pulses were recorded.

This dataset makes an interesting contrast with the previous one. The low level of rejected pulses actually come to a distinct peak at around the same energy as the K_α peak.

Although the K_α peak conforms well to the gaussian form, the K_β peak does not conform as well. the FYR is still around twice as high as expected.

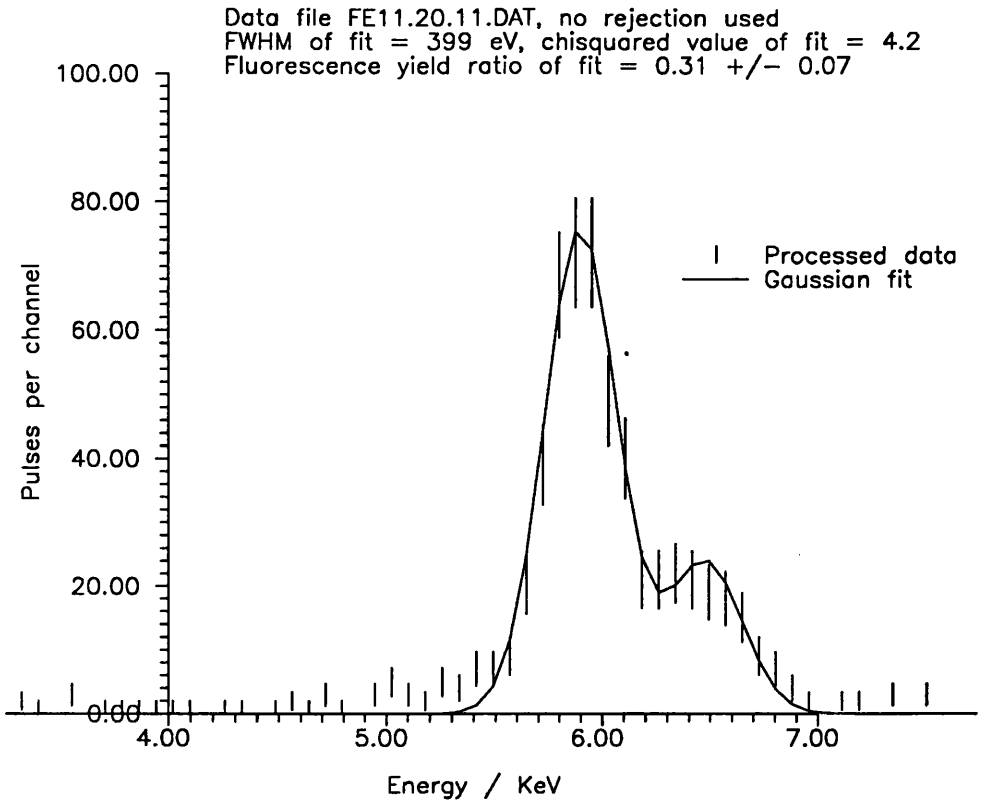

Figure 4.25: *FE11.20.11.DAT, no rejection*

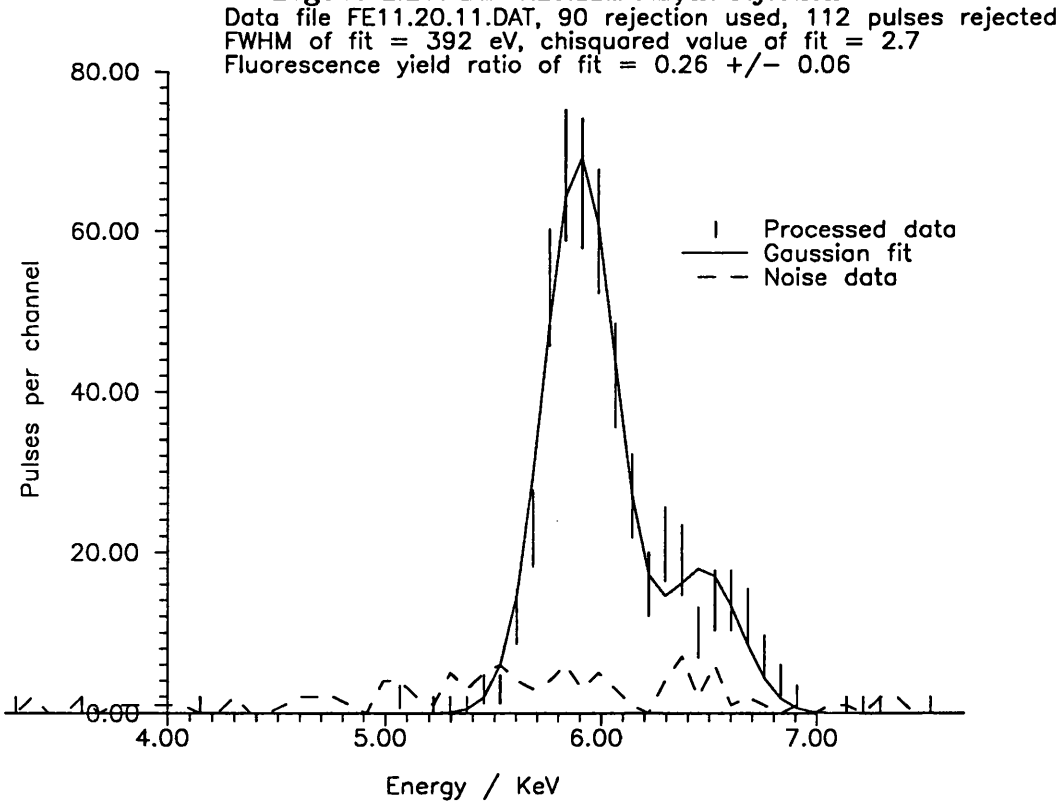

Figure 4.26: *FE11.20.11.DAT, 90 Rejection*

FE11.20.11.DAT Processed Data - Comments

This data was taken at 200 mK, with the detector observing the $^{55}_{26}$Fe source, on 20th November 1991. 600 pulses were recorded.

The K_β dataset histogram also has a rather odd form, and the FYR is therefore unreliable. The level of rejected noise is a little high relative to the peak heights. This is partially due to the greater FWHM of the peaks relative to the previous datasets, resulting in a lower absolute height in terms of pulses.

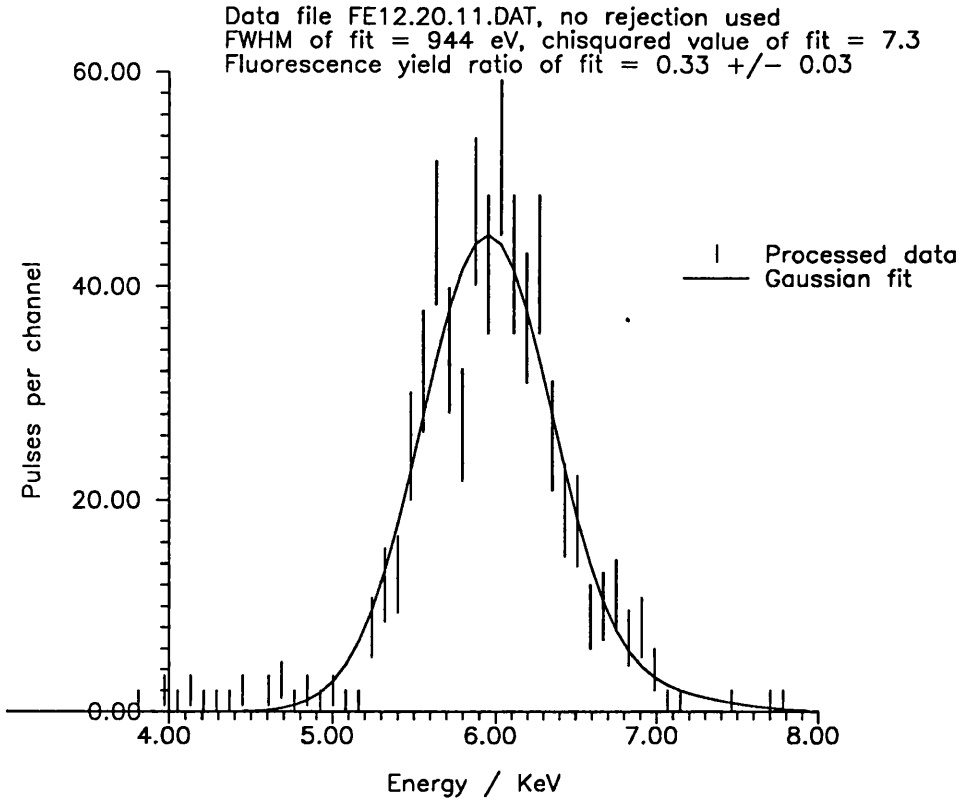

Figure 4.27: *FE12.20.11.DAT, No rejection*

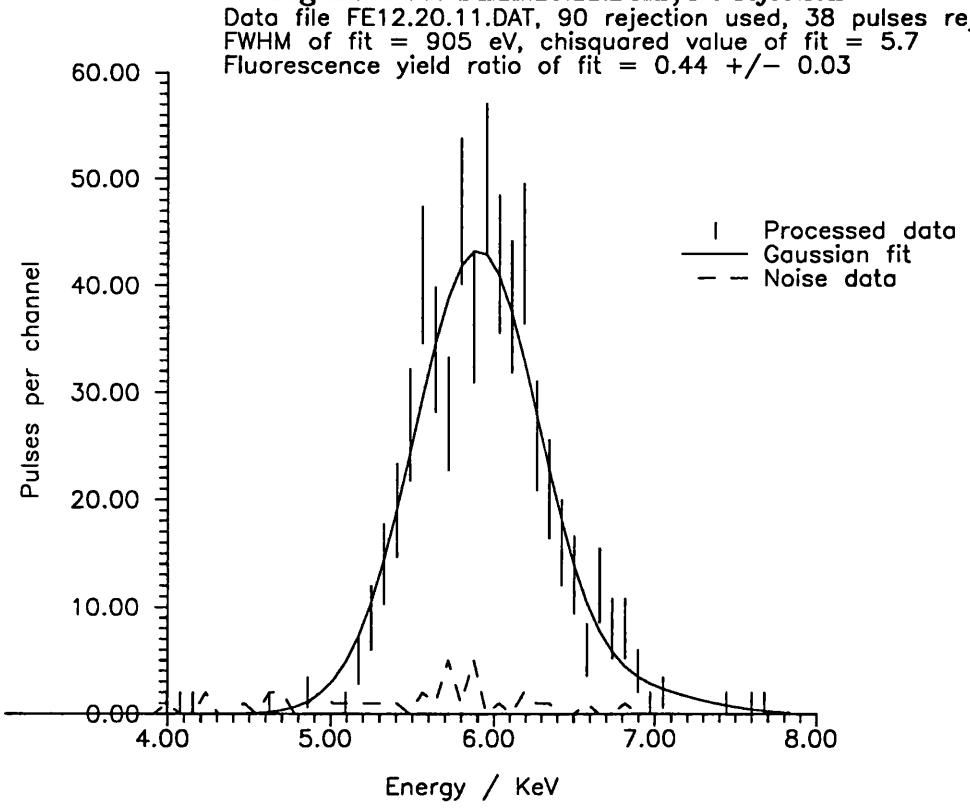

Figure 4.28: *FE12.20.11.DAT, 90 Rejection*

FE12.20.11.DAT Processed Data - Comments

This data was taken at 200 mK, with the detector observing the $^{55}_{26}$Fe source, on 20th November 1991. 600 pulses were recorded.

This dataset was the last taken of this run, and the temperature has drifted upwards with time. Since the resistivity of the detector is strongly dependent on its temperature, this drift has caused the pulse height to drift downwards with time, hence the peaks have spread out, and the distinction between the K_α and K_β peaks has been obliterated. This means that the fluorescence yield ratio value given by the fitting program is worthless.

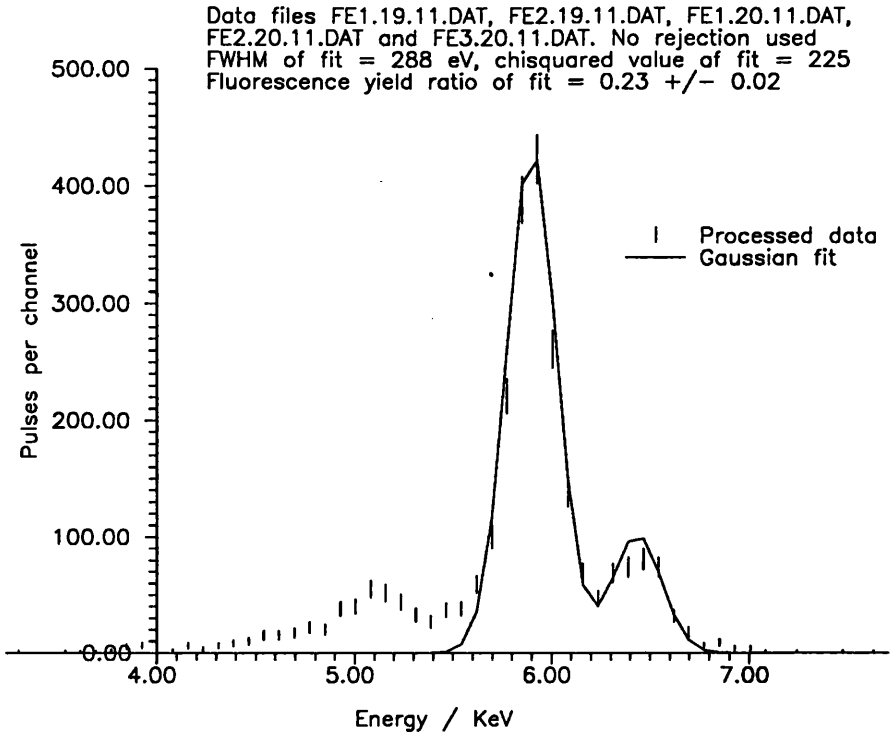

Figure 4.29: *100mK summed data, no rejection*

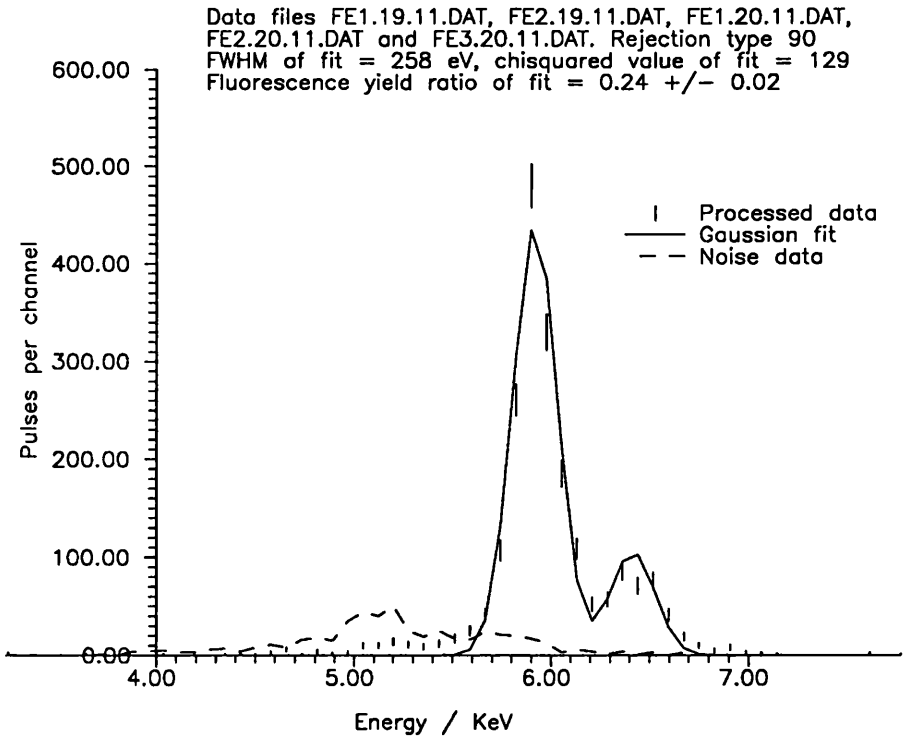

Figure 4.30: *100mK summed data, 90 Rejection*

4.3.2 100 mK Summed Data - Comments

This data was taken at 100 mK, with the detector observing the $^{55}_{26}$Fe source, on 19th and 20th November 1991. The summation comprises 2625 pulses.

As detailed earlier, this data is the sum of five of the 100 mK files. The summation was done largely to reduce the statistical error in each of the data points. This shows the 4 KeV to 6 KeV noise in better definition, and it seems as though there may well be a peak at around 5.1 KeV. The rejection process, again, manages to remove most of this noise, and shows this background separately from the main features.

In the pre-rejection case, the main peak is well fitted, however the upper two points on the k_β peak seem a little low, and the peak seems a little flat. The post-rejection K_β peak looks a little better, but the main peak seems to fit less well, presumably because of the wide K_β peak.

Possibly the most significant result of this histogram and fit is that the uncertainty in the χ^2 fit has been reduced further, and the FYR of 0.24 is still nearly twice the ratio expected.

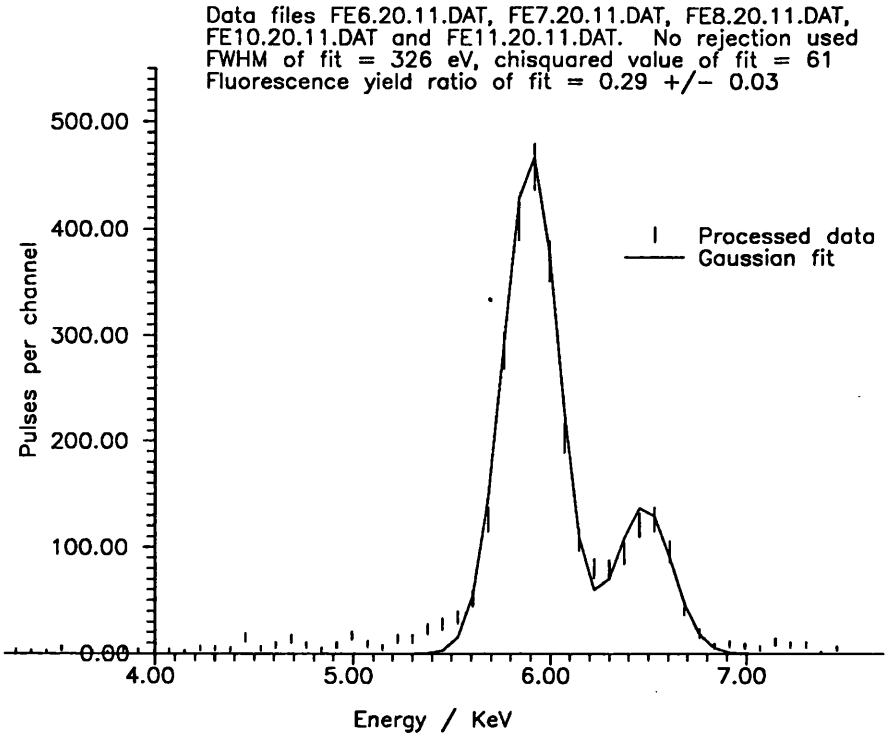

Figure 4.31: *200mK summed data, no rejection*

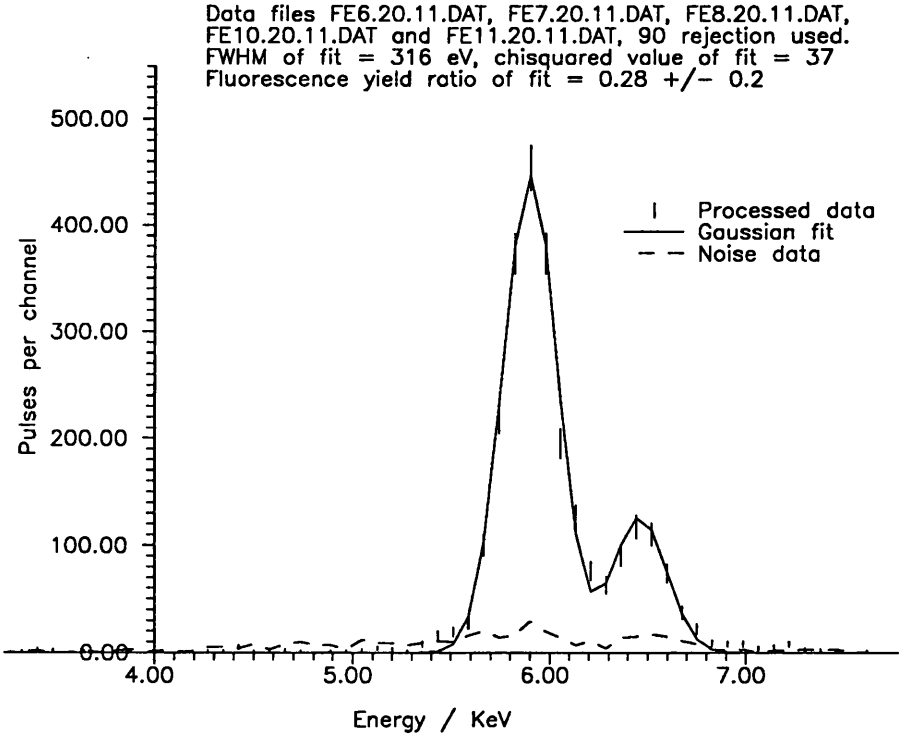

Figure 4.32: *200mK summed data, 90 Rejection*

4.3.3 200 mK Summed Data - Comments

This data was taken at 200 mK, with the detector observing the $^{55}_{26}$Fe source, on 20th November 1991. The summation comprises 3000 pulses.

This data is also the sum of five files, all of the 200 mK files except for the file FE12.20.11.DAT. As expected the 4 KeV to 6 KeV noise is substantially lower. Although the highest bin is close to 5 KeV, it is not really significant enough to claim that the same 5.1 KeV peak is present as with the 100 mK data.

It is notable, however, that the gaussian fit to the peaks is very good in both the pre-rejection and post-rejection cases, and this, combined with the decreased uncertainty arising from the large number of pulses involved, gives strong credence to the apparent fluorescence yield ratio being close to 0.28 at 200 mK.

4.4 Noise File Processing

The results in the following pages were obtained by adding each record in the noise file to a standard pulse generated from averaging a pulse file, and putting the resultant pulses through the processing system as before, using no rejection scheme. The technique is more fully described in Section 3.5.1.

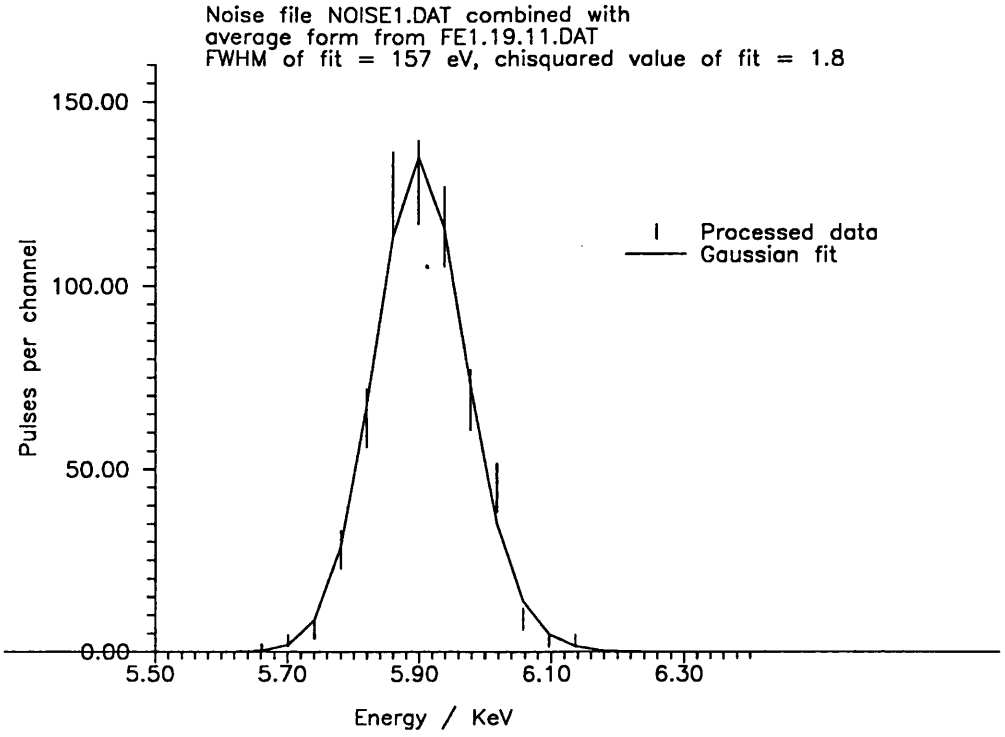

Figure 4.33: *File NOISE1.DAT*

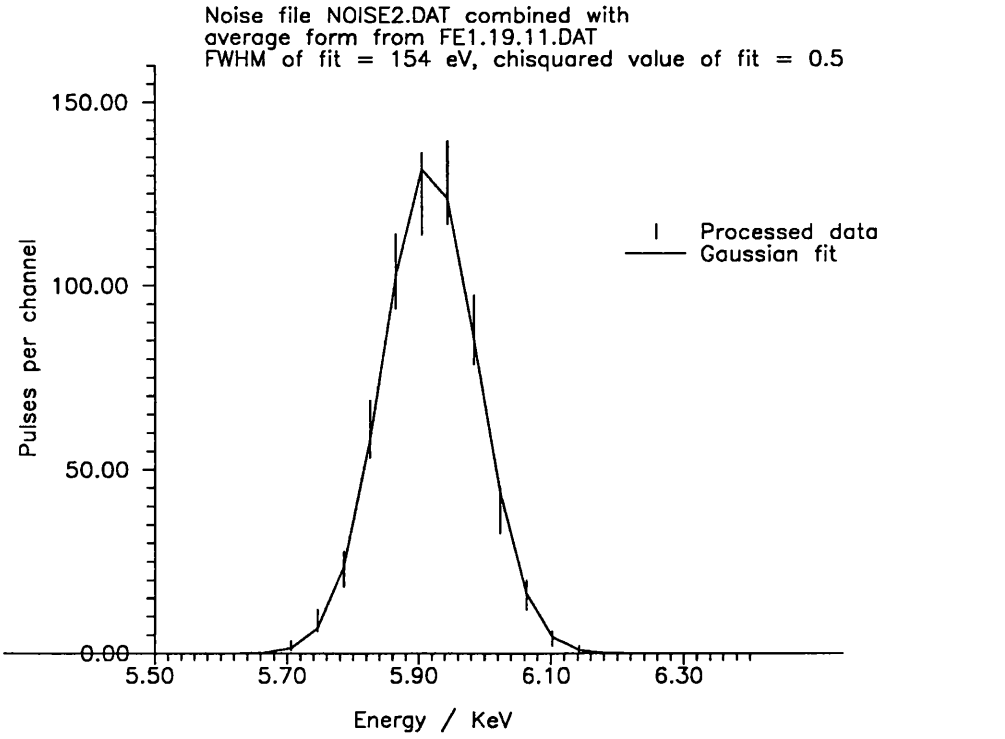

Figure 4.34: *File NOISE2.DAT*

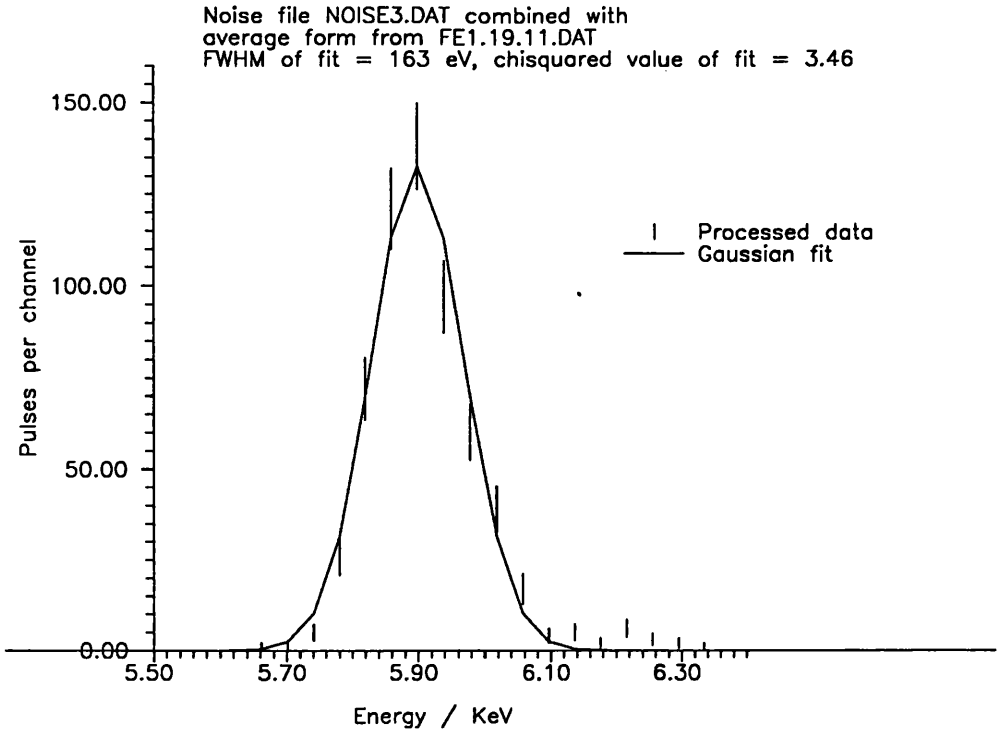

Figure 4.35: *File NOISE3.DAT*

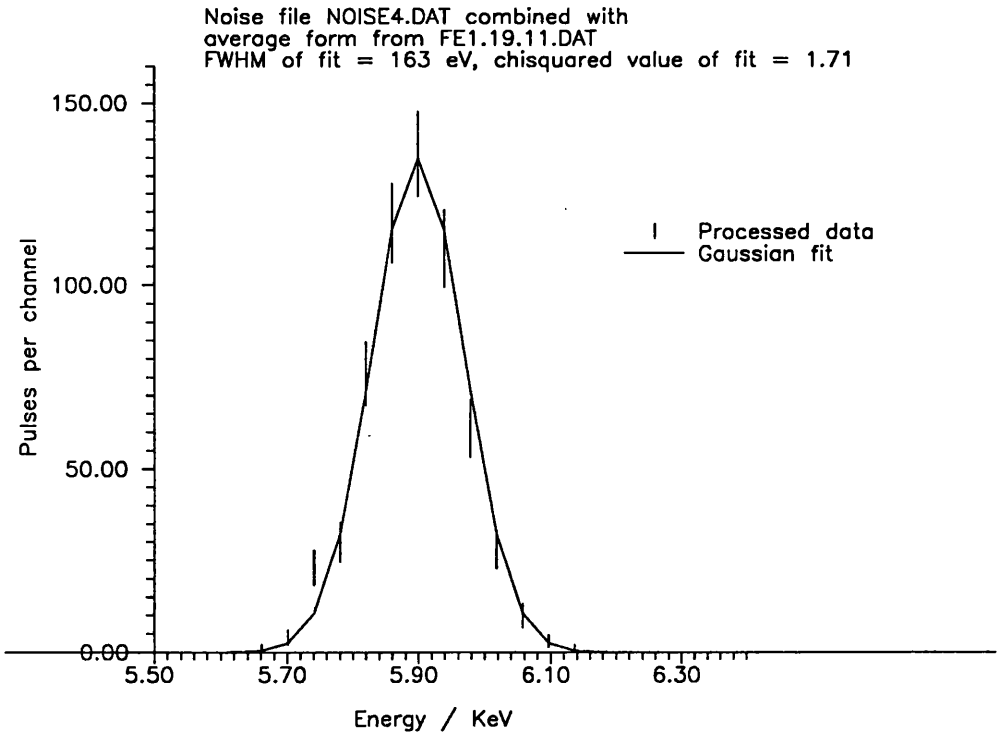

Figure 4.36: *File NOISE4.DAT*

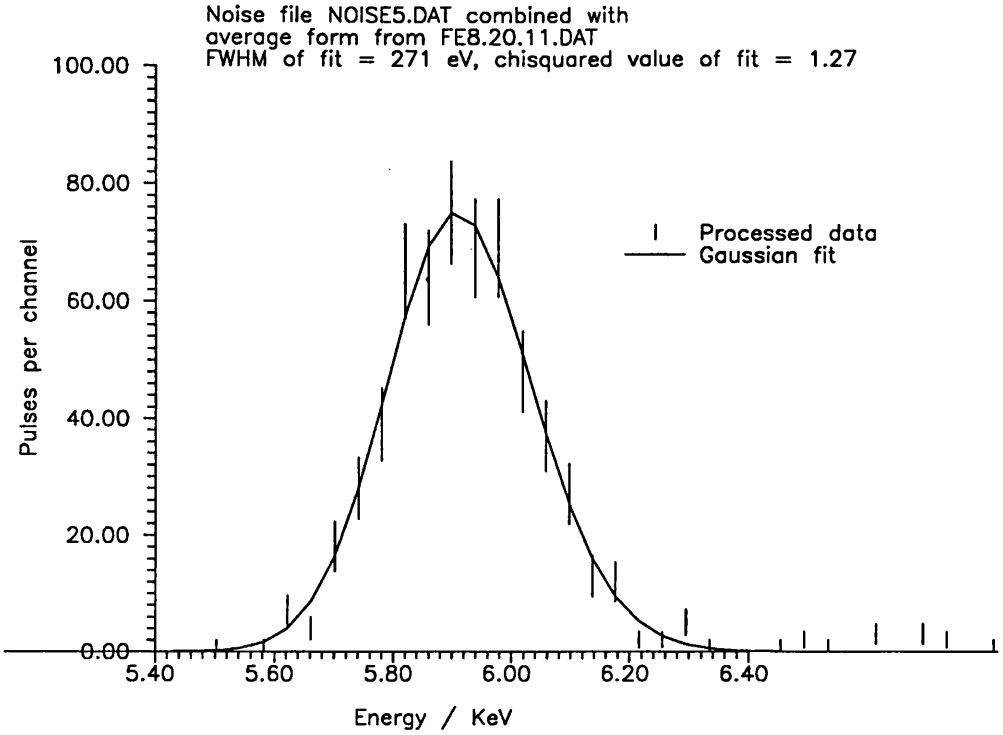

Figure 4.37: *File NOISE5.DAT*

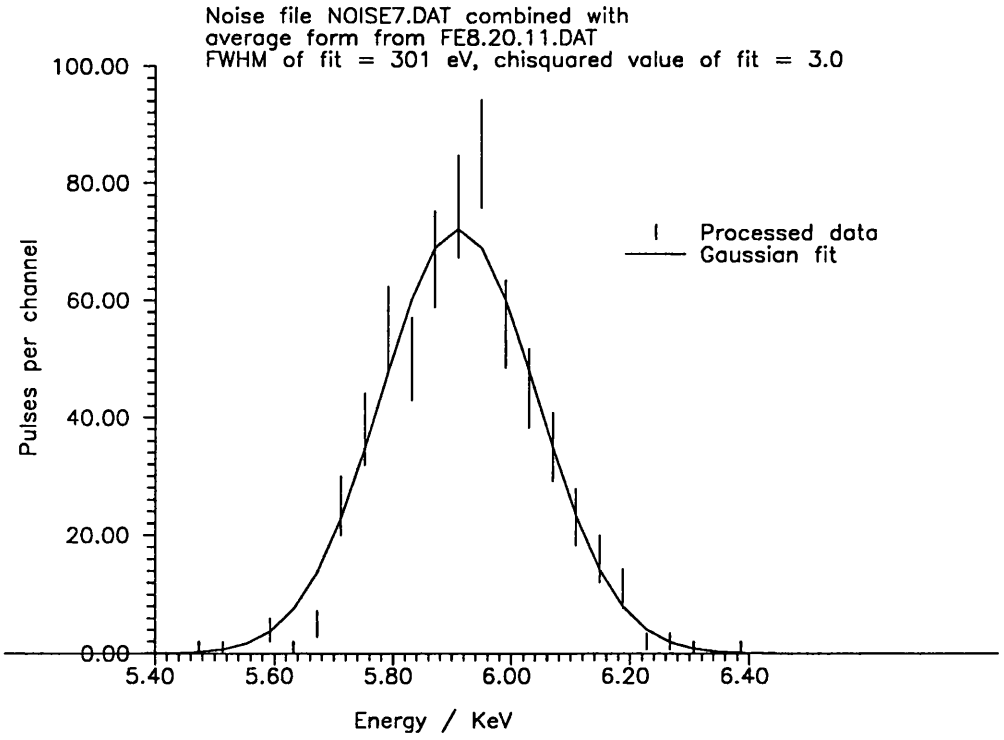

Figure 4.38: *File NOISE7.DAT*

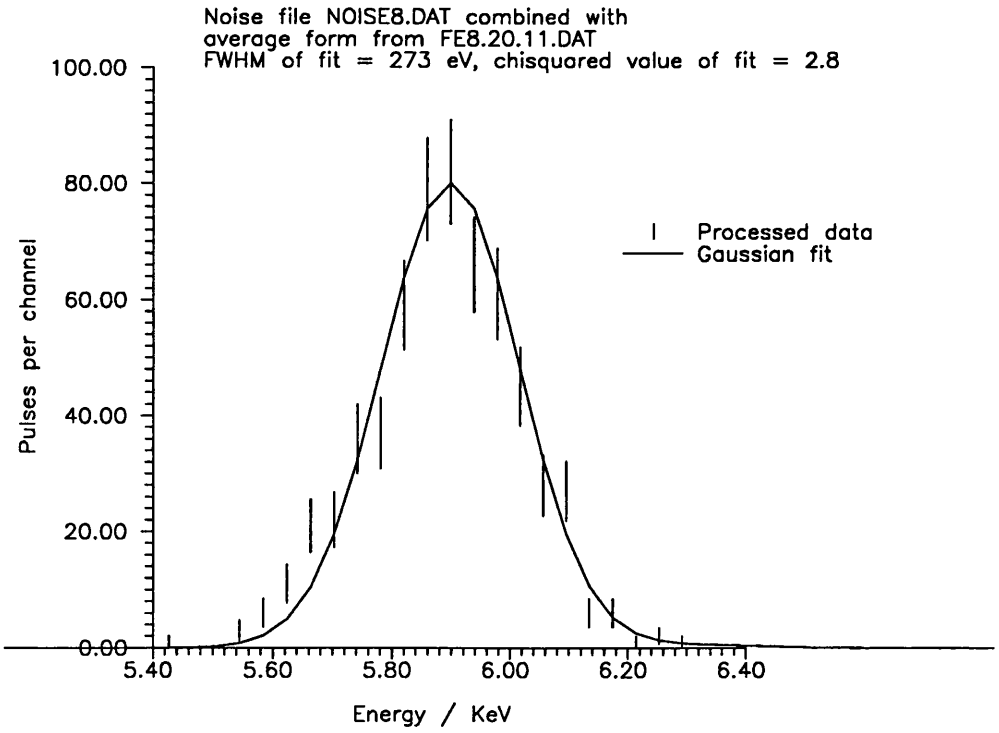

Figure 4.39: *File NOISE8.DAT*

4.5 Results of Processing

4.5.1 The Results of Rejection

In Table 4.2 I show the number of pulses rejected from each dataset using the χ^2 rejection technique. Since the technique remains the same throughout the run, any dramatic change indicates a physical change in the detector.

4.5.2 Resolution Obtained

In Table 4.3 the Full Width at Half Maximum (FWHM) of each of the datasets is presented, as determined by the gaussian fitting program. In accordance with the equation presented in Chapter 2 we would expect the obtained resolution to improve with lower temperature.

We do observe some improvement with the lower temperature, however it is only approximately a 13 % reduction in FWHM for a halving of the operating temperature.

4.5.3 Quality of Gaussian fit to histogram

In Table 4.4 I tabulate the factors which show how well the gaussian fits to the energy histograms match the data provided by the matched filter program. All of the data binning is performed by scaling the pulse height in such a way that the K_α peak occurs around the 80th bin, and 100 bins are used in total. The χ^2 value shown on the graphs in the previous pages, and below, are the mean value of χ^2 per bin averaged over all 100 bins.

The improvement factor is simply the value of χ^2 obtained from the fit to the pre-rejection data divided by the the post-rejection value. Hence a dataset with an improvement factor of 2 is fitted twice as well after the abnormal pulses have been rejected.

How many pulses were rejected				
File	Temp. (mK)	Number of pulses	Number rejected	Percentage rejected
FE1.19.11.DAT	100	600	115	19
FE2.19.11.DAT	100	600	112	19
FE3.19.11.DAT	100	600	104	17
FE1.20.11.DAT	100	600	121	20
FE2.20.11.DAT	100	284	62	22
FE3.20.11.DAT	100	541	105	19
FE4.20.11.DAT	100	750	57	8
FE5.20.11.DAT	100	913	84	9
FE6.20.11.DAT	200	600	37	6
FE7.20.11.DAT	200	600	108	18
FE8.20.11.DAT	200	600	39	7
FE10.20.11.DAT	200	600	111	19
FE11.20.11.DAT	200	600	112	19
FE12.20.11.DAT	200	600	38	6

Table 4.2: *Pulse rejection statistics*

FWHM Results					
File	Temp. (mK)	FWHM (eV) (Rejection type[1]) None	90	FWHM Improvement with rejection	Number of bits used
FE1.19.11.DAT	100	311	295	5.1 %	12
FE2.19.11.DAT	100	290	275	5.2 %	12
FE3.19.11.DAT	100	394	383	2.8 %	12
FE1.20.11.DAT	100	235	222	5.5 %	12
FE2.20.11.DAT	100	240	221	7.9 %	12
FE3.20.11.DAT	100	294	279	5.1 %	12
FE4.20.11.DAT	100	275	291	-5.8 %	8
FE5.20.11.DAT	100	247	238	3.6 %	8
Mean Values		286	276	3.7 %	—
100 mK combined file	100	288	258	10.4 %	12
FE6.20.11.DAT	200	310	311	-0.3 %	12
FE7.20.11.DAT	200	278	268	3.6 %	12
FE8.20.11.DAT	200	303	284	6.3 %	12
FE10.20.11.DAT	200	356	327	8.1 %	12
FE11.20.11.DAT	200	399	392	1.8 %	12
Mean Values		329	316	4.0 %	—
200 mK combined file	200	326	316	3.1 %	12
FE12.20.11.DAT	200	944	905	4.1 %	12

Table 4.3: *FWHM Results*

It can be seen that on only one occasion is the fit not improved by the rejection procedure, and on this occasion the fit is not degraded by the procedure.

4.5.4 Fluorescence Yield Ratio

The fluorescence yield ratio (FYR) is the proportion of K_β photons recorded compared to K_α photons. As mentioned earlier, we expect this ratio to be in the range 0.12 to 0.14. Since the individual files show that the FYR seems too high, it is worthwhile tabulating the FYR for each file to attempt to divine a pattern.

In Table 4.5 are listed the FYRs calculated according to the gaussian fits for each of the datasets, including the datasets which are composites of the 100 mK and 200 mK datasets respectively.

The pattern shown in the table seems to suggest that when operated at 100 mK, the detector registers a fluorescence yield ratio of approximately 0.23, whereas when operated at 200 mK, the ratio is closer to 0.29.

4.5.5 Point Spread Function, Internal Noise

In Table 4.6, the FWHM calculated for each of the noise files when combined with a suitable file is listed. In the case of the 100 mK files, each noise trace is added to the average form from file FE1.19.11.DAT, and the 200 mK noise traces are added to the from from file FE8.20.11.DAT.

It is quite notable from the table that the baseline noise has reduced by a factor of 2 between the temperatures of 200 mK and 100 mK. This would appear to be solely attributable to the lower operating temperature.

Quality of Energy Histogram Fitting			
File	Value of χ^2		Improvement factor
	no rejection	90 rejection	
FE1.19.11.DAT	19.0	10.0	1.90
FE2.19.11.DAT	16.9	10.6	1.59
FE3.19.11.DAT	14.5	5.2	2.79
FE1.20.11.DAT	19.4	7.2	2.69
FE2.20.11.DAT	6.2	2.2	2.82
FE3.20.11.DAT	8.1	2.9	2.79
FE4.20.11.DAT	15.2	9.9	1.54
FE5.20.11.DAT	22.8	9.7	2.35
FE6.20.11.DAT	4.2	2.9	1.45
FE7.20.11.DAT	3.1	3.0	1.03
FE8.20.11.DAT	5.6	5.6	1.00
FE10.20.11.DAT	2.6	1.6	1.63
FE11.20.11.DAT	4.2	2.7	1.56
FE12.20.11.DAT	7.3	5.7	1.28

Table 4.4: *Energy Histogram Fitting*

Fluorescence Yield Ratio			
File	Temperature (mK)	FYR	
		no rejection	90 rejection
FE1.19.11.DAT	100	0.24 ± 0.05	0.24 ± 0.05
FE2.19.11.DAT	100	0.24 ± 0.04	0.24 ± 0.05
FE3.19.11.DAT	100	0.23 ± 0.05	0.23 ± 0.06
FE1.20.11.DAT	100	0.21 ± 0.04	0.22 ± 0.04
FE2.20.11.DAT	100	0.27 ± 0.07	0.29 ± 0.07
FE3.20.11.DAT	100	0.24 ± 0.05	0.24 ± 0.05
100 mK combined	100	0.23 ± 0.02	0.24 ± 0.02
FE4.20.11.DAT	200	0.30 ± 0.06	0.31 ± 0.05
FE5.20.11.DAT	200	0.21 ± 0.03	0.21 ± 0.03
FE6.20.11.DAT	200	0.31 ± 0.06	0.31 ± 0.06
FE7.20.11.DAT	200	0.35 ± 0.06	0.28 ± 0.05
FE8.20.11.DAT	200	0.27 ± 0.05	0.28 ± 0.05
FE10.20.11.DAT	200	0.25 ± 0.05	0.24 ± 0.05
FE11.20.11.DAT	200	0.31 ± 0.07	0.26 ± 0.06
200 mK combined	200	0.29 ± 0.03	0.28 ± 0.02
FE12.20.11.DAT	200 varying	0.33 ± 0.03	0.44 ± 0.03

Table 4.5: *Fluorescence Yield Ratio*

Baseline Noise Results		
File	Temperature (mK)	FWHM (eV)
NOISE1	100	157
NOISE2	100	154
NOISE3	100	163
NOISE4	100	163
100 mK average		159
NOISE5	200	271
NOISE7	200	301
NOISE8	200	273
200 mK average		282

Table 4.6: *Noise Data*

4.6 Conclusions

4.6.1 Rejection Statistics

Although there is some variation in the percentage of pulses within each file rejected, between 6 % and 22 %, there is no discernible pattern in this variation, and must therefore be dismissed as statistical, or due to factors not recorded at the time of the run.

If we consider that 15 % of the pulses are rejected on average, this represents approximately 90 pulses in a 600 pulse run. Statistical variance in this number is approximately 9 pulses, which yields a range of 13 % to 17 %, and only accounts for a small part of the variation in the rejection percentage. We must therefore assume that some other factor is responsible for this strange anomaly.

4.6.2 Full Width at Half Maximum

The full width at half maximum (FWHM) of the individual datasets is of some interest. As mentioned earlier, the expected improvement in resolution with reduced temperature has not emerged, and there are a number of possible explanations for this.

- The detector used was one optimized for use at 300 mK. This means that its resistance at 300 mK is around the ideal value given in Chapter 2. However, the resistance of a semiconductor is strongly dependent on its temperature, and going from 300 mK to 100 mK greatly increases its resistance, and the related V-I behaviour. In order to reduce its resistance closer to an ideal value, a higher current is driven through the detector, and although this does achieve the object, it also increases the temperature of the detector, and hence increases the thermodynamic fluctuations within it, and degrades the performance of the device. In Section 4.6.5 I argue that the detector may have been operating at a temperature as high as 159 mK for this reason.

- The interaction of the X-ray with the germanium detector, rather than with a thermalising medium has unfortunate side effects as described in Chapter 2. The presence of electron traps in semiconductors is only one means by which electrons may be lost, and the variable number of these thus removed from the conduction process with each X-ray event causes some degradation of resolution.

4.6.3 Quality of Fit

It is notable that the fits to the 100 mK files are improved to a greater degree by the rejection than the fits to the 200 mK files. This is largely due to the lower level of the 4 KeV to 6 KeV noise evident in the 200 mK datasets.

Visually inspecting the one dataset in which no improvement in fit is yielded by the pulse rejection procedure, the FE8.20.11.DAT set, it is clear that this is a very 'clean' dataset. Both the K_α and K_β peaks are highly gaussian in form, the fit passes through virtually all of the data points, and only a very low level of noise needs to be removed.

4.6.4 Fluorescence Yield Ratio (FYR)

The FYR anomaly is quite interesting and unexpected. Firstly the nature of the anomaly is odd, in that the result is further away from the expected value when operating closer to the previous operating temperature of the detector. The same detector has previously been operated at 300 mK. The results obtained in the processing performed by Hepburn on the 300 mK data suggests that the FYR was close to 0.18 ± 0.05, which puts it too high, although just within statistical uncertainty. It is therefore odd that the 200 mK results differ more from the 300 mK data than the 100 mK data, in respect of the FYR.

One possibility is the presence of the 4 KeV to 6 KeV noise prominently evident in the 100 mK data, but still visible at 200 mK. It seems possible that the spectrum of this noise is such that it is superimposed onto the genuine data, and is therefore

distorting the heights of the peaks, and thence the FYRs. Whilst previously I have considered that this noise is less evident at 200 mK solely because the factors behind it are temperature dependent, it is possible that at 200 mK the noise has simply moved up in energy, and the main peak is under the Mn K_β peak, hence enhancing its height, and causing the increased FYR. However, the height of this noise at 200 mK does not seem enough if extrapolated to increase the height of the K_β peak sufficiently, or explain the 100 mk anomaly.

4.6.5 Point Spread Function, Internal Noise

At 200 mK the FWHM of the noise is very close to the FWHM observed when genuine pulses were recorded at 200 mK. This suggests that the baseline noise is dominant over all other sources at 200 mK. Since the 100 mK noise FWHM is half that of the pulse data, this suggests that another source of noise is also strong at 100 mK.

Since the mean internal noise at 100 mK yields a FWHM of 159 eV, and the mean 100 mK X-ray event FWHM as shown in Table 4.3 is 276 eV after rejection, then assuming that the noise sources add in quadrature, the other sources of noise contribute 226 eV.

At 200 mK, the mean internal noise contribution to FWHM is 282 eV, and the mean 200 mK X-ray event FWHM from Table 4.3 is 316 eV, then the other sources of noise contribute 143 eV at 200 mK.

We would expect that the variation in this internal noise, caused chiefly by thermodynamic fluctuations in the detector, should obey the equation from Chapter 2, and have a dependence on $T^{5/2}$. If this were the case then the noise at 100 mK should be a factor of 5.6 less than at 200 mK. This is clearly not the case. Referring back to the possible explanation cited for the failure to achieve the resolution improvement expected by operating at a lower temperature in Section 4.6.2, it seems more likely that the detector was operating at an increased temperature due to the passed current. The decrease in thermal noise evident here, a factor of 1.77 reduction, indicates that the 100 mK run was operating at 159 mK.

4.6.6 The 4 KeV to 6 KeV Noise

Some noise occurs in the energy region 4 KeV to 6 KeV. It is evident in the energy histograms at both temperatures, however it is approximately five times more prominent at 100 mK than it is at 200 mK. In the 100 mK composite data the form of this noise is shown quite well, and there seems to be a peak around 5.1 KeV.

Since the $^{55}_{26}$Fe source is extremely pure, it seems likely that the mechanism for this noise is in the detector itself. Somehow, it would seem that some of the X-rays incident on the semiconductor are losing around 1 KeV of energy in the thermalisation process.

The main difference between the research of the *University of London* group, and that of the other microcalorimetry groups, is that other groups decided early on to use a detector consisting of an absorber connected to the semiconductor. The *University of London* group have avoided the use of an absorbing medium thus far because of the vast increase in the heat capacity such a medium causes.

Since other groups have not experienced this noise, it seems likely that the noise is due to using the semiconductor as the thermaliser. Unfortunately, very little work has been done by anyone in the field of semiconductor physics at temperatures in the very low temperature region, and it is therefore difficult to determine what mechanism has caused this energy loss.

One might suppose that this noise is due to metastable electron trapping, the creation of electron-hole pairs which retain some of the energy of thermalisation for some time. If this was the case, then we would expect a long tail to be present on thusly affected pulses. What also may trap electrons is the presence of potential wells in the semiconductor. Imperfections in the crystal lattice can cause very deep wells, and may trap electrons for a far greater time than the duration of the pulse. The eventual release of this energy may occur long after the recording has finished.

It is also possible that some of the electrons that make up the bias current are taking some of the thermalisation energy away from the detector before it can be

given to phonons.

Bibliography

[1] *Compilation of X-ray Cross-sections* - W.H. MacMaster, N. Kerr Del Grande, J.H. Mallett, J.H Hubbell - National Bureau of Standards - Lawrence Radiation Laboratory.

[2] *Atomic FYs* - R.W. Fink, R.C. Jopson, Hans Mark, C.D. Swift, Rev. Mod. Phys. Vol.38 No.3 pp. 513-536, July 1966

[3] *X-ray Fluorescence Yields, Auger and Coster-Koenig Transition Probabilities* - Walter Bambynek, Bernd Crasemann, R.W. Fink, H.U. Freund, Hans Mark, C.D. Swift, R.E. Price, P. Venugopala Rao, Rev. Mod. Phys. Vol.44 No.4 pp.716-813, October 1972

Chapter 5

General Refrigeration Techniques

5.1 The Need for Refrigeration

The performance of a resistive X-ray microcalorimeter is greatly improved with a reduction in operating temperature. This is chiefly due to the reduction in thermodynamic fluctuations in the detector material. The noise energy contributed by thermodynamic fluctuation is given in Chapter 2 as

$$\Delta E = \xi T (k_B C)^{\frac{1}{2}}$$

The Debye approximation for heat capacity is applicable at low temperatures, and yields heat capacity C as proportional to T^3. This makes ΔE proportional to $T^{5/2}$, and hence there is a strong dependence of noise energy on temperature. This makes it highly desirable to operate at as low a temperature as possible.

5.2 The Use of Liquid Cryogens

5.2.1 Cooling by Nitrogen Evaporation

Nitrogen is the most abundant gas in the atmosphere, and hence is exceptionally cheap to obtain. At standard pressure it liquifies at 77 K, and hence in its liquid form is a useful cryogen. Once nitrogen has been liquified, keeping a bath of it in thermal contact with an object at a higher temperature causes a flow of heat from the object to the nitrogen. The migration of this heat causes the temperature of the object to drop, until the object and the cryogen are in thermal equilibrium. As the object cools, the nitrogen becomes warmer, until the temperature reaches the boiling point, and some nitrogen is boiled off as it is supplied with its latent heat of vaporisation, and no longer participates in the cooling.

Nitrogen is commonly used in the laboratory as a means to lower apparatus to a temperature of 77 K, since it is possible with suitable insulation to maintain such an environment for long periods of time. A typical nitrogen cryostat will consist of a vacuum jacket, which is silvered to reduce radiative transfer between the nitrogen and the outside world, inside which is a cavity to contain the nitrogen.

It is also common to use a nitrogen layer outside another cooling device, which can then reduce the temperature of the apparatus even further down.

5.2.2 Cooling by ^{4}Helium Evaporation

Helium is the second most abundant gas in the Universe, and is usually used to obtain temperatures in the laboratory below those offered by nitrogen. At standard pressure ^{4}He liquifies at 4 K, and when used in the same manner as described above for nitrogen, can bring the temperature of the object down to 4 K. However, when the pressure of helium gas is reduced significantly, the boiling/liquifaction temperature comes down to 0.8 K. A very low pressure is required to reduce this temperature so low, however, and 1.5 K is often the compromise temperature achieved by pumping on a bath of ^{4}He.

A helium cryostat usually consists of an outer vacuum jacket, with silvered sides to reduce radiative heat flow, with a nitrogen layer inside, another silvered vacuum layer, and then the helium bath, which is designed in such a way as to make it possible to pump on the bath, and hence obtain the lower temperature made available by this technique.

5.2.3 Cooling by ^{3}Helium Evaporation

^{3}He is the less abundant isotope of helium which possesses only one neutron in its atom, making the nucleus a fermion, obeying Fermi-Dirac statistics, whereas ^{4}He is a boson, and obeys Bose-Einstein statistics. The most basic result of this difference is that whereas many ^{4}He nuclei may occupy the same quantum state, ^{3}He nuclei are subject to an exclusion principle, and this results in markedly different behaviour at low temperatures.

The useful differences in cooling terms between the isotopes of helium are these. ^{3}He has a boiling point of 3.2 K, 0.8 K less than that of ^{4}He, but this improvement is too small to make it economically useful. However, when ^{3}He is pumped on, its boiling point comes down to about 0.3 K, and it is useful for obtaining temperatures this low.

5.3 Magnetic Refrigeration

5.3.1 Adiabatic Demagnetisation of a Paramagnetic Salt

Adiabatic demagnetisation requires a material which is ideally paramagnetic over the temperature range of interest, so that electronic magnetic moments will line up with an externally applied magnetic field. These moments are subject to very weak restraining forces, and so at room temperature are free.

At lower temperatures, the thermal energy k_BT becomes less, and is comparable to the energy of restraint, decreasing spatial freedom. At this point the dipoles

become ordered, and the entropy of the system is reduced. Entropy can be further lowered by the application of an external magnetic field. The restriction in the degree of freedom of movement of the dipoles causes a rise in vibrational energy, temperature, and a cold heat sink is used to bleed off thermal energy.

Subsequently, when the magnetic field is reduced, the degree of freedom of the dipoles is increased, and the temperature of the salt is reduced.

5.3.1.1 Principle of Operation

The two methods of operation for an ADR are shown in Figure 5.1 and Figure 5.2, where temperature T is the ordinate, and entropy S the abscissa.

Initially the system is at point **A**, where the pill has been cooled to the initial temperature of the cycle, and no magnetic field has yet been applied.

A strong magnetic field is then applied to the salt whilst it is still in thermal contact with the heat bath which keeps it at the temperature T_i. In both figures point **B** represents this situation. Thermal contact with the cold sink is then disconnected by means of a heat switch.

If the field is brought to zero immediately, then the increase in the degree of freedom of the ions, and the redistribution of energy results in a drop in temperature to point **C** on Figure 5.1. Heat leakage inwards from the environment results in the temperature moving up the $H = 0$ line.

If, alternatively, the field is only partially removed, then the state of the system will move to point **C** on Figure 5.2. If the magnetic field is carefully reduced to compensate for heat inflow from the environment, then the low temperature T_f can be maintained until the system reaches point **D**, and proceeds along the $H = 0$ line to point **A**.

The difference between the two methods is two-fold. Using the total demagnetisation method, a lower initial temperature is reached, but it is not constant. The area between the S-axis and the **C-A** or **C-D-A** line is a measure of the amount of energy the salt pill is absorbing, and it can be seen that the further away from the

S-axis point C is, the longer it will take a constant flow of energy into the system to move the temperature up. Hence working in isothermal mode, it is possible to keep below a desired temperature for longer compared with standard operation. For an ADR supporting a bolometer, or any device with temperature-dependent characteristics, the isothermal mode is the normal method employed.

The magnetisation energy generated in the salt pill when the magnetic field is applied is given by the area between the **A-B** line and the S-axis, and in the cases here does not affect the cycle since this energy is transferred from the pill to the heat bath as it is generated in the first **A-B** stage on the cycle.

5.3.1.2 System Description

The conventional mechanical arrangement for an ADR is to have a salt pill at the center of a powerful magnet, powerful here being of the order of 10 tesla. The strength of the magnetic field must be variable in order that the above described gradual demagnetisation process is possible. These two requirements usually mean that the magnet is an electromagnet, although the work of Leupold and Potenziani[1] suggests that a permanent magnet might be built with the required strength. The problem with such a device would be achieving the variability of field strength, and this is addressed more fully in the Chapters 6 and 7, where I consider the design of a space-based refrigerator.

Connected to the salt pill via a thermal switch is the cold bath. In the case of a helium-backed ADR this would be a pumped helium bath. Various designs for heat switches exist, but the two main types are gas-operated and mechanical. In the gas type, a small cavity is filled with a thermally conductive gas, which is absorbed into a charcoal nugget. This nugget can be heated by a small electrical coil to release the gas, and hence close the switch.

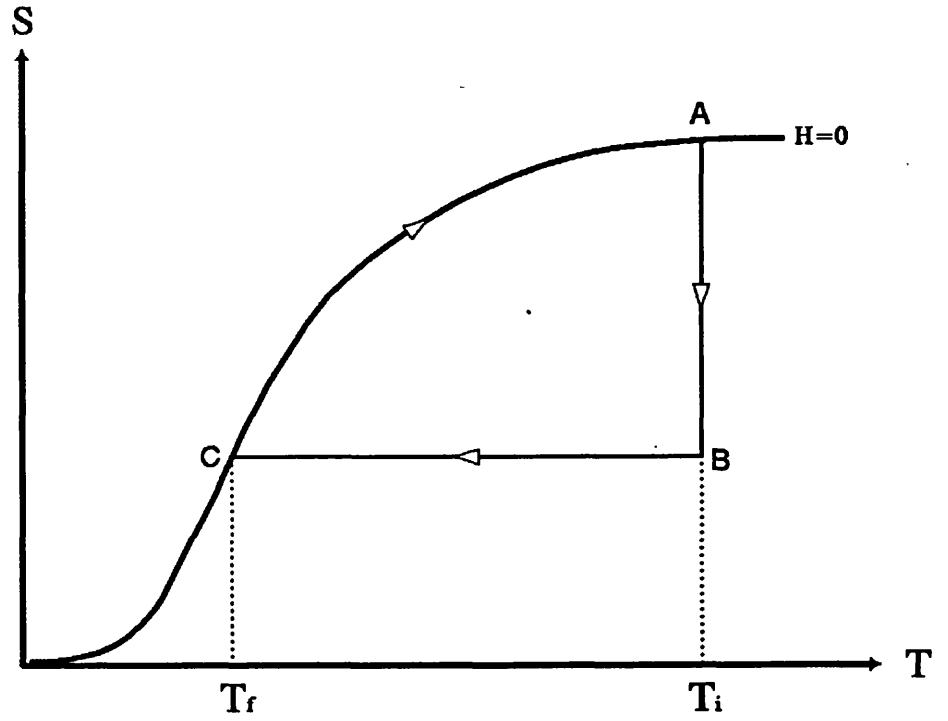

Figure 5.1: *Standard Operation of an ADR*

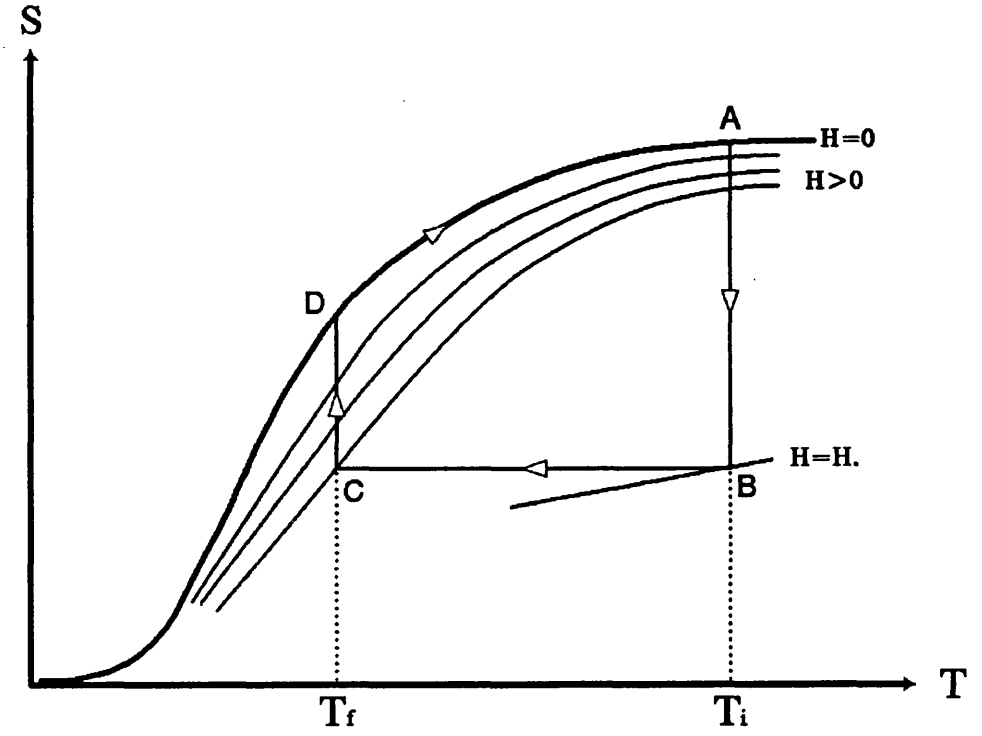

Figure 5.2: *Isothermal Operation of an ADR*

5.3.2 Nuclear Demagnetisation

Nuclear demagnetisation as a refrigeration technique uses the same basic concept as the above-described technique, except that where in the salt case the electronic magnetic moments are manipulated, in this case the change in the moment of the atomic nucleus is used. To this end the material copper serves as the active pill. Because nuclear magnetic moments are much smaller than electronic moments, this technique is useful chiefly in the temperature region below 1 mK, and is not of significant interest to the field of microcalorimetry.

5.4 Helium Dilution Refrigeration

In helium dilution refrigerators, cooling is produced by having a mixture of ^{3}He and ^{4}He, and cooling it to below the tricritical point at 0.7 K, where the mixtures exists in two different phases, one on top of the other - a ^{3}He-rich 'concentrated' phase, and a ^{4}He-rich, ^{3}He-poor 'diluted' phase.

In the ^{3}He poor phase the ^{3}He concentration tends towards a constant 6 % at absolute zero. ^{3}He is pumped from the ^{3}He-rich phase to the ^{4}He-rich phase. The helium from the ^{3}He-poor phase was in a more dispersed, lower energy state, so cooling is produced as the helium is 'diluted' on crossing the phase boundary.

5.5 Mechanical Cooling

Whilst previous cooling in space has been reliant on expendable cryogens, our aim here is to design a system limited not by the supply of such, but by mechanical reliability, since this form of system should yield not only an improved lifetime, but a far more compact system.

Bradshaw and Orlowska of the *Rutherford Appleton Laboratory* (*RAL*) have, over the last few years, been developing a cooling system appropriate to a space environment, able to provide a 4.0 K platform, with an high temperature end at

20 K[2]. The system consists of two Joule-Thomson compressors in series expanding high pressure gas below its inversion temperature isenthalpically. In the specific case of the *RAL* system, this gas has been helium expanding from a pressure of 10 bar to 1 bar.

Whilst the details of operation of the system are outside the purview of this document, it is worth noting the results of the system tests. When operated at a temperature of 4.17 K, the system was capable of extracting 1.5 mW, whilst the compressor consumed 126 W. It was expected that in the future it should be possible to extract 5 mW at 4 K, with power input of under 150 W, and these parameters are applied as part of the hypothetical refrigeration system described in Chapter 7.

5.6 The *Cochise* ADR experimental set up

5.6.1 General Description of System

The system being used by the *University of London* collaboration team for the X-ray calorimetry system studies is an adiabatic demagnetisation refrigerator (ADR) as described earlier, designed and constructed by the American company *Cochise*. A simplified cutaway schematic of it is shown in Figure 5.3.

5.6.1.1 The Salt Pill

The salt pill shown at the center of the device is composed of Chromic Potassium Alum (chemical structure $CrK(SO_4)_2.12H_2O$). This material is effective at bringing the system temperature down from 1.5 K to 100 mK. The lowest recorded temperature achieved in the total demagnetisation method described above is 58 mK, this being the lowest temperature recordable by the thermometer used at the time.

The salt pill is connected to the helium chamber on the lower side by a Kevlar (polyaramid fibre) foot (not shown). A copper rod is embedded in the upper

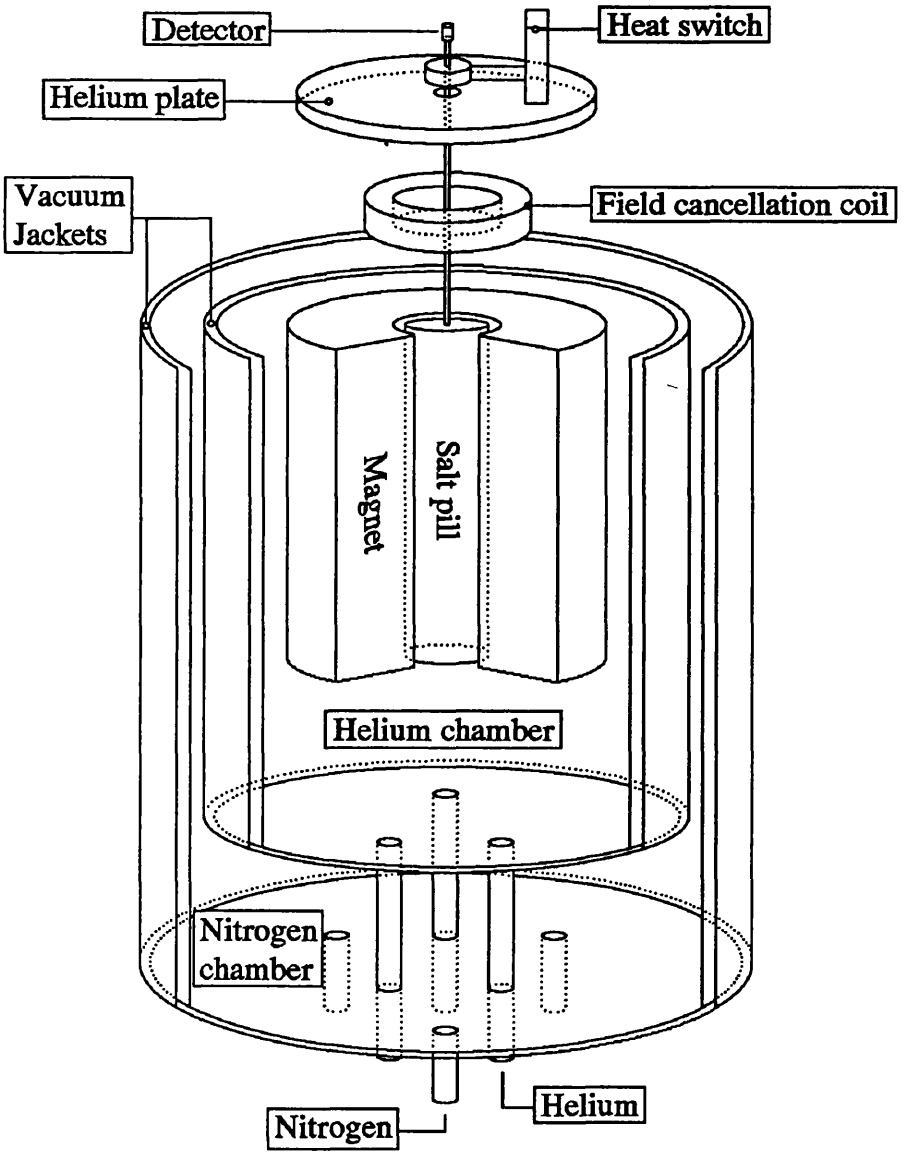

Figure 5.3: *Cutaway schematic of Cochise ADR*

portion of the salt pill, and goes upwards connecting directly to the detector housing above the helium plate. The end of the rod embedded in the pill also has a number of copper wires attached to it, which are spread throughout the pill in order to ensure a good thermal contact. A heat switch provides connection to the helium bath via the helium plate. This switch is mechanical in design, and is operated by a 12 volt solenoid.

5.6.1.2 The Superconducting Electromagnet

The electromagnet sits around the salt pill, sealed into the helium bath. The electromagnet is superconducting at liquid helium temperature, and hence dissipates a negligible Joule heating when operating. The magnet uses 30 amps to operate, and generates a maximum field strength inside the bore of 6 tesla. A persistent switch is present within the magnet, to break the continuity when loading the magnet with current, and draining it. This switch consists of a coil of wire around part of the magnet coil. The switch coil heats up the magnet coil, driving it above the critical temperature, and impeding electrical conduction. Electrical contacts either side of the switch are then able to drive a suitable current through the magnet.

A field cancellation coil operates above the main magnet. The purpose of this is to attempt to reduce the magnetic field present in the small volume occupied by the detector, and minimize any effect on the semiconductor.

5.6.1.3 The Helium Chamber (Can)

The helium can has a capacity of approximately 7 litres, and is fed by three tubes running through the nitrogen chamber, which are also used to take the power supply cables for the magnet, and a small tube which takes liquid helium directly to the bottom of the can, reducing loss through contact with 'warm' gas.

Between the helium layer and the nitrogen is an evacuated layer, which also contains a thermal jacket composed of 8 alternating layers of aluminised mylar and bridal veil. Aluminised mylar is used for the outside surfaces.

5.6.2 Description of Operation

The ADR operated by the *University of London* collaboration, supplied by *Cochise Inc* is a device which brings the temperature of the salt pill, and though conductive contact, the detector stage, down to a temperature of 100 mK. This it does with a combination of cryogenic liquid layers separated by insulating layers, and the ADR set-up inside the helium layer.

Firstly the entire cryostat is cooled to the boiling temperature of nitrogen, 77 K, by pouring nitrogen into both the helium and nitrogen chamber of the ADR. Once the nitrogen has stopped boiling off, then the apparatus has reached thermal equilibrium with the liquid, and it is below 77 K. The nitrogen liquid is then removed from the helium cavity either by blowing it out with compressed air, or by inverting the cryostat. Liquid helium is then used to fill the helium chamber (or can). The transfer method is somewhat more involved than for nitrogen because of the lower boiling point of helium, and the somewhat higher cost. Briefly, a narrow transfer tube is used between the dewar and the ADR, which is cooled by the passage of helium before liquid transfer can begin. At the ADR end the helium supply pipe feeds directly into a funnel which brings the liquid directly to the bottom of the can, hence avoiding losing energy to the air.

Once the helium can is filled, the vapour pressure above it is brought down as low as possible, in our case down to 10 millibar. This has the effect of bringing its boiling point down to 1.5 K, and consequently about 30 % of the liquid helium is boiled off during this pressure drop.

Now the ADR process discussed in Section 5.3.1.1 can begin. The 1.5 K helium bath is used as both cooling for the superconducting electromagnet and as the low temperature sink. The salt pill is magnetised using the persistent switch to feed 30 amps into the magnet. The subsequent rise in temperature of the pill is then neutralised by using the heat switch to bring the pill into thermal contact with the helium bath. Once the pill temperature has returned to a temperature of 1.5 K, the thermal contact is removed again, and the persistent switch can be used to reduce the magnetic field , and reduce the temperature. Currently

a computer can be used to control the demagnetisation, and keep as constant a temperature as possible.

In a typical run, the magnet and power supply would be controlled to maintain a temperature of 100 mK for as long as possible, hence the gradual demagnetisation technique described in Section 5.3.1.1 is used. To calibrate thermometers, however, the total demagnetisation method can be used.

The greatest limit on the lifetime of the helium in the helium can is the persistent switch. To operate, it makes a small section of the superconducting magnet normal (in the conduction sense), which causes some Joule heating through the helium, and hence accelerates boil-off.

5.6.3 Thermal Model of System

In order to better understand the flow of heat throughout the ADR, and to gain familiarity with the thermal modelling software ESATAN, a thermal model of the *Cochise* ADR was constructed and run.

For the purposes of the thermal model, only the system from the helium level inwards is considered, and it is represented in Figure 5.4 and Table 5.1. The helium is assumed to be a thermal boundary, unchanging in temperature. External to this is 'The World', which because of the internal environment of the ADR is assumed to be at 77 K. The representation of the ADR in the model is largely based on the original blueprints supplied by *Cochise*.

Each of the nodes has a number and an associated ID. The number is just to differentiate between the nodes, whereas the ID consists of the number plus a prefix to determine whether the node is a boundary or dynamic (B or D).

5.6.3.1 Node 1 - The Detector

The detector is usually a small piece of germanium. For the model it is assumed to be a 0.3 mm cube, and is bonded strongly to Node 2, the detector mount.

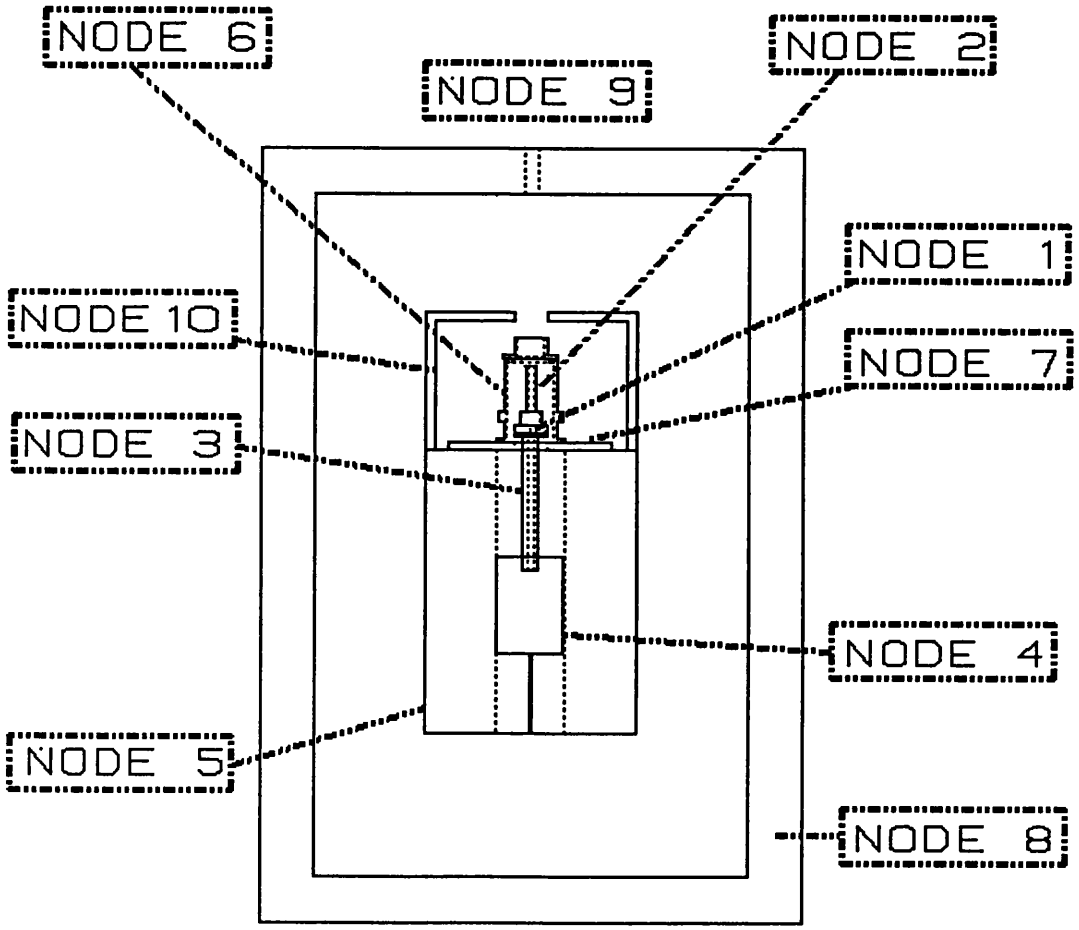

Figure 5.4: *Thermal model of Cochise ADR*

Physical Data on Nodes					
Node			Material	Volume (m^3)	Mass (kg)
No.	Name	ID			
1	Detector	D1	Ge	2.70×10^{-11}	1.45×10^{-7}
2	Detector Mount	D2	Cu	3.07×10^{-6}	0.0274
3	Detector Stage	D3	Cu	1.12×10^{-5}	0.100
4	Salt pill	D4	CPA [1]	1.42×10^{-4}	0.260
5	Helium jacket	B5	-	-	-
6	Helium shield	D6	Cu	2.86×10^{-5}	0.255
7	Helium plate	D7	Cu	6.49×10^{-5}	0.579
8	World	B8	-	-	-
9	Source	B9	-	-	-
10	Outer He Shield	D10	Al	0.000126	0.340

Table 5.1: *Thermal model of Cochise ADR*

5.6.3.2 Node 2 - The Detector Mount

This is a construct to hold the detector, Node 1. It is geometrically equivalent to three concentric hollow copper tubes of different diameters and lengths, attached end-to-end, and closed at the ends. The widest part has a diameter of 25 mm, length 8 mm. The tube attached to this has a diameter of 16 mm, length 11.5 mm, and the final part has a diameter of 7 mm, length 40 mm. At the narrow end a 0.25 mm aperture allows the detector sample to view the source. At its wider end this node bolts onto Node 3, the detector stage.

The stage is connected to the inner helium shield, Node 6, by means of three kevlar rods, of diameter 2 mm, length 13 mm.

5.6.3.3 Node 3 - The Detector Stage

This is a copper rod, diameter 12 mm, length 119 mm, of which 13 mm are embedded inside the salt pill, node 4. At the other end, the rod widens out to a diameter of 25 mm for its end 3 mm of length. The rod is hollowed out to a diameter of 5 mm for most of its length, and has cuts made in it to reduce the occurrence of eddy currents. A number of copper wires connect to the embedded end of the stage throughout the pill to ensure good thermal contact.

At its wider end it is bolted to the detector mount, Node 2.

5.6.3.4 Node 4 - The Salt Pill

The salt pill is a plastic tube, 48 mm in diameter, 85 mm in length, containing a compound of Chromic Potassium Alum ($CrK(SO_4)_2.12H_2O$).

The salt pill is assumed to be a thermal boundary at 100 mK.

On one end it has a mount for the salt pill foot, and in the other end the detector stage is embedded for 13 mm.

5.6.3.5 *Node 5 - The Helium Jacket*

For the purposes of the model, the helium jacket is a cylinder, outer diameter 155 mm, inner diameter 50 mm, length 250 mm, which is closed at one end, where the salt pill contacts it. The pill foot is a kevlar rod 2 mm in diameter, 70 mm in length.

The jacket is represented in the model as a thermal boundary, and hence is held at a constant temperature of 1.5 K.

5.6.3.6 *Node 6 - The Inner Helium Shield*

This is a cylinder of inner diameter 34 mm, outer diameter 38 mm, length 74 mm. At one end it has a lip for 3 mm of its length, where the outer diameter is 50 mm, and there is a bulge in the tube centered 22 mm from this end, where the outer diameter increases to 48 mm for a length of 8 mm. At the other end, a cap fits onto the main body, which attaches a tube of length 14 mm inner diameter 20 mm, outer diameter 24 mm to the shield.

The inner helium shield bolts onto the helium plate. Inside the shield is the detector mount, to which it is attached by three polyaramid rods. The rods are epoxied into copper threaded cylinders, which are mounted in threaded openings in the shield bulge. This support structure is under modification to a kevlar tension support structure.

5.6.3.7 *Node 7 - The Helium Plate*

The helium plate is a copper disc of diameter 120 mm, thickness 6 mm, which has a hole through its center of diameter 25 mm, through which the detector stage protrudes. A number of holes, threaded and blank, are bored through the plate for the mounting of the heat switch, the bias resistor, and the pre-amplification system.

The helium plate is bolted to the helium jacket, Node 5.

5.6.3.8 Node 8 - The World

'The World' is the region surrounding the rest of the nodes, except for the source, and is held at 77 K, to represent the nitrogen layer.

5.6.3.9 Node 9 - The Source

The source is the ^{55}Fe radiation source which is held in the source holder bolted onto the end of the cryostat. It is viewed through a small hole in the cryostat, and is treated as a boundary node at room temperature.

5.6.3.10 Node 10 - Outer Helium Shield

The outer helium shield is a cylinder which attaches to the top of the helium jacket, and is topped by a disc with an aperture through it.

5.6.3.11 Modelling

For the model it was necessary to calculate view factors between each node and each of the others. This factor was based solely on the geometry of the arrangement. From this the software can determine, based on the temperature of any two nodes, the net radiative transfer between the nodes. To allow the program to simulate the thermal conduction between nodes, it was necessary to calculate the thermal conductance between each of the nodes.

By assuming thermal equilibrium, it is possible to inspect the heat flow between the nodes. The most important result from the model is the parasitic heat input to the salt pill. The majority of this is due to thermal conduction from the helium jacket and the detector mount, and totals 0.008 mW.

Using partial demagnetisation to obtain a constant temperature of 100 mK, the pill can absorb approximately 0.468 J, which makes a hold-time of just over 16 hours. In practice, operation of the ADR provides a hold-time of 8 hours

at 100 mK. This suggests that the whole of the salt pill is not participating in the ADR process.

The ADR has been tested by monitoring the warm-up curve, and observations suggest that there is a distinct thermal buffer between the salt pill and the detector stage. The thermal contact is less than ideal, and hence when the stage is at 100 mK the pill may be at 80 mK. This would go some of the way to explaining the low hold time observed.

5.6.4 A Higher Temperature Salt Pill

Further to this low temperature work, and as a consequence of the consideration in Chapter 7 of the possibility of an intermediate temperature ADR, it was considered that the possibility of using Gadolinium Gallium Garnet (GGG) as a salt pill might be investigated. Although this has been considered a viable possibility previously[4], there has to date been no experiment that demonstrates GGG in an ADR.

5.6.4.1 Initial GGG Preparation

As obtained the GGG crystals were obtained as approximately 100 crystals making up a total mass of 100 g. These crystals were ground down to an estimated grain size of between 10 and 50 μm over a period of one week. The resultant powder was removed from the grinding equipment by washing off with chloroform. The chloroform was subsequently removed by drying the powder in a dried vacuum oven.

5.6.4.2 Pill Preparation

The next stage will be the preparation of a G10 fibre-glass tube to contain the pill. At one end of this tube will be the detector stage, a copper rod which will also plug the end of the tube. Soldered to the end of the stage protruding into the pill will be approximately 100 copper wires, which will be strewn throughout

the pill, so that thermal contact will be maintained between the pill and the stage when the pill contents are inserted. The detector stage is inserted into the pill, and secured by Stycast 2850 FT epoxy. The tube is then filled, though its open end, with the GGG. A 10 ton press will then be used to compress the GGG. Subsequently the Stycast epoxy will be used to seal the open end of the pill.

5.6.4.3 *Pill Testing*

The testing system envisaged for the GGG pill is this. The pill will be mounted in the *Cochise* ADR in place of the CPA pill which has been used to date. The pill will then be tested at a starting temperature of 4 K by filling the helium can of the ADR with ^{4}He. The magnet will then be controlled to obtain a temperature of 1.5 K, and the hold time at that temperature observed. The pill will then be tested at a starting temperature of 1.5 K by pumping on the ^{4}He. Full demagnetisation will be used to determine the cooling energy available.

Bibliography

[1] *Novel High-field Permanent-Magnet Flux Sources* - H.A. Leupold, E. Potenziani II, IEEE Trans. Magnetics Vol. MAG-23, No.5 pp.3628-3629, September 1987

[2] *A Closed Cycle 4 K Mechanical Cooler for Space Applications* - T.W. Bradshaw, A.H. Orlowska, Proceedings of the 4th European Symposium on Space Environmental and Control Systems, Florence 21-24 October, 1991, ESA Sp-324, pp.397-401

[3] *Principles and Application of Magnetic Cooling* - R.P. Hudson, North-Holland Publishing Company, 1972, ISBN 0 7204 1257 9

[4] *Materials for magnetic refrigeration between 2 K and 20 K* - J.A. Barclay, W.A. Steyert, Cryogenics, February 1982, pp.73

Chapter 6

Space Application

6.1 The Need for a Spaceborne Platform

The aim of this investigation is to determine a suitable means for deploying an X-ray microcalorimeter to obtain observational information on X-ray sources in space. To this end, the observation point must have an unrestricted view of space in the X-ray region. The attenuation of electromagnetic radiation in the Earth's atmosphere is well documented[1], and it is clear that in order to observe in the X-ray region (10^3 to 10^6 eV), and more acutely in the soft X-ray region (10^2 to 10^3 eV), it will be necessary to observe from a point at least 100 km above the Earth's surface, and preferably 200 km for the soft X-ray region.

6.2 Means of Attaining a Space Platform

6.2.1 Balloon

The balloon is an inexpensive option in comparison to other systems, costing approximately £ 1M for a day of observing time, with a lead time as low as two

years. Although the payload is recoverable, the maximum altitude obtainable with a balloon is only 30 km, which makes it unusable in X-ray applications, except for observation of the very highest energy X-rays, in which energy regime atmospheric attenuation will still block 50 % to 90 % of X-rays. The only application for balloons currently are as gamma-ray observatories.

6.2.2 Sounding Rocket

A sounding rocket mission has approximately the same cost as a balloon, and is able to attain an altitude of 150 km. However, it requires three years lead time, and has an observing time of only 15 minutes. With a rocket, it is usually possible to retrieve the payload, however there is no guarantee that it will have survived the return trip intact. Rockets were an important tool in the early days of X-ray observation, but are used very little currently.

6.2.3 Space Station

Using a long-term Earth-orbiting space station as an observing platform has the advantages of easy access by the station crew, for a possible reduction in the extent of automation required on the device. It would also be useful should any unforeseen eventualities occur with the device to have humans available to deal with them. Unfortunately, having humans in close proximity to the device will mean that safety will have to be considered in the design, and device efficiency may have to be compromised to this end. A station environment is also a very poor background for an experiment; onboard systems may interfere with it, the option to point the detector may well be limited, and the orbit adopted is unlikely to be ideal.

6.2.4 Recoverable Module

One possibility would be a module launched from the Space Shuttle on one mission, placed in suitable orbit, and recovered at a later date on a subsequent Shuttle

mission, as intended for *Eureka.* The advantages of such modules is that their recoverability allows for diagnostics on the post-flight instruments, and possible re-flight. In addition, the development of interface standards is unnecessary.

However, the necessity of launching the module from the Shuttle bay means that the shuttle orbit will define that of the module, and is unlikely to be ideal. As with all shuttle-based operations human safety is a paramount consideration, and poses some limitations on design. Also the size of the shuttle bay and mass restrictions apply. Duration of such missions is usually only 6 months, although there are some notable exceptions, such as the *Long Duration Exposure Facility* (*LDEF*).

6.2.5 Space Shuttle Short-term Module

Systems such as *SPAS* (Shuttle **PA**llet **S**atellite), and the more recent *AstroSPAS* have come to prominence in the last ten years, and the use of such a system has advantages in this application. A *SPAS* platform is launched into space from the US Space Shuttle, and remains in free flight up to 120 km from the Shuttle for between 4 and 8 days. It is then retrieved into the Shuttle, and returned to the Earth. Telemetry for the platform is handled via a Shuttle relay to the *Kennedy Space Centre* ground station, whereas data is stored on magnetic tape on board the Shuttle.

This system will be very useful for the development of instruments, but will not have an ideal orbit since it will have to be close to the Shuttle. To enable as many detectors as possible to fly, it is likely that a number of instruments will be operated on the same platform, at the cost of them being of modest size, and the other instruments on board are likely to create a less than ideal environment. Safety is a high consideration for this platform, since the deployment of the *SPAS* unit and shuttle operation will still, in the forseeable future, be handled by humans.

Although mission time in orbit will be at least 4 days, it is likely that actual observing time will be much less than this.

6.2.6 Free-flying Satellite

The most popular choice for a space-borne instrument is that of a satellite mission. A typical operating life for a satellite mission such as for example *ROSAT* is a launch by rocket into Earth orbit, followed by an observation period of some years until systems failure, often after outliving their nominal lifetime.

There are a number of advantages over the other systems described above, not least of which is the possibility to select the most ideal orbit for the mission, which I discuss in greater detail below. Since there is no involvement by humans in any aspect of the mission from launch until systems failure, there are very few safety limitations. Because the satellite is being designed around the instruments, rather than being fitted into a Shuttle bay, restrictions on mass and size can be better tailored. Unlike a shuttle module, or a space-station instrument, the satellite is completely dedicated to its mission, and can therefore obtain the maximum observing time, and have control and data transfer systems optimised to its needs.

Once a satellite has left the launch-pad, it is very hard to repair or recover it. All maneuvering into orbit and mechanical operations such as opening solar panels must be done automatically. Should anything go wrong, it is unlikely that a human team could be mobilised to correct the failure, even if economically viable. Notable exceptions to this rule include the *Solar Maximum Mission* (*SMM*), and the *Hubble Space Telescope* (*HST*). Since satellite development is an expensive process with a long lead-time, very strict standards must therefore be adopted to reduce the probability of such a failure. In this respect, instruments flown on satellites are more usually those with a high reliability that can be operated for long periods with high stability.

6.3 Choice of Orbit

Assuming that one of the Earth-orbiting possibilities is chosen as a platform, there are a number of classes of orbits that might be considered.

6.3.1 Geostationary Orbit

Although a geostationary orbit is well above the atmosphere at 36000 km, it does, because it is equatorial, pass through the radiation belts, and is totally unsuitable for X-ray missions because of the large induced particle background.

6.3.2 Low Earth Orbit (LEO)

At an altitude in the 400 km to 500 km range, a low Earth orbit with near-zero inclination only slightly touches the radiation belt. A large inclination orbit will pass through the cusps of the radiation belt, and so will cause a variation in particle flux. LEOs are protected from solar particles by the Magnetosphere.

LEO period is approximately 65 minutes, which sets an upper limit for uninterrupted viewing time of any one source. Since the microcalorimeter is envisioned to be most useful as a faint source spectrometer, this would mean that to observe a source for greater than this orbital time will necessitate breaking up observation time, and realigning the detector accurately at the start of each session.

In addition, atmospheric drag causes the orbit to decay, putting a finite lifetime on any mission unless boost motors are employed, with the attendant mass cost. An alternative to this is that used by the massive *HST*, which has an altitude of only 300 km, but if necessary will be pulled up by the Shuttle to counter atmospheric drag.

6.3.3 Highly Eccentric Orbit (HEO)

This is an orbit with a perigee of the order of 10000 km, an apogee of over 100000 km, and a high inclination. The high eccentricity and altitude mean that the orbital period is a few days, which allows for longer periods of uninterrupted viewing. The low relative speed also allows one ground station to control the platforms systems, and data to be sent to the station in real time. For a prototype system like the ADR, it will be very advantageous to be able to continuously

monitor the system.

Background particle flux is significantly (by a factor of 10) higher than in an LEO, however the level is more stable. Since the apogee is only about a quarter of that of the moon, the pull of the Moon and Sun cause HEOs to be inherently unstable, resulting in variation in perigee, and eventual re-entry.

6.4 Considerations for a Space-based refrigerator

Assuming an X-ray microcalorimeter were to operate in either a satellite or *SPAS* environment, there are a number of matters to consider which are unimportant in an laboratory-bound environment.

6.4.1 Size

It must be small, chiefly because of the limitations inherent in the cost of putting a large instrument up. The bulkiest part of the instrument by far, excluding the electronic support, will be the refrigeration system, and it is to this which we apply our attention. An *ESA* report[2] suggests a volume of 180 mm by 75 mm by 75 mm. In the *AXAF* project, however, a vast tank of liquid helium is used to back up the refrigeration system. The two-stage ADR described in Section 7 is a compromise in size between these two extremes, and if feasible is a preferable option to putting helium tanks into orbit.

6.4.2 Mass

For the same reasons as those above, the package must be lightweight. In this case the magnets of both stages will be the limiting factor. The *ESA* report quotes an acceptable mass as being in the range of 2 kg plus electronics. This is where the two-stage ADR approach adopted here has advantages over the *AXAF* helium tank option. A problem in this area may also be the power supply unit required.

A superconducting electromagnet will require a to must supply 10 amps, which is a high power supply requirement. A device needs to be designed capable of supplying, storing, and draining a 10 amp current from the magnet with high efficiency, and this will clearly be non-trivial.

6.4.3 Ambient Magnetic Field Strength

Considering that there will be two fairly high strength magnets involved in the construction of the refrigerator, it is important to ensure that the field strength external to the detector is kept within acceptable limits. Spacecraft instrument subsystems and magnetometers used for attitude control can be highly susceptible to residual magnetic fields, and it is also necessary to ensure that no torque results on the spacecraft, due to the interaction of the dipole moment of the refrigerator and the Earth's magnetic field. A more detailed discussion of the requirements and techniques of shielding are to be found in [3]. What might be added to what is discussed there is the nature of the magnetic fields used here. The design of a permanent magnet as discussed by Leupold and Potenziani[4] means that the vast majority of magnetic flux passes perpendicular to its axis. This makes it not only a highly efficient device, but also a very low source of external flux. The same cannot be said of superconducting electromagnets (SCMs). Although a strong source of flux, the SCM flux lines pass along the axis of the magnet, and hence cause a strong magnetic field outside it. Conventionally, this magnetic field is countered by the use of cancellation coils. A system of one coil close to the magnet end to reduce the overall magnetic field, and a pair of coils either side of the area which is most sensitive to fields is the most modern technique used by magnet designers, and may well reduce the field strength to within more tolerable levels.

6.4.4 Control Instrumentation

In order that a reliable refrigerator be put up, control systems must be designed and tested to allow close monitoring of the cooling device at all times. Two parallel systems will be required, both with independent access to all systems, so that should one fail, the redundant system will be able to take over from the faulty one without problems.

6.4.5 Reliability

Extreme reliability is required of the system. One would expect of the design that it should operate for some weeks without supervision, since the repair of spaceborne packages is at worst impossible, or at best prohibitively expensive. A *SPAS* or space station platform will mean that some maintenance is possible, however the extent of this will be severely limited, and should not be relied upon.

6.4.6 Hardiness

The device must be sturdy enough to withstand the large accelerations, vibrations, and temperatures experienced during a launch. This may well be a problem with the salt, since Chromic Potassium Alum (CPA) decomposes at temperatures over 89 celsius, and Ferric Ammonium Alum (FAA) has an even lower decomposition temperature, 40 celsius. In addition, there are reports[5] that FAA is highly corrosive to the extent of corroding embedded electrical leads. In fact, both of the salts are corrosive, however, adequate hermetic sealing, care in bakeout, and other protective measures should ensure that whichever salt is chosen should be able to survive the process. In fact, a CPA salt pill survived a simulated two week bake-out[6] at 50 celsius.

Also, the mounting of the salt pill inside the magnet must be by a means that will have a low conductivity to the surroundings, but strong enough withstand the launch, which may be a situation for compromise. Currently, Kevlar wires are

used, and would appear to be a suitable material for the space device described later due to its strength (bullet-proof clothing is woven from Kevlar), and low thermal conductivity. In Section 6.6.1.2 I discuss a suitable means for securing the parts of the system with the minimum heat transfer.

6.4.7 Long-duration Stability

It must be able to operate continuously over a period of months to years without mechanical service or replenishment of cryogens. This will be an overriding consideration in any system which operates continuously at as low a temperature as a microcalorimeter will have to. The *Infra-red Space Observer* (*ISO*) solution to this is to be to take up as much helium as possible for the mission with the device, in this case 10000 litres. This is clearly a basic solution, even incorporating the low-loss containment involved in the storage. A more stable solution to this may be that refrigerator described later in this section, where a 4 K mechanical cooler as discussed in Chapter 5, and described in [7] takes the place of the cryogen. It may well be necessary to also use a quantity of liquid helium, but this will be to ensure the adequate transfer of heat around the system, rather analogous to the role of engine oil. In this design the helium would be inside a sealed system, kept below its boiling temperature by the mechanical cooler.

6.4.8 Zero-gravity Environment

In addition, the refrigerator must be able to operate in a zero-gravity environment. This should not be a problem with a magnetic refrigerator such as the two-stage device described later, but the absence of a net gravitational force does make the design of dilution refrigerators more problematic. Although efforts have been made in this direction, particularly with regard to the use of such a device on *AXAF*, little progress seems to have been made, and the *AXAF* group now seem to have returned to the use of an ADR[8],[9] .

6.5 The Use of Helium Dilution Refrigeration in Space

The chief problem with operating a helium dilution refrigerator in space is the effective lack of gravity. In ground-based systems the force of gravity is used to keep the liquid components of the refrigerator in their respective chambers, and to keep ^{3}He above ^{4}He in the mixing chamber. For a convincing ground-based test, one needs to operate it the right way up, and inverted in order to confirm its gravity independence.

A number of possibilities for compensating for this lack of gravity have been suggested. In one, a porous material confines the liquid in the chambers where only one form of helium exists, and a similar material confines ^{4}He adjacent to the wall of the mixing chamber, with ^{3}He in the center. An alternative solution uses a high electric field for confinement. Unfortunately the forces involved are much less than gravitational force at the Earth's surface, so that ground-based testing will be impossible.

Against the case for dilution refrigeration in space are

- The necessity of proving the reliable operation of a suitable device in space.
- The complexity of the required control system.

In favour of such a system are

- The low mass of the device. No magnets are required for a dilution system, and this is the chief mass problem with the ADR.
- The system also interferes less with the environment than an equivalent ADR in terms of stray magnetism as a consequence.
- Low output power. Less than 1 mW of power should be produced at 2 K by a dilution refrigerator drawing about 3 μW of cooling power at 100 mK. This makes the cooling requirement on a second cooling stage less critical.

6.6 The Use of an ADR in Space

Adiabatic demagnetisation refrigeration is a technology with no reliance on gravitational force in its ground-based form. This therefore makes it a favourable candidate for conversion to a space-worthy device. The main difference between the operation of this and a ground-based device will be the replenishment of cryogenic fluids, easily achieved in a laboratory.

6.6.1 Support Structures

6.6.1.1 General Considerations

In order to determine the suitability of Kevlar threads over more rigid supports, it is necessary to compare the Kevlar solution with the alternatives, with regard to thermal and mechanical considerations.

The need for supports of low thermal conductivity precludes a large variety of materials from this purpose. Thermal conductivity data for any material at temperatures as low as 1 K is not generally available, however it is possible to compare materials at a temperature of 4 K, and it is possible to discount all metals. A number of materials have been used in the laboratory for mounting detectors in cryostats, and for separating the layers of cryostats. In [10], a number of materials are considered, including Torlon and Vespel, the former of which we have used in the ground-based ADR as a support for the detector stage. Both of these materials are stiff solids, and so would be used as struts, under compression rather than tension. Consequently another form of support would be required to hold the contact points of either end of the struts in place. Whilst the reference shows that solid struts are able to withstand launch vibration along their length, the bending stress would appear to be too great. In the analysis, however, all struts are parallel, and it is worth considering that holding a central mass in place with six struts aligned along any three orthogonal axes may obviate this problem somewhat. One problem that may occur is the possibility of rotation. This is the only form of movement in which none of the struts will be in compression, and

hence there is no protection against any strut bending. Under launch conditions, however, it is very unlikely that any rotational vibration would occur.

6.6.1.2 Kevlar Thread Diameter Determination

The above arguments lead to the conclusion that a Kevlar thread supporting arrangement may well be suitable for mounting the salt pills. Assuming this is the case, it is necessary to determine the diameter of the thread necessary, since the inflow of heat to the salt pills will be highly dependent on this. For this case, I will determine the necessary diameter of kevlar wire to support a 0.1 kg salt pill or other mass, when six wires are used to support it, and a 20g vibrational force is applied to the mass.

Parameters:-

- M is the mass of the pill.
- a is the acceleration of the pill due to launch vibration.
- F is the force on the pill due to acceleration a.
- d is the diameter of the kevlar wire.
- Y is the Young Modulus for the wire.
- T_P is the pre-tensioning on each kevlar thread.
- T_F is the additional tension on each kevlar thread due to the force F on the pill.
- S_T is the tensile stress on each wire.
- S_B is the breaking stress of Kevlar thread, 2.76×10^9 Nm^{-2}

Three threads are attached to the upper edge of the cylindrical pill, and three to the lower edge, in positions and at angles that mean that the lines all pass

through the center of the pill orthogonally. This angle will probably have to compromised slightly due to the shape of the pill.

The launch vibration is chiefly in the direction of flight, however it is unknown in which orientation the refrigerator would be mounted in a launch vehicle. Arbitrarily, therefore, I assume that the launch is in the direction of the axis. This direction should not affect the result adversely, since a three-axis mounting such as this should be equally effective in all directions.

Since the acceleration of the mass a is 20g, and the mass of the pill is M, the force F is calculated as

$$F = Ma$$

The upper three threads are at 45°to the axis of symmetry. As a force F is applied upwards to the salt pill mass, the lower three threads are in tension, and the upper three threads are relaxed from their pre-tensioned level.

The additional tension placed on each of the threads is

$$T_F = \frac{F}{3cos(45°)} = \frac{\sqrt{2}F}{3}$$
$$= \frac{\sqrt{2}Ma}{3}$$

If instead we assume the worst case, that the acceleration is along the direction of one of the threads, and that thread must take all of the stress, then the additional tension on this thread is

$$T_F = Ma$$

We can set a limit on the maximum stress to be applied to the thread by stating that it will be equivalent to one-tenth of the breaking stress S_T. Stress is the result of dividing the tension by the cross-sectional area, so

$$\frac{T}{A} = \frac{S_T}{10}$$
$$\rightarrow \frac{4T}{\pi d^2} = \frac{S_T}{10}$$

$$\rightarrow T = \frac{S_T \pi d^2}{40}$$

Since the total tension T is the sum of the tension due to pre-stressing, and the tension due to the external force, we assume each of these to be approximately equal. ie. $T_F = T_S = \frac{T}{2}$ hence

$$\rightarrow 2T_F = \frac{S_T \pi d^2}{40}$$

$$\rightarrow T_F = \frac{S_T \pi d^2}{80}$$

We can equate this maximum permitted additional tension with the tension caused by the external force calculated above. Where acceleration is along the axis, we find

$$\frac{S_T \pi d^2}{80} = \frac{\sqrt{2} M a}{3}$$

$$\rightarrow d = \sqrt{\left(\frac{80\sqrt{2} M a}{3 \pi S_T}\right)}$$

and where the acceleration is in line with one of the threads, we obtain, similarly,

$$d = \sqrt{\left(\frac{80 M a}{\pi S_T}\right)}$$

This yields a required diameter 45 % greater than the previous case, and should therefore be used as the baseline.

Since $M = 0.1\,\mathrm{kg}$, $a = 20\mathrm{g} = 20 \times 9.81\,\mathrm{ms}^{-2} = 196.2 ms^{-2}$, and the breaking stress $S_T = 2.76 \times 10^9\,\mathrm{Nm}^{-2}$, the diameter of Kevlar thread required for this mass is 0.42 mm. We round this up to 0.5 mm, and note that this diameter increases proportionally with the square root of the mass of the pill.

6.6.2 Heat Switch Qualification

As briefly mentioned in the previous chapter, there are two possible designs of heat switch currently used in ground based systems. One of them uses the conductance of a gas inside a cavity to close the switch, the other depends on a direct conductive contact.

6.6.2.1 Gas Heat Switch

The gas heat switch consists of an enclosed cavity, which contains a small quantity of helium gas. Also inside the cavity is a small amount of activated charcoal. At the ambient temperature, the charcoal absorbs the helium into itself, and the switch is open. A small heater is attached to the charcoal, and when the switch is to be closed, the heater is activated, and the helium is released, filling the cavity, and completing the conduction path. This has the advantage that, if control of the switch is lost, it is most likely to be through a heater failure, and the switch fails in the open position. It is therefore possible to use two switches in parallel, with one able to stay open as a backup, which can be used in place of the main switch should it fail open. Another advantage of the gas heat switch is the simplicity, there are no moving parts, and only one simple electrical component. The heater is as simple as a length of wire wrapped around the charcoal, and hence is therefore very hardy. The most likely source of damage to such a switch is the distortion of the metal plates either side of the cavity to an extent that they touch, forcing the switch permanently closed, but this is a minor consideration compared to the mechanical failure possibilities of the mechanically operated heat switch.

The problem with the gas heat switch is that because of conduction through the gas-containing shell, switch conductivity is always non-zero. A typical gas heat switch conducts 20 mW in the closed case, and 10 μW in the open case, over a temperature gradient of about 4 K. This open conduction is undesirable in a system like an ADR where parasitic heat input will strongly affect hold time, particularly in a space-qualified application where two heat switches would operate in parallel, one as a redundant fail-safe.

6.6.2.2 Mechanical Heat Switch

The mechanical heat switch operates by bringing two highly conductive plates, usually metallic, together with some force. In the case of the heat switch in use on our ground-based system, one plate is sandwiched between two others, which

are brought together and clamp onto the central plate to close the switch. The outer plates are connected to one of the temperature regions, the inner plate connects to the other. The plates are brought together by a solenoid activated by a current. The motion of the solenoid is converted by levers to the direction of motion of the plates.

The advantage of this design of heat switch is its high on/off ratio. A typical switch will conduct 10 mW when closed, and effectively no power when open. In a system like an ADR where the heat influx to the salt pill determines the hold-time, a switch with a very low leakage is highly desirable.

The major problem with this form of heat switch is the complexity. The design of this switch will require mechanical elements to change the direction of movement of parts, in all probability hinges, potential points for failure. In addition, should the switch fail, it may fail either open or closed, making designing a failsafe system more difficult.

6.6.3 Choice of Magnet

In order to operate the ADR, it is necessary to provide a strong magnetic field around the salt pill. The device to supply this magnetic field could take two forms.

6.6.3.1 A Superconducting Electromagnet

A superconducting electromagnet (SCM) would have to be cooled by some means to a temperature of 4 K or less, unless a one that operates at a much higher temperature becomes available. Because of the large mass of such magnets, strong supports are required, and the temperature gradient across these supports will cause a significant parasitic heat loss. Current leads to supply the magnet would have to carry a few amps through the cold regions during recycling, producing Joule heating. Because of the solenoid configuration, a high external field remains at each end of the magnet, which would have to be reduced by cancellation coils in

order that the field does not interfere with the detector, the spacecraft systems, or any nearby equipment. The operation of the magnet requires a persistence switch and controller, with the ever-present danger of quenching.

However, this does make the possibility of high magnetic field strength available, and changing the field strength is a simple operation involving no moving parts.

6.6.3.2 *A Permanent Magnet*

Such magnets as described by Leupold and Potenziani II[4] would have significant advantages over electromagnets in an application such as this. No current need be supplied to the magnet, hence no Joule heating occurs. Because of the unusual layout of the magnet, the field strength outside it will be small.

However, there are also some problems with a permanent magnet option. In order to demagnetize and re-magnetize slowly, it would be necessary to arrange some means of attenuating the field provided by the magnet. This might possibly take the form of a shield between the magnet and the salt pill within it, probably composed of either niobium-tin or or Cryoperm. Its gradual withdrawal from the pill will cause the magnet to affect a variable portion of the pill. A second problem with permanent magnets is that the field strength available with them is more limited. About 2 T is the largest field one could reasonably expect to obtain. At low field strengths, and a 1 K base temperature, Chromic Potassium Alum(CPA) becomes quite inefficient. At 1 T field we can only obtain about 35 % of the potential cooling capacity of CPA[11]. However, Ferric Ammonium Alum (FAA) is more efficient at this low field strength, and could supply nearly 50 % of its maximum capacity at 1 T. If we can generate a field as high as 2 T inside the salt, then CPA efficiency becomes 75 %, and FAA efficiency is 82 %. Given that the maximum cooling of FAA is 40 % greater than that of CPA per unit mass, then it will be useful to consider its use. The chief problem with the use of FAA as a salt is that it decomposes at about 40 celsius, as opposed to the 89 celsius decomposition point of CPA.

Assuming that the permanent magnet option is in an ADR, and that a FAA salt

pill is used, then it is possible to run a thermal model for the system. As in the ground-based model, the model was run in an equilibrium mode, and the heat flow into the salt pill used to determine heat flow. The model shows that the heat flow from the frame along the Kevlar strands are the dominant mechanism. The interesting consequence of this is that the hold time is independent of the mass of the pill in the mass regime of greater than a few grammes.

In the higher mass regime. although a larger pill gives a larger heat capacity, it also requires stronger supports, and any advantage is lost in the heat flow along these supports. What proves to be the determining factor is the conductivity of the supports, and this is strongly dependent on the temperature of operation. In the 3 K region the conductivity of Kevlar is roughly proportional to its temperature, so assuming we can extrapolate this behaviour down to 0.5 K, reducing the temperature of the frame by a factor of 2 increases hold time by a factor of 4. Not only is the conductivity of Kevlar halved, but the temperature gradient across it is also, hence a four times yield. By the same argument, operating the ADR from 4 K decreases the hold time enormously.

Bibliography

[1] *High Energy Astrophysics* - M.S. Longair, Cambridge University Press, 1981, ISBN 0 521 23513 8, ISBN 0 521 28013 3.

[2] *Study on Very Low Temperature Cryogenic Cooling - Final Report* - Wanner, Ettlinger, Schneider, Jewell at ESTEC, Study under ESTEC Contract No. 8527/89/NL/PP(SC), October 1990

[3] *An Adiabatic Demagnetisation Refrigerator with a Mechanical Pre-Cooler for Space Applications* - I.J. Davenport, A. Smith, I. Hepburn, P.A.R. Ade, T.J. Sumner, Proceedings of an ESA Symposium on Photon Detectors for Space Instrumentation held at ESTEC, Noordwijk on the 10-12 November 1992.

[4] *Novel High-field Permanent-Magnet Flux Sources* - H.A. Leupold, E. Potenziani II, IEEE Trans. Magnetics Vol. MAG-23, No.5 pp.3628-3629, September 1987

[5] *Principles and Application of Magnetic Cooling* - R.P. Hudson, North-Holland Publishing Company, 1972, ISBN 0 7204 1257 9

[6] *An Adiabatic Demagnetisation Refrigerator for SIRTF* - P.T. Timble, G.M. Bernstein, P.L. Richards, IEEE Transactions on Nuclear Science, Vol.36 No.1 pp.898–902, February 1989.

[7] *A Closed Cycle 4 K Mechanical Cooler for Space Applications* - T.W. Bradshaw, A.H. Orlowska, Proceedings of the 4th European Symposium on Space

Environmental and Control Systems, Florence 21-24 October, 1991, ESA Sp-324, pp.397-401

[8] *The AXAF/XRS ADR: Engineering Model* - Aristides, T. Serlemitsos, Marcelino SanSebastian, Evan S. Kunes, Advances in Cryogenic Engineering, Vol.37, Part B, Plenum Press, 1992

[9] *Design of a spaceworthy adiabatic demagnetisation refrigerator* - A.T. Serlemitsos, M. SanSebastian, E. Kunes, Cryogenics 1992 Vol.32 No.2

[10] *Mechanical Mounting of the First FIR Receiver* - D.G. Vickers, M.J. Griffin, P.A.R. Ade

[11] *In Orbit Adiabatic Demagnetisation Refrigeration for Bolometric and Microcalorimetric Detectors* - I.D. Hepburn, P.A.R. Ade, I. Davenport, A. Smith, T.J. Sumner, Proceedings of the ESA Symposium on Photon Detectors for Space Instrumentation, Noordwijk, 10-12 November 1992

[12] *Materials for magnetic refrigeration between 2K and 20K* - J.A. Barclay, W.A. Steyert, Cryogenics, February 1982, pp.73

[13] *Calculation of Heat Flow in a Medium, the Conductivity of which Varies with Temperature* - Richard L. Garwin, The Review of Scientific Instruments, Volume 27, Number 10, October 1956

[14] *Magnetic Refrigeration in Space - Practical Considerations* - P. Kittel, Journal of Energy, Vol.4 No.6 pp.266, Nov-Dec 1980.

[15] *Salt Materials testing for a Spacecraft Adiabatic Demagnetisation Refrigerator* - M.L. Savage, P. Kittel, T. Roellig, Advances in Cryogenic Engineering, Vol.35, Plenum Press, New York, 1990, pp 1439-1446

Chapter 7

A Space-Based ADR

In this chapter I describe a theoretical system for refrigeration in a space environment, and the methodology behind its design.

7.1 Objective

The objective of this exercise is to design a system that will allow an X-ray microcalorimeter, or any low temperature small detector, to operate at 100 mK with a high level of temperature stability, for periods in terms of hours, with a recycle time of considerably less. To this end, it will be necessary to consider a two-stage system. The low-temperature stage will operate between 100 mK and an intermediate temperature between 100 mK and the mechanical cooler temperature. A second stage will then operate with its low-temperature end at this intermediate temperature, and its high temperature end at the temperature of the mechanical cooler.

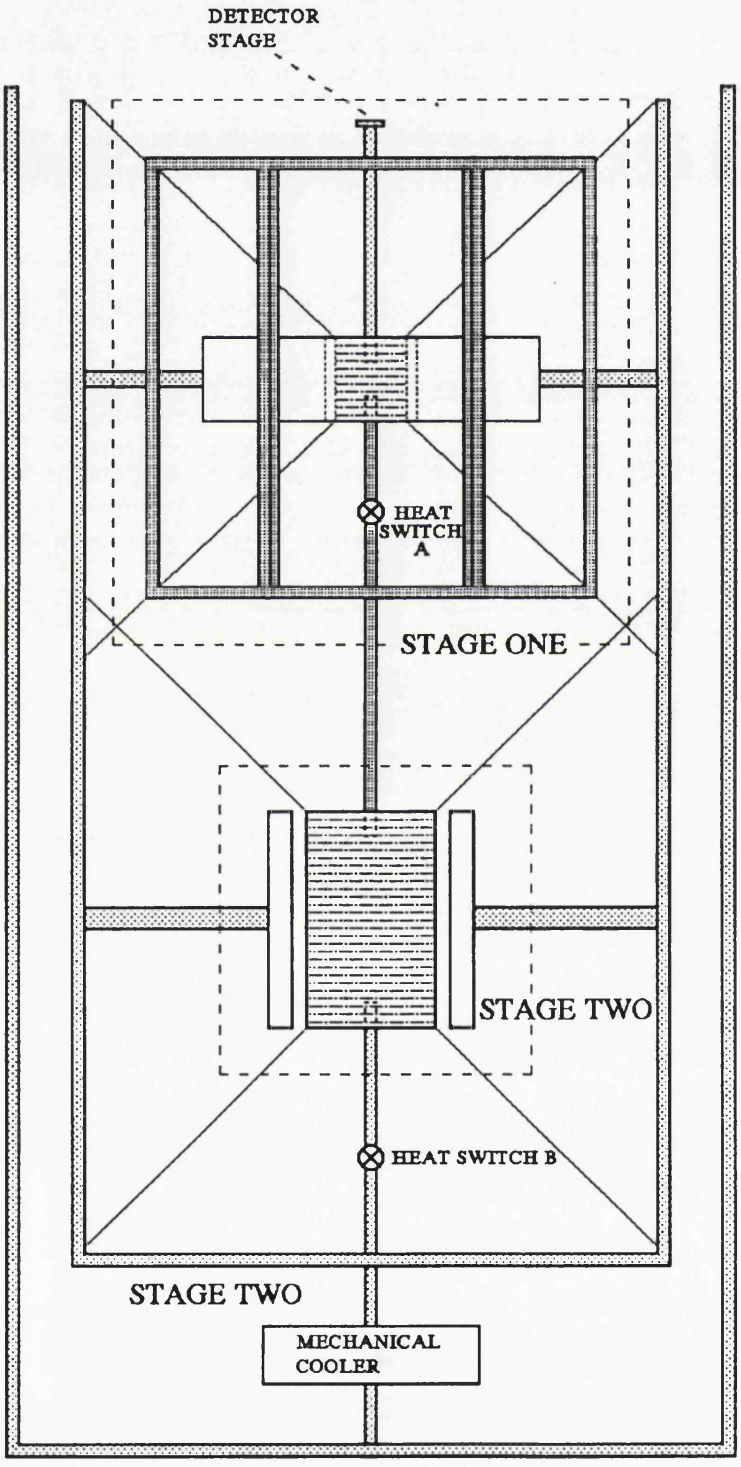

Figure 7.1: *Overview of Space-based ADR*

7.2 Brief Overview of Operation

The cooling system shown in Figure 7.1 is in essence a two-stage ADR. The cooling cycle is shown in Figure 7.2, and described below. In each of the diagrams the upper section (1) represents Stage 1 with its surrounding magnet, the middle section (2) represents Stage 2, also with a surrounding magnet, and the lower section is the heat bath, cooled by the mechanical cooler. A magnet which is clear maintains no magnetic field, solid diagonal lines through the magnet denote a magnet operating at maximum field, and broken diagonal lines indicate a condition of partial magnetisation. The opening and closing of the heat switch connections, labelled A and B as in Figure 7.4, are shown as physical links.

1. At the beginning of the cooling cycle, it is assumed that the whole device has been allowed to warm up to the ambient spacecraft temperature. The mechanical cooler is then started up, and both of the heat switches closed, so that the entire cooler will drop in temperature to 4 K.

2. Once this has been achieved, it will be necessary to open heat switch A and activate the magnet on Stage 2. This will cause the temperature of salt pill 2 to rise, and then fall back to 4 K because it is still in thermal contact with the mechanical cooler.

3. Once pill 2 has returned to 4 K, then it is necessary to isolate Stage 2 from the mechanical cooler, so heat switch B is opened.

4. The Stage 2 salt pill will then be demagnetised in a controlled manner so as to maintain a temperature of 1 K.

5. Once this temperature has been attained, then heat switch A can be closed, and thermal contact be established between the two salt pills. Because the Stage 2 salt pill heat capacity is much larger than that of Stage 1, the two salt pills will then acquire the same temperature, about 1 K. Stage 1 is then magnetised, and the magnetisation energy thus generated input to Stage 2.

Once this magnetisation energy is disposed of, pill 1 will return to 1 K, since it is still in contact with Stage 2.

6. Once the Stage 1 salt pill has reached 1 K, then it is isolated from Stage 2 by opening switch A.

7. Both magnetic fields are reduced in a controlled manner, to maintain pill temperatures of 100 mK and 1.0 K

8. The cooling power of either the Stage 1 or Stage 2 pill is exhausted, and the temperature of Stage 1, starts to rise. and both of the heat switches are closed

7.3 First Stage ADR Description and Thermal Model

The first stage cooler as shown in Figure 7.3 is an adiabatic demagnetisation refrigerator, as described in the previous section, operating between 100 mK and 1.0 K. It is composed of a salt pill of mass 50 g at its center. The pill is supported by six kevlar threads connecting it to a hexagonal frame. This frame is also connected to the pill via a heat switch,and is composed of a light, low heat capacity material, and is connected directly to the cold end of Stage 2. Support for this frame is given by six kevlar wires connecting it to the 4 K can in which it sits.

7.3.1 Hold Time

A 50 g salt pill is depicted in the model of Figure 7.3. The molar mass of FAA is 0.482 kg, and a magnetic field of approximately 2 T should be able to reduce the entropy in the FAA crystal to such a level at 1 K that 1.05 J per mole is available for cooling[2]. Hence a 50 g salt pill operating at 100 mK should be able to absorb 0.109 J of input heat energy. The thermal model shows that the

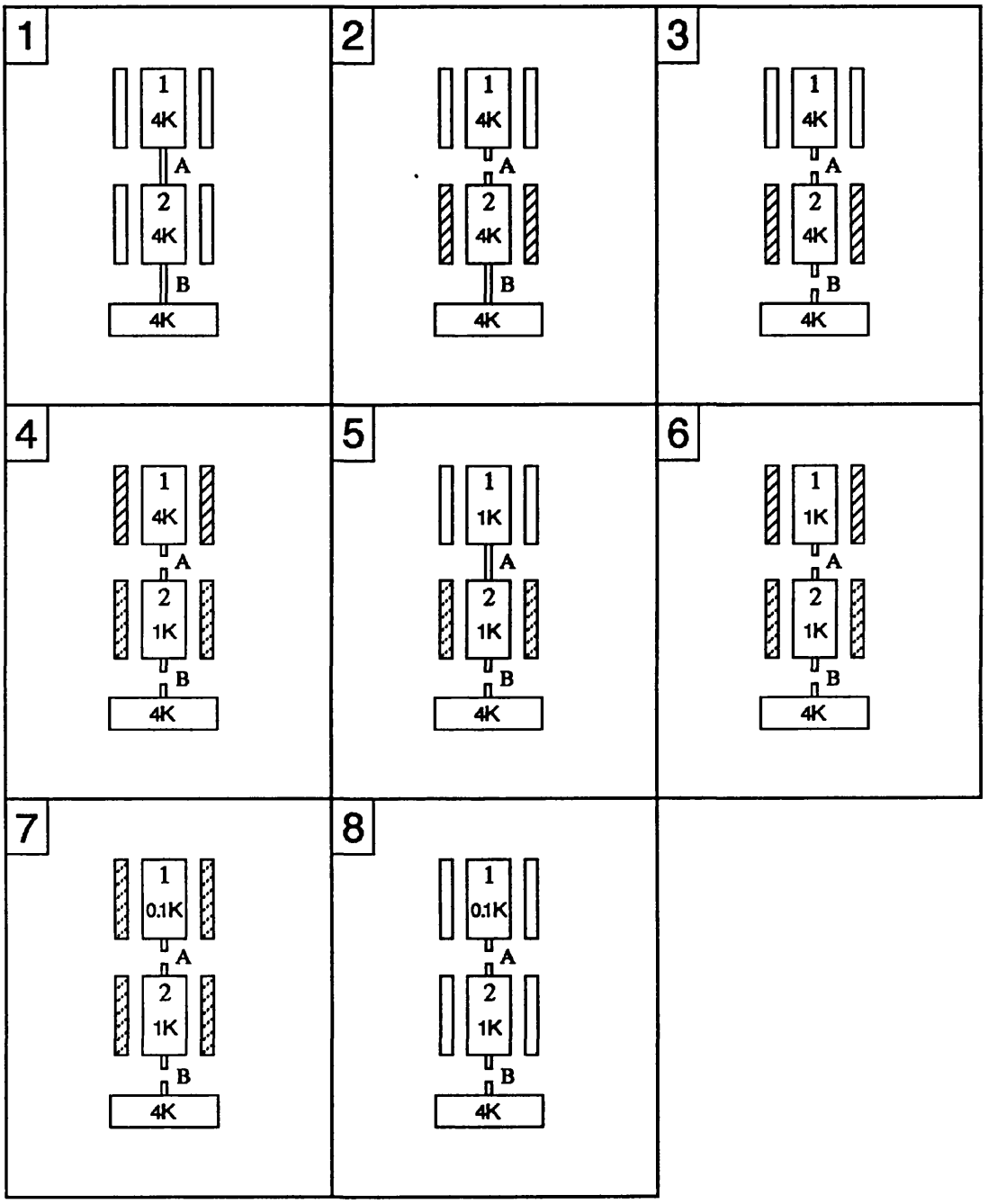

Figure 7.2: *Two stage ADR cycle*

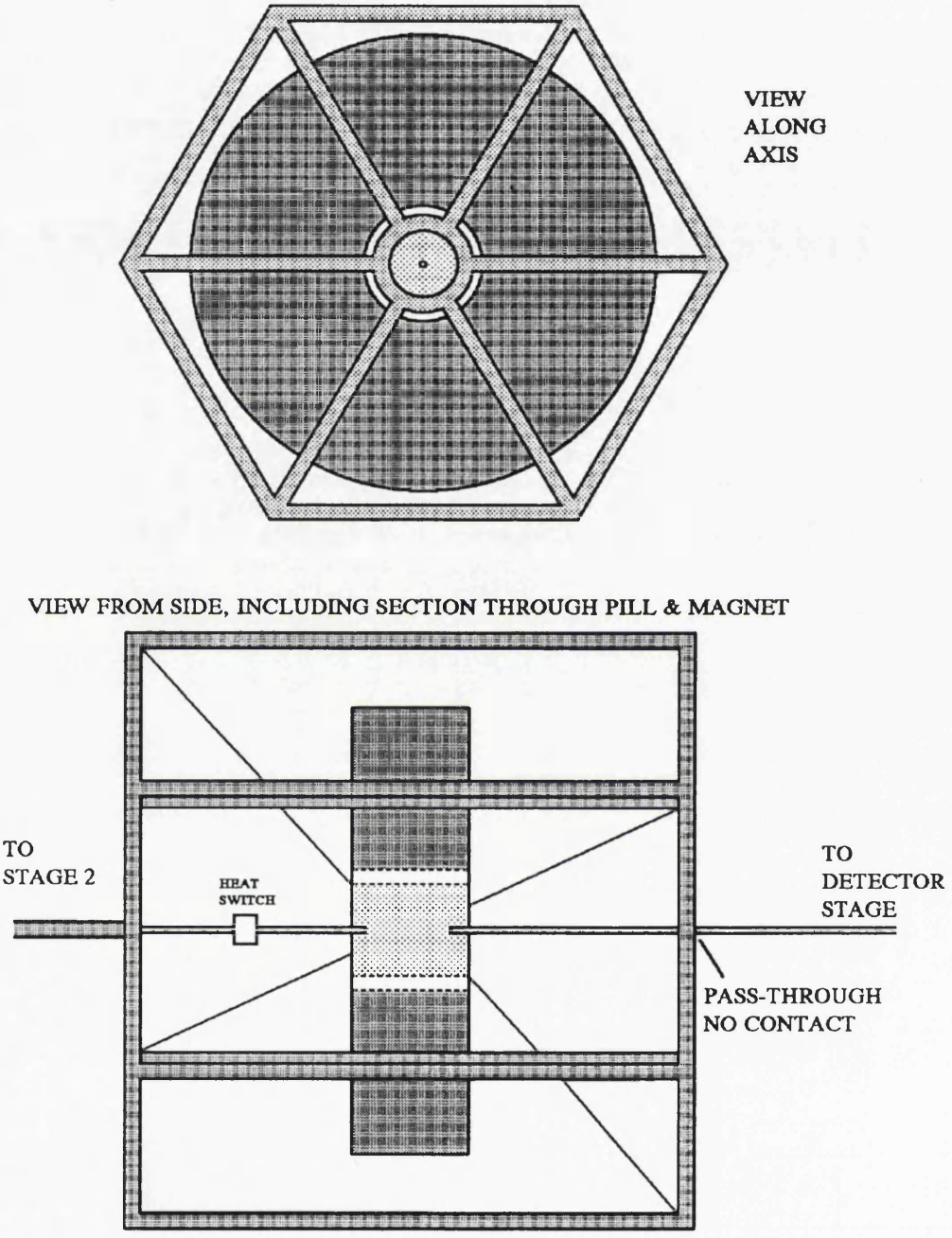

Figure 7.3: *Stage 1 of the Space ADR*

heat flow inside the Stage is chiefly conductive. The inflow to the salt pill is approximately 0.0545 μW, which gives a hold-time of approximately 550 hours.

As described in Chapter 6, the hold time is dependent on the square of the upper temperature, and the efficiency of the magnetic field in reducing the entropy of the pill, and a Stage 1 operating from a frame at about 2 K will have a hold-time in the region of 80 hours because of the reduction in efficiency of the magnetic field to 60 %, and a Stage 1 operating between 3 K and 100 mK will have a hold time of approximately 18 hours, because of the entropy reduction of the field at 3 K only being 30 % of that at 1.0 K.

It is possible that the heat switch in position A in Figure 7.1 has a finite conductance when open, and this will reduce the hold time. As described in Chapter 6, a typical open conduction for a gas heat switch is 10 μW over a temperature gradient of about 4 K. Since the temperature gradient between the Stage 1 pill and the Stage 2 pill is less than 1 K we might expect this conduction to be reduced by a factor of 4, and so we assume it to be 2.5 μW. In a space application two such heat switches would have to operate in parallel, hence giving a potential 5 μW power input to the pill, and reducing the hold time to 6 hours. It is therefore clear that if a gas heat switch is used in this position, then a drastic reduction in hold-time will result, however a mechanical heat switch, with a near-zero open conductance should be suitable here.

7.3.2 Recycle Time

The other important factor in the design of Stage 1 will be the amount of time it will take to cool it from the temperature of the low temperature end of the mechanical cooler. At the end of a cycle it must be assumed that Stage 2 has run out of cooling power, and the entire system will rise to the mechanical cooler temperature. This time will be dependent on the heat capacity of all the component parts of the stage. At the start of the new cycle it is necessary that the Stage 1 components have reached 1.0 K in order that the 1.0 K to 100 mK cycle can begin. This cooling must be achieved by the Stage 2 cooling cycle, which will

also cool the support frame. In Section 7.6.2 I show that approximately 0.3 J are required to cool the frame/pill/stage combination from 4 K to 1.0 K. Given that, when the temperature gradient between the frame and the 4 K case is maximum the heat flow from the frame is 6 μW, then a heat switch in position A shown in Figure 7.1 of conductance 10 mW will make this extraction time 30 seconds.

Once the pill is magnetised, the alignment of the dipoles within the pill will cause a temperature rise, and the resultant energy must also be extracted to bring the Stage 1 temperature back to 1.0 K before the cooling demagnetisation is possible. From [2] the energy of magnetisation of FAA when subjected to a 2.0 T magnetic field at 1.0 T is 13 $Jmol^{-1}$. Since the pill consists of 0.10 mol of FAA, this energy will be approximately 1.3 J, and must be extracted before the cycle starts. This time will be part of the recycle time, and assuming a heat switch conductance of 10 mW, should be drained in a time of approximately 130 seconds. This yields a total recycle time for Stage 1 of under 3 minutes.

7.4 Description of Second Stage ADR

There are two fairly well defined alternatives for Stage 2 of the cooling apparatus.

A method I shall explore in Section 7.7 is that of utilising a cooled helium bath, which held under low pressure should be able to maintain a temperature of 1.5 K, but which will expend helium in the cooling, and require a stock of helium to be part of the payload.

The method that would supply cooling power not dependent on the renewal of cryogens would be a stage composed of an ADR operating between 4 K and 1 K, as I have detailed above. This stage would have its upper temperature end cooled by a mechanical cooler, and would use a large salt pill with a surrounding electromagnet to cool its cold end to 1 K, which would be connected to the Stage 1 frame, and to Stage 1 via a heat switch between the frame and the Stage 1 pill.

7.5 Overall Arrangement Thermal Model

In order to appraise the design of the refrigerator, it is necessary to consider the operation of the complete device in its static mode, where the second stage is being demagnetised to maintain a 1.0 K temperature, and the first stage is maintaining a 100 mK detector stage. This is necessary to get an estimate as to the expected hold time, and to determine if the set-up is viable. To this end the arrangement is divided up into the following nodes, described here, and illustrated in Figure 7.4

7.5.1 Node 1 - Spacecraft

This describes the cavity in which the whole refrigerator/detector system sits. It is held at 20 K for the purposes of this model, but is flexible dependent on the only part in thermal contact with it, which is the mechanical cooler. This operates between Nodes 1 and 11, maintaining the 4 K temperature of the environment case.

7.5.2 Node 2 - The Link Stage

This is the thermal connection between the Stage 1 ADR and the Stage 2 ADR. It takes the form of a solid rod of metal, embedded well within the Stage 2 salt pill, and joined to the Hex frame of Stage 1. Between the point where this node is joined to the Hex frame and the Stage 1 salt pill is a heat switch, which enables the Stage 1 salt pill to be brought quickly to the temperature of the Stage 2 salt pill. This is referred to here as Switch A.

7.5.3 Node 3 - Stage 1 Magnet

This is the magnet which surrounds Stage 1. In the current design this is a permanent magnet giving a 2 tesla magnetic field in the manner described above.

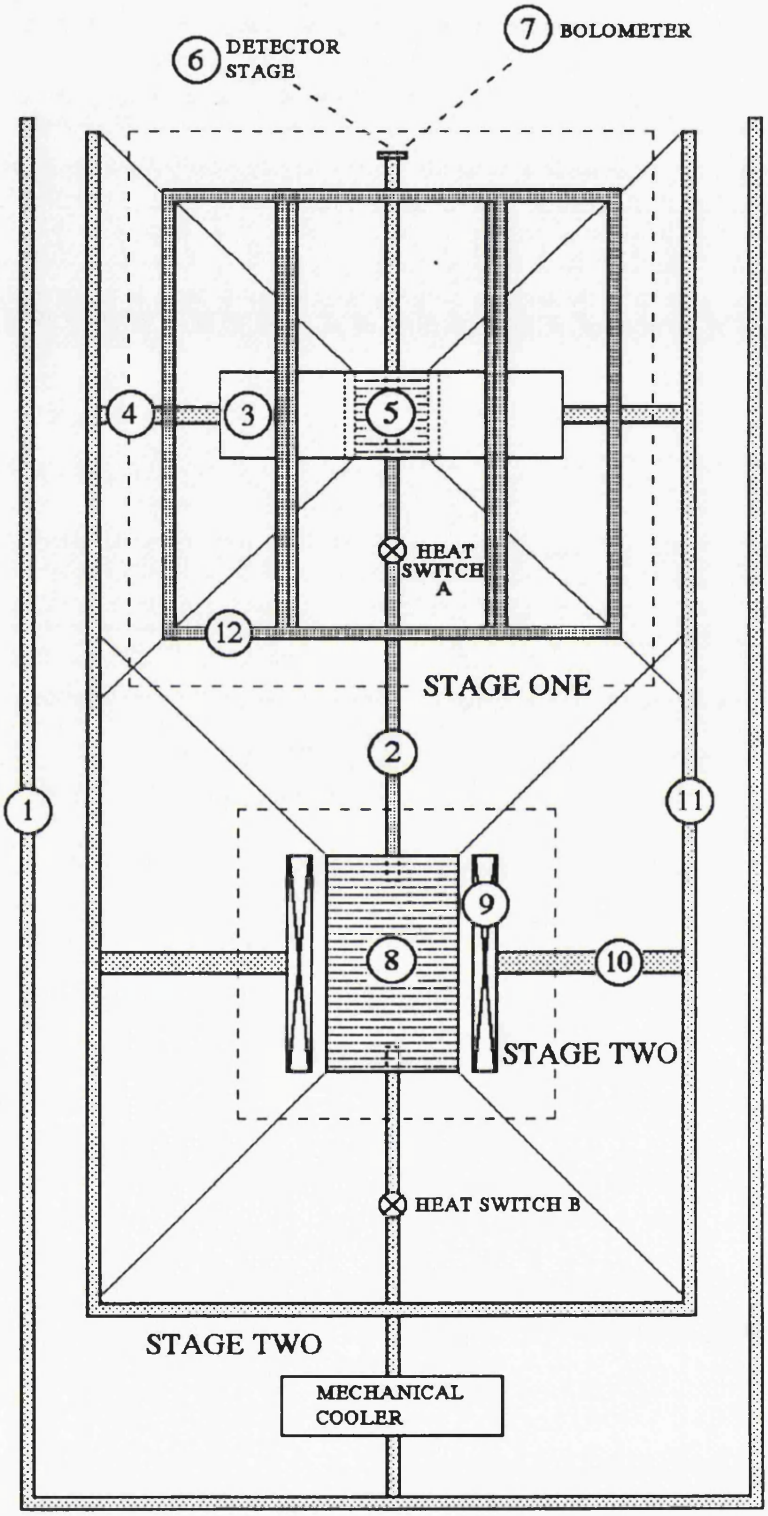

Figure 7.4: *The node structure of the System Thermal Model*

As yet a means for varying the magnetic field around the pill for the procedure has not been finalised, however it may be feasible to:-

1. Have a shield in place as described in Section 6.6.3.2.

2. Have a heating element on the detector stage to maintain a constant temperature. This would eliminate the need for a gradual demagnetisation during warm-up, however it does not remove the need for variation in magnetic field elsewhere in the cycle. This technique would require a finite conductance between the pill and the detector, and would cause a flow of heat from the heating element to the pill, thus reducing the hold time.

The magnet is held at 4 K, and supported by six metal struts, which connect it to the environment case, Node 4.

7.5.4 Node 4 - The Stage 1 Magnet Supports

These are six struts which connect the Stage 1 magnet to the environment case. Both of the nodes it connects are at 4 K, as are the struts.

7.5.5 Node 5 - Stage 1 Salt Pill

This is the salt pill, composed of Ferric Ammonium Alum or Chromic Potassium Alum, which is at the heart of Stage 1. Currently it is only 50 grammes in mass, and is supported by six kevlar wires, which are arranged so that movement in all three dimensions is controlled. These wires go to node 12, the Hex frame. The pill, when in operational mode, is at 100 mK, and the Hex frame is kept in good thermal contact with the Stage 2 salt pill at 1 K. This means that there is some heat flow down the kevlar wires, and this is the chief source of parasitic heat loss from the salt pill, and determines the hold time for this stage.

7.5.6 Node 6 - The Detector Stage

This is a small copper rod embedded into the Stage 1 salt pill at one end, and with a platform on the other end. This platform is for the detector to be mounted upon, in this case Node 7, a bolometer.

7.5.7 Node 7 - The Bolometer

This is for the purposes of this model, the detector to be mounted on the detector stage. Typically such detectors are less than 1 mm in each dimension.

7.5.8 Node 8 - Second Stage Salt Pill

This is the salt pill which is at the heart of the second stage. In the model this pill is composed of gadolinium gallium garnet(GGG), the chemical formula for which is $Gd_3Ga_5O_{12}$, discussed in [3]. When in operating mode, it will be at 1 K. The pill is supported by six kevlar wires, which, as with the Stage 1 pill supports, are arranged so as to limit movement in three dimensions. The other ends of these wires are connected to the environment case, at 4 K, and so these wires are one of the two chief sources of heat inflow to this pill, and hence a significant factor in calculating hold time for Stage 2. The other source of heat inflow is from the Hex frame (Node 12) via the Linking Stage (Node 2). The pill is also linked via heat switch B to the environment case.

7.5.9 Node 9 - The Stage 2 Magnet

This is a superconducting electromagnet, which can generate a field of 6 tesla in its cavity, where the Stage 2 salt pill resides. It is supported by six metal struts (Node 10). This magnet is held at 4 K.

7.5.10 Node 10 - The Stage 2 Magnet Supports

The Stage 2 magnet is supported by six metal struts, which connect to the environment case (Node 11). All of these nodes operate at 4 K. The supports will also have to carry the cables supplying and removing current from the magnet. At 4 K it should be possible to use a superconductor for this, so that joule heating will be negligible.

7.5.11 Node 11 - The Environment Case

This is the case within which the system is contained. Inside it is directly linked to the Stage 1 Hex frame, the Stage 1 magnet and the Stage 2 salt pill. The case is connected to the mechanical cooler, which keeps it at 4 K.

7.5.12 Node 12 - The Stage 1 Hex frame

This a a frame which has struts at the edges of an imaginary hexagonal prism, and has supports across the diameters of the hexagonal faces. On one face, these supports connect it outwards to the linking stage (Node 2), and inwards to heat switch A and the Stage 1 salt pill. On the other side the supports have a hole in the center of the face for the detector stage to protrude through, connecting to the salt pill.

7.6 Determination of the Stage 2 Salt Pill Mass

Having modelled the complete refrigeration system in a steady-state mode, it is necessary to study the heat flow into the Stage 2 salt pill in order to determine its optimum mass.

The cooling power supplied by the Stage 2 salt pill must :-

- Achieve all the cooling of Stage 1 down to 1 K and remove the magnetisation energy from the Stage 1 pill before Stage 1 operation begins.

- Drain the power flow from the 4 K shell supporting the hex frame to the frame. If this is not done the frame temperature will start to rise.
- Accommodate the heat inflow to it along its support wires. This can be calculated as for the Stage 1 pill supports, and will be determined by the mass of the salt pill.

In order to calculate the hold time of Stage 2 it is necessary to determine a set of equations to describe the above. It can be stated that the energy available from the pill must be sufficient to cool Stage 1, drain the magnetisation energy, and allow the parasitic losses to the Stage 1 frame supports, and the Stage 2 pill supports for the duration of the hold time. Mathematically, this can be expressed as :-

$$M_s \times \rho_E = Q_{cool1} + P_1 \times t_H + P_2 \times t_H$$

or

$$M_s \times \rho_E = Q_{cool1} + P_1 \times t_H + P_{2m} \times M_s \times t_H$$

where,

- M_s is the mass of the Stage 2 salt pill,
- ρ_E is the energy absorbable from the Stage 2 salt pill per unit mass,
- Q_{cool1} is the energy required to be removed to bring the temperature of all of Stage 1 down from 4 K to its stable 1 K level.
- P_1 is the heat flow down the supports for the Stage 1 frame from the 4 K shell.
- P_2 is the heat flow down the supports for the Stage 2 salt pill, and since it depends proportionally on the M_s, is defined as the product $P_{2m} \times M_s$.
- t_H is the length of time the Stage 2 salt pill will be able to maintain the heat drain.

The solution of the above equation will involve making a number of arbitrary decisions on, for example, the length of support wires, which I will determine from the computer model. These will have a strong influence on the chief factors we need to determine from the equation, M_s and t_H. It will therefore be necessary to reduce the equation somewhat, but leave in dependence on possible changes. Below I describe each of the terms in the equation above, and discuss what might be done to improve the efficiency of the design.

7.6.1 Determination of ρ_E

ρ_E is the energy absorbable per unit mass of the Stage2 salt pill. In order to determine this, it is necessary to determine the reduction in entropy at the upper temperature that is caused by the application of the magnetic field that the Stage2 magnet provides. In Figure 7.5, where the vertical axis shows entropy per mole of the substance, the shaded area shows the energy per mole available in cooling.

The energy available per mole is therefore easily obtainable, and reference to the entropy diagram for GGG in [3] gives the figures I show in Table 7.1 for a 4 T to 1 T cooling.

The molar mass of GGG is calculated as being 1012.5 g = 1.012 kg. However, in each molecule of GGG are three gadolinium ions, so that the gram-ion mass is 337.5 g.

For a 6 T field, an energy density of approximately 3.48 $\mathrm{Jmol^{-1}}$ is available, and this is the case I use in further calculations.

7.6.2 Determination of Q_{cool1}

Q_{cool1} is a simple flat term, which contains the heat capacity of the Stage1 parts between the temperatures 4 K and 1 K, and the energy generated inside the salt pill by the magnetisation.

Energy available for cooling from GGG				
Highest Magnetic Field Available (tesla)	Entropy removable per gram-ion ($J.K^{-1}$)	Cooling available per g-ion (joule)	Cooling available per kg (joule)	Cooling as a proportion of maximum (%)
1.0	-	-	-	
2.0	0.12	0.12	0.36	6.7
3.0	0.51	0.51	1.50	28.7
4.0	0.78	0.78	2.31	43.8
5.0	1.02	1.02	3.03	57.3
6.0	1.17	1.17	3.48	65.7
7.0	1.33	1.33	3.93	74.7
8.0	1.45	1.45	4.29	81.5
9.0	1.54	1.54	4.56	86.5
∞	1.78	1.78	5.22	100.0

Table 7.1: *GGG cooling energy*

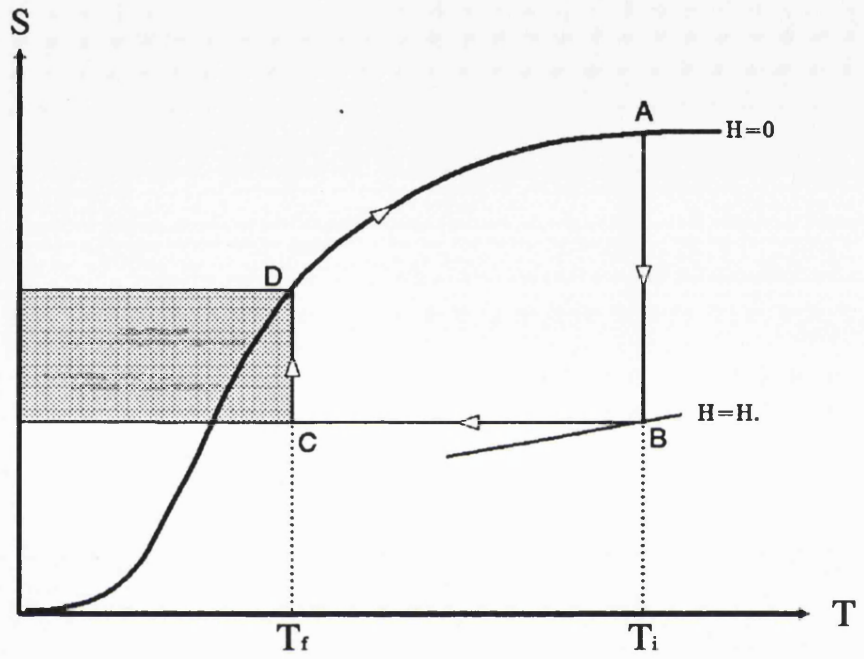

Figure 7.5: *Determination of absorbable energy density* ρ_E

The heat capacity element includes the salt pill, since it must be brought to 1 K before being cycled to 0.1 K, the hex frame, and the copper rods embedded in the pill, which provide thermal conduction to the detector, and to the frame via a heat switch.

The most massive part by far of the stage will be the magnet. Using a cylindrical design as described by Leupold and Potenziani II[1], designed to supply a magnetic field of 2 T to a 50 g salt pill requires a magnet of about 8 kg mass. This requires a strong support structure, and hence will cause a large heat input to the stage if held at 1 K. It is therefore proposed that the magnet be held in thermal equilibrium with the mechanical cooler cold end, as shown in the overview Figure 7.1, and be thermally isolated from the rest of Stage 1. As such the magnet will not contribute to the heat capacity of Stage 1.

The next most massive part of this stage, and thermally the most significant part

is the hexagonal frame. The radius of the structure is about 0.110 m, with a depth of 0.040 m. Assuming that each of the struts composing it have a cross-section 5 mm square, and the frame can be made from a fairly light material, a space-qualified equivalent of aluminium, the structure could have as low a mass as 0.2 kg. The heat capacity of the structure is non-trivial to calculate because of the large range of temperature the cooling operates over. Since at these low temperatures the specific heat of materials varies greatly, it is necessary to either use a number of discrete values and interpolate interval values, or to determine by theory or empirical means an equation, and integrate the heat required. By using the values of specific heat at 1, 2, 3 and 4 K and interpolating, I have determined that the energy to reduce the temperature of 1 kg of aluminium from 4 K to 1 K is about 0.525 J. This would mean a 0.2 kg frame would require the extraction of about 0.11 J.

The salt pill itself has a mass of only 50 g, and requires the extraction of less than a joule to cool it from 4 K to 1 K. My approximate calculation is that 0.03 J are required. The detector stage is comparatively small, with a mass of approximately 6 g, as is the thermal connection to heat switch A, and both require only a approximately 1 mJ to bring them down to 1 K.

Therefore, given the fact that some of this energy will be lost in the parasitic flow from the frame to the 4 K case, the total amount of energy required to bring Stage 1 down from a temperature of 4 K to a temperature of 1 K is under 0.3 J.

The magnetisation energy of the pill at 1.0 K with an applied field of 2 T is given in [2], and, as described in Section 7.3.2 for the FAA pill in Stage 1 will be 1.3 J. This yields a total Q_{cool1} of 1.6 J.

7.6.3 Determination of P_1

P_1 is the heat flow per unit time down the supports for the Stage 1 hex frame. Currently the mass of the frame is calculated as approximately 0.2 kg, based on an aluminium construction. The mass will obviously change if a different material is decided upon, or if a design change is necessary. Since the size of the supports

for the frame will depend largely on the its mass, there is clearly scope for change in this factor.

The power P_1 is determined by calculating the heat flow along the six kevlar wires to it across the temperature gradient of 4 K to 1 K. In calculating this heat flow it is assumed that in considering heat flow through a medium with a varying temperature along it, only the conductance at the mean temperature of the ends need be considered. The proof of this is to be found in [4]. To decide the required radius of the Kevlar strands supporting the frame, we invoke the empirical formula $r = 0.00079\sqrt{(M)}$, where r is the radius in meters, M the mass in kg, and the constant derived from the fact that six 0.5 mm strands are suitable support for a 0.1 kg mass, as I proved earlier in Section 6.6.1.2. We then come to a strand radius for the frame support of 0.35 mm for the 0.2 kg mass of the frame. The flow along six of these strands from the 4 K to the 1 K regions is approximately 5.8μW if the strand length is estimated at 50 mm. An equation that allows for the alteration of the mass of the frame M_f and the length of the supports x_1 is easily derivable, as shown below.

$$P = K.A.\frac{dT}{dx}$$

where

- P is the transferred power between the two points
- K is the thermal conductivity of the transfer material between the points
- A is the cross-sectional area of the transfer medium
- dT is the temperature gradient present between the points
- dx is the distance between the two points

From this we can derive

$$P_1(watts) = 1.45 \times 10^{-6} \times \frac{M_f}{x_1}$$

or

$$P_1(\mu watts) = 1.45 \times \frac{M_f}{x_1}$$

7.6.4 Determination of P_2

P_2 is the heat flow down the supports for the Stage 2 salt pill, and has the same dependence as P_1. We can use the same power equation shown above, since the same temperature gradient applies, and the same material, Kevlar, is assumed to be used as the support. In this case M_f is replaced by M_s, the Stage 2 salt pill mass, and x_1 becomes x_2, the length of the support strands for the salt pill. We now have

$$P_2(watts) = 1.45 \times 10^{-6} \times \frac{M_s}{x_2}$$

The current model for the ADR has the length of the support wires as 150 mm, or 0.15 m. This leads to a heat flow of

$$P_2(watts) = 9.7 \times 10^{-6} M_s$$

Hence P_2 can be represented as $P_2 = P_{2m} \times M_s$, where $P_{2m} = 9.7 \times 10^{-6}$

Rearranging the above hold-time equation, we obtain

$$t_H = \left(\frac{M.\rho_E - Q_{cool1}}{P_1 + P_{2m}.M}\right)$$

Using the initial values calculated above, and assuming that we operate Stage 2 using a 6 tesla electromagnet, we obtain this equation describing hold time variation with the mass of the Stage 2 salt pill:-

$$t_H = \left(\frac{M \times 3.48 - 1.6}{5.8 \times 10^{-6} + 9.7 \times 10^{-6} \times M}\right)$$

We can see from this equation, that as the mass of the Stage 2 pill becomes greater, the hold time available will tend towards 100 hours. Table 7.2 shows the

Hold time for Stage2			
Mass (kg)	Hold Time t_H (hours)	Mass (kg)	Hold Time t_H (hours)
0.1	0.0	2.5	65.6
0.2	0.0	3.0	70.4
0.3	0.0	3.5	73.9
0.4	0.0	4.0	76.7
0.5	3.7	4.5	79.0
0.6	11.7	5.0	80.8
0.7	18.4	5.5	82.4
0.8	24.3	6.0	83.7
0.9	29.3	6.5	84.8
1.0	33.7	7.0	85.8
1.1	37.6	7.5	86.6
1.2	41.0	8.0	87.4
1.3	44.1	8.5	88.1
1.4	46.9	9.0	88.7
1.5	49.4	9.5	89.2
1.6	51.7	10.0	89.7
1.7	53.8	10.5	90.2
1.8	55.7	11.0	90.6
1.9	57.5	11.5	90.9
2.0	59.1	12.0	91.3

Table 7.2: *Hold Time Available from Stage2*

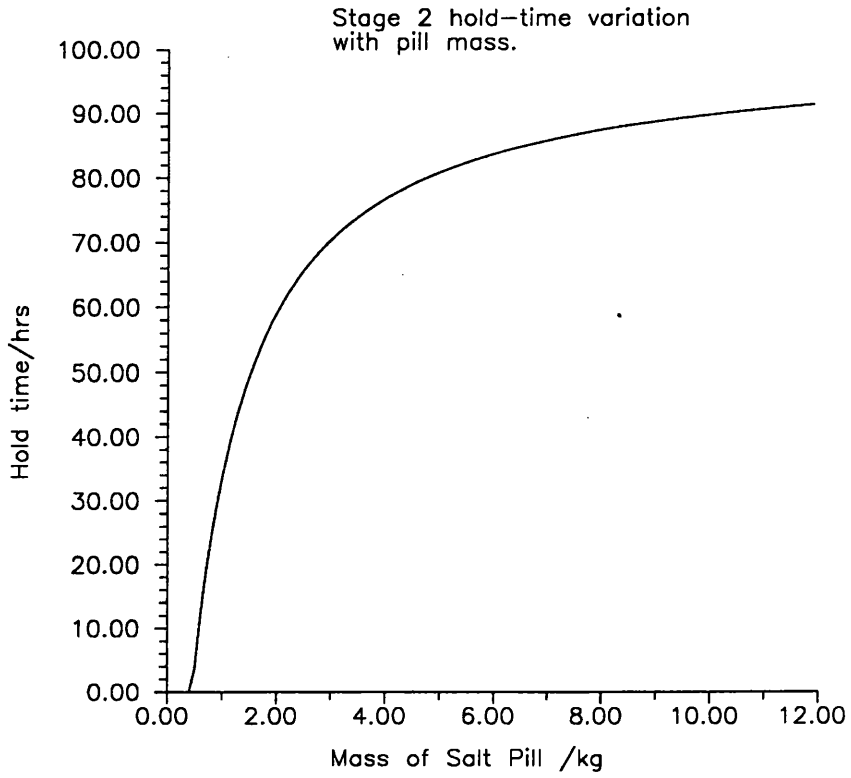

Figure 7.6: *Variation in Stage2 hold time with pill mass*

hold time available per unit mass of salt pill, and Figure 7.6 shows the same data graphically.

It can be seen from this that most of the maximum capacity is obtained by the time the mass has risen to 2 kg, where the hold time is 59 hours. Doubling the mass of the pill to 4 kg only results in a hold time extended by 18 hours.

For the basic Stage 2 model, then, a hold time of 59 hours seems to be the practical limit. Assuming this is coupled with a suitably short recycle time, this is quite adequate.

7.6.5 Recycling Stage 2

In addition to the recycling of Stage 1, involving the cooling of the pill and frame, and the removal of magnetisation energy, at the beginning of each cooling cycle it will be necessary to initialise Stage 2 first. Since the mechanical cooler will be operating continuously at 4.0 K, extracting the energy to keep Stage 2 at 4 K, the

only consideration will be the removal of the magnetisation energy generated by applying a 6 T field to the GGG salt pill at 4.0 K. This will be the only time that an element inside the 4 K shell will become warmer than the shell, and it is therefore important that this energy be removed as soon as possible. The magnetisation energy of GGG is easily calculable from [3] as approximately 43 Jgram-ion^{-1}, and since a 2 kg GGG pill has 6 gram-ions, an energy of 258 J will be generated.

Since the mechanical cooler should be able to remove 5 mW from a 4 K object, 258 J will require at least 14.3 hours to recycle, plus the 3 minutes required to cool Stage 1. This is a rather long time, and given the 59 hours usable time yields an efficiency of only 80 % in terms of 100 mK time over total time.

7.7 An Alternative Stage 2 - Cooled Helium bath

As an alternative to the Stage 2 ADR described above, it is also possible to operate a cooled helium bath to provide the intermediate temperature of the system. It may be necessary to adjust this intermediate temperature in the system, however. In projects such as the *Infrared Astronomical Survey* (*IRAS*), the *Cosmic Background Explorer* (*COBE*) and *ISO* a helium cryogen tank is used, typically of a volume of a few thousand litres. This liquid is subjected to a low pressure, and so is useful for getting down to about 1.8 K. This is a useful system, since there is no cycling involved, hence the only limit on hold time is the Stage 1 salt pill. The loss of helium from the storage tank is kept to a minimum by the mechanical cooling of the tank.

The implications of using such a device as Stage 2 are

- The change of intermediate temperature will require a re-appraisal of Stage 1, considering its hold-time in this configuration. My appraisal of the variation in hold time with intermediate temperature in Section 7.3.1 suggests that operating at 2.0 K would yield a Stage 1 hold time of approximately 80 hours. This is only 20 hours better than the hold time given by the ADR

Stage 2. The recycle time imposed by this change is the recycle time of Stage 1, less than 3 minutes.

- A fixed supply of helium puts a finite lifetime on the refrigerator, and although this lifetime can be made as long as necessary, it is at the expense of mass and size of the system. For instance, in the case of *ISO*, a tank of 2300 litres of Helium is intended to maintain the 1.8 K temperature for a period of at least 18 months.

7.8 Conclusions re: a viable space refrigeration system

The two-stage ADR described in this chapter provides some solutions to the problems inherent in operating at a temperature as low as 100 mK in a space environment. Although the recycle time is somewhat longer than would be ideal, it is a system that requires no attention, and does not have a fixed lifetime.

The Stage 1 ADR backed by a mechanically cooled bath of helium, as used by, for example, *ISO*, is the alternative to this, which although it gives a hold time only slightly greater than that of the Stage 2 ADR, has no need of recycling the high temperature stage, and thus the recycle time of such a system would be just that of the Stage 1 ADR, less than 3 minutes.

The deciding factors between the two systems must be how tolerable are the disadvantages of a well-defined lifetime, and the vast mass of the helium system. Since any observing platform is designed with a specified lifetime, the promise of an extension of lifetime should not be a determining factor in this argument. The key question then becomes the acceptability of the high mass of the helium Stage 2, and this depends very much on the launch system, and the possible alternative uses of the mass saved by an ADR Stage 2.

In addition these items need further thought and study:-

- The development of a system to alter the magnetic field applied to the Stage 1 salt pill. This may take the form of the removable shield alluded

to in Section 6.6.3.2, but the viability of such a system is still questionable. It may be possible, given the layout of the magnet, to make a shield which rotates about the magnet axis, providing a shield at one position where the flux is perpendicular, but when rotated by 90° the majority of the metal is not obstructing field lines. This would be a little simpler, since the shield would only have to be rotated rather than withdrawn.

- The power supply system for a superconducting electromagnet requires some consideration. A means of feeding a current of the order of 10 amps into the magnet has to be devised, and the gradual demagnetisation procedure requires a gradual draining off of this current. This may be difficult to achieve with currently available power systems, and requires some consideration.

7.9 Electronic Control Systems

In a complete model of a space-based detector system it is necessary to consider the overall design layout of the control electronics. In Chapter 3 I specified the algorithm for obtaining energy histograms from a microcalorimeter, and here I shall show where this processing fits into a total system.

In Figure 7.7, the block diagram for the system is shown, and below I will describe each of the subsystems.

7.9.1 On-board Electronics Functions

The function of the on-board electronics will be:-

1. To interpret and implement the telecommands of the on-board data handling system (OBDH).

2. To control and monitor the instrument.

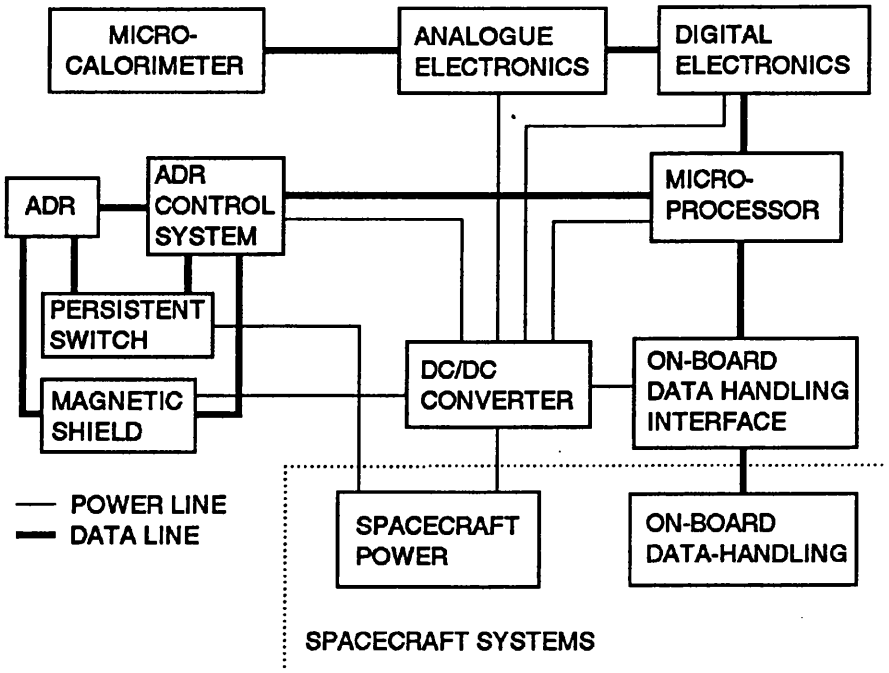

Figure 7.7: *Block Diagram*

3. To provide housekeeping data to the OBDH for transmission to ground.

4. To acquire microcalorimeter event data.

5. To process and analyse event data according to different modes of operation.

6. To provide power to the subsystems of the instrument.

7.9.2 System Telecommands

Typical telecommmands for this system might be

- Initiate steps in the ADR cycle, given the required detector temperature. This could be a pre-programmed function, ie. one command to initiate the cycle, or a step-by-step process as a backup.

- Data acquisition and the setting-up of data modes. This could be one of the following techniques.

  1. Transmit each X-ray event profile (as a diagnostic measure).
  2. Apply the matched filter to an individual pulse, and transmit the calculated height. This would be the nominal mode of operation.
  3. Accumulate an X-ray spectrum on-board, and transmit the resultant histogram. This would be a low data-transfer rate means of operation. It should also be possible to use this mode in a period-folding mode, so that a spectrum is generated after well-defined intervals, and any time-dependence is evident.
  4. A calibration mode will enable the matched filter to be devised, by moving the calibration source into place, and observing a set number of resultant X-ray events. This calibration source will probably be a $^{55}_{26}$Fe source with a filter between the source and the detector to block the K_β X-rays.

  Parameters which will be specified in data acquisition will be:-

  - The mode and submode of operation.
  - The integration time for spectrum build-up.
  - The period for period-folding.
  - The number of bins in the spectrum histogram.

- Switching power on and off to the experiment subsystems.
- Microprocessor commands, including system reconfiguration.
- Sofware patching, to modify parts of the processing code.
- Housekeeping mode, to monitor ADR temperature, the DC/DC converter current supply to each experiment subsystem, and the status of the various mechanisms. This could also include microprocessor housekeeping tasks, such as memory integrity monitoring.

7.9.3 2-Stage ADR Control Diagram

Figure 7.3 shows the sort of control structure that would have to be coded as the pre-programmed control for the ADR. Note that in this case I have assumed that a magnetic shield is used to reduce the magnetic field strength in the Stage 1 salt pill, although this does not change the form of the control structure.

7.9.4 Electronic System Constraints

Electronic packages used as part of space-based systems are subject to a number of constraints often not required of similar Earth-based systems. The most significant of these are listed below

- Since the system must generate all the required electrical power from (typically) solar arrays, systems are usually optimised to require as little power as possible, and this usually means the use of low-power CMOS electronics.
- Launch constraints mean that the package should have as low a mass as possible, and this includes the electronics. Consequently an integrated approach is taken to design, however, this close a clustering of electronic components in a small volume can cause thermal problems.
- The space environment generally causes a higher level of ionizing radiation than experienced on Earth, and consequently it is necessary to assess the radiation environment of the selected orbit (See Chapter 6) and allow for this in the selection and monitoring of components.
- High reliability is required of the entire system, and consequently all the components. For space purposes long lifetime components, typically conforming to the US military specification MIL883 are used.

  To extend the lifetime of components 'derating' is used. This is the practice of using components well below their rated specification in order to reduce the stresses on them, and extend their lifetime.

2 Stage ADR Cooling Cycle				
Step No.	Title	What is Done	What Occurs	What is Observed
1	Initial cooling	ON command is given to mech. cooler	Mechanical cooler activated	Temp. of mech. cooler drops
2	Thermal Equalisation	CLOSE command given to heat switches	Heat Switches A and B close	Temp. of both stages drops
3	Isolate Stage 1 from 2	OPEN command given to heat switch A	Heat switch A opens	Heat switch microswitch
4	Stage 2 Magnetisation	Full power command given to Stage 2 magnet	Stage 2 pill magnetises	Temp. of Stage 2 pill rises and falls
5	Isolate Stage 2 from mech. cooler	OPEN command given to heat switch B	Heat switch B opens	Heat switch microswitch opens
6	Stage 2 demagnetisation	Power to Stage 2 magnet reduced	Stage 2 pill mag. field drops	Temp. of Stage 2 drops
7	Stage 1 initial cool	CLOSE command given to heat switch A	Heat switch A closes	Temp. of Stage 1 drops
8	Magnetise Stage 1	Withdraw Stage 1 magnetic shield	Stage 1 mag. field increased to maximum	Stage 1 pill temp rises and falls
9	Isolate Stage 1 from 2	OPEN command given to heat switch A	Heat switch A opens	Heat switch A
10	Stage 1 demagnetisation	Magnetic shield gradually inserted	Stage 1 mag. field slowly decreases	Temp. of Stage 1 drops and levels
11	End of cycle	Cooling power exhausted,	Return to Step 2	Temp. of Stage 1 rises

Table 7.3: *ADR Control Cycle*

Circuits can also be designed in such a manner as to reduce the effects of degradation and failure, and combining this with redundancy extends the expected system lifetime.

7.9.5 Analogue Electronics Subsystem

An amplifier circuit such as that shown in Figure 2.5 in Chapter 2 would be a suitable means of making the microcalorimeter output more suited to input to the digital processing stage. A FET as shown would consume approxmimately 50 mW, and the pair of amplifiers would consume as little as 14 mW.

7.9.6 Digital Electronics Subsystem

The function of the digital electronics stage is to convert the analogue output from the analogue electronics stage to a digital form by use of an analogue to digital converter (ADC) so that the microprocessor stage can deal with it.

With an event duration of 0.5 ms, and a requirement to sample 50 times during the event, a sample is required every 10 μs. This means that the ADC must have a speed of 100 kHz or over. This is not a particularly demanding speed, and should be achievable using either of the two main types of ADC. 8-bit sampling will be sufficient for this application.

- A flash ADC consists of a number of comparators in parallel, each comparing the input voltage to a reference voltage. The result of the comparisons is fed to a logic circuit which calculates the digital word. This is a very fast means of conversion, however a differential non-linearity of $\frac{1}{2}$ the least significant bit is typical, which degrades the quality of the data.

- A Wilkinson ADC consists of a comparator with one of the inputs being fed by a capacitor being charged by a constant current source, and the other fed by the ADC input. When the capacitor starts charging a clock is started, which stops when the two comparator inputs are the same. The clock value

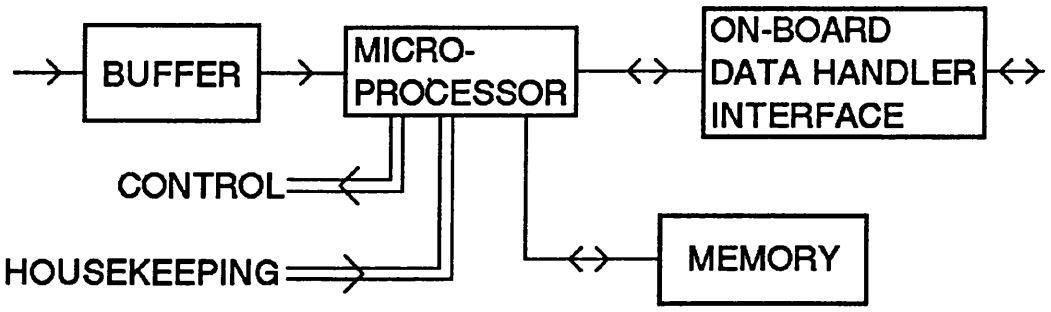

Figure 7.8: *Microprocessor Diagram*

is then fed to the output as the digital equivalent of the analogue input. This system is slower than the flash ADC, but is more consistent. It is fast enough for the 100 kHz rate required for this application, and a differential non-linearity of 1 to 2 % is possible for such a device.

7.9.7 The Microprocessor Subsystem

The microprocesor subsystem in Figure 7.7 is actually comprised of the elements shown in Figure 7.8.

7.9.7.1 Microprocessor Elements

- The buffer contains the data being sent to the microprocessor system from the ADC. This buffer will be cyclic in nature, so that when an event occurs some data from before the event is available.
- The microprocessor itself serves simply to accept instructions from the memory block and the process these instructions by accessing the buffer. It will handle commands given to it by the OBDH instructing it on modes of operation as discussed earlier, and it will instruct the ADR control system

and the electronics subsystems as to modes of operation. It will also handle housekeeping operations.

- The system memory consists of two types, read only memory (ROM) and random access memory (RAM). Typically the ROM will be erasable programmable ROM (EPROM) for ease of modification on Earth. The ROM will contain the programme to be executed by the microprocessor, and the RAM will contain the data. It is usual, however, to copy the programme from ROM to RAM for execution; this allows the programme to be modified by the use of software patches and provides a means of allowing for data corruption in the ROM.

The power requirement for the microprocessor subsystem is approximately 500 mW. A greater demand for processing speed may increase this, but the 100 kHz data rate is not very demanding.

The area of such a subsystem would be approximately 10 cm by 10 cm, 100 cm^2. This could be reduced to perhaps as small as 6 cm by 6 cm if required. As a rule for microprocessor boards, the mass is 1.1 gcm^{-2}, which for a 100 cm^2 board would imply a mass of 0.1 kg. Compared to the ADR mass, this is insignificant.

7.9.7.2 Sofware Approaches

The software for the microprocessor subsystem may be written using one of two main approaches.

1. The monolithic approach is a very linear means of programming. Tasks are set out for execution in a specific sequence, and the cycle of operation is uninterrupted. This approach leads to software which is very predictable, and is small in overall code size. However, this sort of code is difficult to develop, not easy to modify if a software patch must be developed, and can have a low response time due to its rigid structure. In Section 3.7.3 I gave an example of the programming sequence that the microprocessor will have to

execute in order to turn a number of input pulses into an energy histogram. A monolithic program structure would have this sequence operating, with all the required extra functions embedded at certain points.

2. A multi-tasking system is a more flexible approach. A number of sub-programmes, or tasks, operate simultaneously, with each allocated either a fraction of the microprocessor's time, or an operating cycle when required. This type of software is not as predictable, and hence harder to debug, but is a highly flexible system, which can operate more efficiently than an equivalent monolithic design. The flowchart referred to above would comprise one of the running tasks, with other tasks running concurrently.

   The list of tasks a multi-tasking system might have to execute in the example system are as follows

   - Waiting for the OBDH to interrupt, and interpreting and executing the given command.
   - Waiting for an X-ray event to be put into the buffer by the digital electronics ADC output, and the processing the event. The exact nature of the programme executed on the event will vary with the operation mode.
   - Housekeeping tasks such as monitoring the temperature of all the subsystems and the ADR stages.
   - Diagnostics on the microprocessor system such as ensuring memory integrity by parity checking, and error handling.

7.9.8 OBDH Interface Subsystem

The OBDH interface serves to connect all the subsystems of the shown in Figure 7.7 to the rest of the spacecraft systems. The telecommand instructions listed earlier are routed through this subsystem. A remote buffer interface (RBI) converts the communication protocol from that of the system bus to one acceptable

to the OBDH internal microprocessor. The microprocessor has its own memory allocation for OBDH intstruction packets.

7.9.9 DC/DC Converter Subsystem

The purposes of the DC/DC converter are

- To isolate the instrument from the other onboard systems.
- To filter the noise from the rest of the satellite systems.
- To regulate the power supplies to the subsystems.
- To synchronize the various satellite systems power supplies. This may be necessary if it transpires that some subsystems cause noise at particular points in the power cycle, and the points at which noise occurs are to be kept apart to keep the peak noise level to a minimum.

Bibliography

[1] *Novel High-field Permanent-Magnet Flux Sources* - H.A. Leupold, E. Potenziani II, IEEE Trans. Magnetics Vol. MAG-23, No.5 pp.3628-3629, September 1987

[2] *In Orbit Adiabatic Demagnetisation Refrigeration for Bolometric and Microcalorimetric Detectors* - I.D. Hepburn, P.A.R. Ade, I. Davenport, A. Smith, T.J. Sumner, Proceedings of the ESA Symposium on Photon Detectors for Space Instrumentation, Noordwijk, 10-12 November 1992

[3] *Materials for magnetic refrigeration between 2K and 20K* - J.A. Barclay, W.A. Steyert, Cryogenics, February 1982, pp.73

[4] *Calculation of Heat Flow in a Medium, the Conductivity of which Varies with Temperature* - Richard L. Garwin, The Review of Scientific Instruments, Volume 27, Number 10, October 1956

[5] *Magnetic Refrigeration in Space - Practical Considerations* - P. Kittel, Journal of Energy, Vol.4 No.6 pp.266, Nov-Dec 1980.

[6] *Salt Materials testing for a Spacecraft Adiabatic Demagnetisation Refrigerator* - M.L. Savage, P. Kittel, T. Roellig, Advances in Cryogenic Engineering, Vol.35, Plenum Press, New York, 1990, pp 1439-1446

[7] *Design of a spaceworthy adiabatic demagnetisation refrigerator* - A.T. Serlemitsos, M. SanSebastian, E. Kunes, Cryogenics 1992 Vol.32 No.2

[8] *The AXAF/XRS ADR: Engineering Model* - Aristides, T. Serlemitsos, Marcelino SanSebastian, Evan S. Kunes, Advances in Cryogenic Engineering, Vol.37, Part B, Plenum Press, 1992

ERRATA

TECHNICAL ERRORS

Page	Line	Correction
29	4-5	"FWHM at 200mK was **316eV**, with a baseline FWHM of **282eV**, and at 100mK FWHM was **241eV**, with a baseline FWHM of **159eV**.".
40	10	"or an Auger electron" should read "and possibly an Auger electron".
42	15	"Above it has been shown that **initially** $\Delta T = \Delta E / C$.".
49	20	"extrapolation" should be "interpolation".
55	10	"and since $\Delta T = \Delta E / C$".
55	19	"τ = about **0.5 ms = 500** μs".
58	8	"or an Auger electron" should read "and possibly an Auger electron".
58	9	"electron" should read "electron or electrons".
76	21-23	Delete "The rise time... ... semiconductor", replace with "The physical rise-time is much smaller than that imposed by the amplification constraints as detailed in Section 2.1.2.".
93	-	On flow chart, first back loop should join flow after "PULSECOUNT=1" box.
185	11	Change "10000 litres" to "2300 litres".
190	4	Change "$T_F = T_S = T / 2$" to "$T_F = \mathbf{T_p} = T / 2$".
200	8-9	"and...closed" should be replaced by "Both of the heat switches are closed and the situtation returns to that at step 1.".
204	10	"The energy of magnetisation of FAA when subjected to a 2.0 T magnetic field at 1.0 **K** is 13 $J.mol^{-1}$.".
225	9	In "Step 3 - What is Observed", "Heat switch microswitch opens".
225	23	In "Step 9 - What is Observed", "Heat switch microswitch opens".

TYPESETTING ERRORS

Page	Line	Correction
28	26-27	"Cochise Inc." should be italic.
29	10	"Imperial College" should be italic.
29	21	Change "impact" to "incidence".
46	25	"University of London" should be italic.
47	1	"potential divider the two form" should read "potential divider formed by the two"
49	23	"VI" should be italic.
53	22	N in "N is the number of unit cells" should be italic.
60	7	Insert half-space between "6" and "KeV".
60	13,14	"Tin" should be "tin".
74	14	Insert space after "a,".
82	6	"guesses" should be "estimates".
82	27	"informed guesses" should be "estimates".
95	7	The extraneous "*Proc*" should be removed.
113	12	"little doubt **as to the** unexpectedly high value of the FYR".
143	3	Superscript on "Rejection Type" should be removed.
147	10/11	Single line above "200 mK average" should be double.
153	5	The title of the reference should read "*Atomic Fluorescence Yields*".
165	30	Remove space before comma on bottom line.
168	7	Remove superscript on CPA.
179	1	"*Eureka*" should be spelled "*Eureca*"
190	16	"ms^{-2}" should not be italic.
192	21	Delete "a" from "unless a one".
200	6	Add full stop at end of sentence.
200	15	Insert space after "heat switch,".
206	-	Remove extra "STAGE TWO" from bottom left of diagram.
228	18	Correct spelling of "Sofware" to "Software".